THE UNIVERSITY OF CHICAGO

DESIGNING AND DRIVING EXCITED STATE DYNAMICS IN THE CONDENSED PHASE: ULTRAFAST SPECTROSCOPY OF PHOTOSYNTHETIC AND SEMICONDUCTING SYSTEMS

A DISSERTATION SUBMITTED TO

THE FACULTY OF THE DIVISION OF THE PHYSICAL SCIENCES

IN CANDIDACY FOR THE DEGREE OF

DOCTOR OF PHILOSOPHY

DEPARTMENT OF CHEMISTRY

BY

POLINA NAVOTNAYA

CHICAGO, ILLINOIS

JUNE 2021

To my parents, Olga and Aleksandr, with love and gratitude

Маме и папе с любовью

Science, my lad, is made up of mistakes, but they are mistakes which it is useful to make, because they lead little by little to the truth..

- Jules Verne

Because no scientific discovery happens without challenges.

TABLE OF CONTENTS

List of Figures

List of Tables

ACKNOWLEDGMENTS

It really takes a village to get a graduate student to this point. First and foremost, I would like to thank my research advisor, Prof. Greg Engel. Greg's hands-off but very supportive approach let me explore science independently. However, I always knew I could come to Greg with questions and for advice about science, teaching and career. Greg has provided the necessary resources for my work and encouraged me to explore as much I wanted. I also have learned how to present my science for different audiences from Greg. I would also like to thank my dissertation committee – Prof. Guyot-Sionnest and Prof. Tian. I am grateful for the numerous encouraging conversations with Prof. Tian about teaching and careers.

I am honored to have had the opportunity to serve as a teaching assistant in multiple classes at UChicago. I would like to thank Dr. Meishan Zhao, Prof. Greg Engel, Prof. Bozhi Tian, Prof. David Mazziotti, Prof. Ka Yee Lee and Dr. Vera Dragisich for mentorship and example of teaching excellency as I was learning how to be a compassionate instructor. Our work would not be possible without incredible staff that helps the students so much with the endeavors we are taking on. Melinda Moore has always been there to answer numerous questions about all kinds of paperwork and department policies. Luigi Mazzenga has been an incredibly supportive machine shop instructor – I have learned so much, and I enjoyed numerous conversations about history during my time in the machine shop.

I would not have been here without the amazing support from my Purdue family. I have learned so much from Prof. Tim Zwier about spectroscopy and quantum mechanics, and I am grateful for believing in me in my very first year at Purdue away from home by providing me a spot in the research group. Prof. Lyudmila Slipchenko, Prof. Dor Ben-Amotz and Prof. Graham Cooks have

had a tremendous impact on my choice to go into physical chemistry, which I am very grateful for. My academic advisors – Julie Mills and Dr. Beatriz Cisneros – have become sources of unwavering support throughout my college career, and welcomed me with open arms when homesickness kicked in. I am lucky to have worked with Dr. Deepali Mehta-Hurt, Prof. Jacob Dean and Prof. Nathan Kidwell as the best graduate student mentors I could have asked for during my time in the Zwier group. I hope I did justice to their mentorship when I got to mentor undergraduate students.

I was fortunate to work with my amazing colleagues in the Engel group. Dr. Brian Rolczynski has been instrumental in my training as an ultrafast spectroscopist. We spent many hours at the white board together deriving physical principles and drawing parts of the experimental setup. I am grateful for his patience and flexibility, but I am most grateful for the friendship we have developed over the many years of working together. The team of undergraduate students – Ruvim Ginzburg, Matt Talaga, Jonathan Michelsen, RJ Bogdan – brought a lot of joy into the lab and made working on an incredibly difficult project fun. I am especially thankful to senior members of the group – Dr. Ved Singh, Dr. Peter Dahlberg and Dr. Marco Allodi – who have been a fantastic support both with research and career advice. I am so lucky to have worked with Siddhartha Sohoni and Lawson Lloyd on phycobilisome project, and I am so grateful for the friendship that has grown out of our shared work (and many-many pizzas at Medici with Sid). The last year would not have been manageable without their support and help! Po-Chieh Ting has been especially amazing in the many conversations about life and science we've had. And I can't not thank Dr. John Otto, Dr. Ryan Wood, Jake Higgins, Sami Abdulhadi, Elizabeth Bain, Indranil Ghosh, Coco Li, Qijie Shen, Anna Dardia and Danika Nimlos for making my time in the group so enjoyable! Dr. Karen Watters has been instrumental in making sure my writing makes sense, and I am grateful for this!

I’m lucky to have had fantastic support system during my time in graduate school. My best friend from high school, Olesya Beskina, stuck with me through all these years on different continents, and I’m so grateful for her wisdom, bringing smile to my face and always being there when lab life felt too overwhelming. The trips all around Midwest with my friends from Purdue – Rachel Roeder and Alex Parobek – are especially memorable. I am thankful for their love and support long after we graduated from college. I cannot express enough how grateful I am to Cynthia Buckley and Marty Shankland for inviting me to their home and cheering me on always!

When graduate school felt like too much, I always knew I had amazing friends to talk to, go to Ukrainian village with and discuss everything in the world. Igor Fedin, Pavel and Nataliia Elkins and I shared numerous fun home parties, trips around Chicago and hours and hours of fun conversations. Andrii Neshchadin, Valerii Sharapov and Alex Filatov have been the best cookie time buddies – I always looked forward to seeing them three times a week on the first floor of GCIS and talk about our homes, families, work, careers. I cannot state the extent of my gratitude to them for supporting me throughout my PhD. I am confident that we will stay in touch and do our best to meet up at every opportunity.

Most importantly, I am grateful to my family. My parents – Olya and Sasha – are truly the most inspiring people I know. They are my biggest supporters, and I am so thankful for the trusting and loving relationship we have. I thank them for the opportunities they have provided for me, for teaching me the value of curiosity and education, and especially, for instilling values in me. My grandparents – Shimen and Inna – have been very instrumental in my upbringing, and I hope they would be proud of who I grew up to be. Last but not least, I cannot express enough how grateful I am to Vlad for being there for me in the last 6 years. The many travel adventures we have taken

on, the many ice creams at Medici we've eaten, and infinite amount of his support have got me through graduate school. I look forward to hiking the world together.

ABSTRACT

Modern day challenges such as energy crisis or rapid increase in demand of high-quality communications cannot be solved without a collaborative effort from researchers in various fields. As physical chemists, we bring in a unique perspective to the issues from the quantum mechanical standpoint, testing hypotheses about dynamic evolutions of the chemical and biological systems with light. In order to tackle synthetic light harvesting, we need to have deep understanding of the nature's ways of evolving the organisms to perform efficient photosynthesis and protect themselves from stress. To address this, we perform non-linear optical spectroscopy on a specific light-harvesting antenna complex called phycobilisome found in cyanobacteria. We seek to identify the photoprotective mechanisms in the organism to understand their response to excess sunlight. Experiments and theory compliment each other in our work on identifying the precise Hamiltonian of the Fenna-Matthews-Olson complex – another important light-harvesting antenna found in green sulfur bacteria. The developed methodology can assist in finding the exact energetic structures of less-studied biological systems.

There is a lot of promise in using orbital angular momentum of light to alleviate issues of classical and quantum communications. The potentially infinite amount of OAM supplied to light offers solutions to challenges in information multiplexing in optical communications. We can also use the unique response of the chemical systems to twisted light as a detection mechanism in information encoding. In my work, I take the first step towards understanding the interactions of orbital angular momentum of light with bulk gallium arsenide to identify spectral differences as a function of twist in the light using home-built ultrafast transient absorption spectrometer. While

this work is in its early stages, it has shown promising results in establishing the trends governing the electronic transitions induced by twisted light.

CHAPTER 1

INTRODUCTION TO DYNAMICS OF QUANTUM PROCESSES

1.1. Overview

Quantum coherences have long been an intriguing topic for experimental physicists and chemists. One of ways to quantify coherent phenomena in a system is to measure the response of the system to perturbation by light. With the development of ultrafast nonlinear spectroscopies it has become possible to study the electronic, vibrational and rotational properties of the chemical systems in detail. This allows to build complete dynamic profile of the system, explain the time evolution of the excited states, and apply this knowledge to solving issues like energy crisis (by developing artificial photosynthetic methods); limitations of classical and quantum communications (by evaluating entanglement of the electronic states of the system); and controlling materials' properties to perform desired functions (by tweaking the composition or electronic structure of the sample system).

In this thesis I show the electronic properties of a diversity of systems using nonlinear electronic spectroscopic methods such as transient absorption and two-dimensional electronic spectroscopy. In this chapter I discuss the basics of non-linear spectroscopy with the focus on time evolution of the system's excited states. I further discuss in detail the spectroscopic methods involved in my studies, with description of the types of signals we observe, and the experimental challenges with ways to overcome them. Chapter 2 describes the idea of photosynthesis, energy transfer and excess energy quenching mechanisms. Specifically, I look into the stages of photosynthesis with the focus on the parts where ultrafast spectroscopy is needed; the mechanisms of energy transfer such as

FRET, Redfield energy transfer and Coherent energy transfer. Finally, I discuss the various known energy quenching mechanisms in different organisms to show the diversity of nature's ways to protect the photosynthetic systems.

In Chapter 3 I focus on the phycobilisomes isolated from Synechococcus elongatus PCC 7942. Here I discuss the structures of cyanobacteria and phycobilisomes, as well as present the results of fluence-dependent transient absorption measurements resulting in exciton-exciton annihilation as proposed method for excess energy quenching in the organism. Chapter 4 considers 2DES measurements of the Fenna-Matthews-Olson complex with the goal of developing a method of data collection and processing to identify the quantum states of the complex systems in combination with HEOM. In Chapter 5 I show preliminary work on the interactions of orbital angular momentum of light with bulk semiconductors and discuss the theoretical ideas behind the measurements. Chapter 6 presents the proposed work on projects from Chapters 3 and 5.

1.2. Theory of non-linear spectroscopy

In order to observe very short processes, such as energy transfer in photosynthetic antenna complexes or excited state dynamics in semiconductors, we need time-resolved spectroscopic methods. Here I provide a brief summary of theoretical concepts of non-linear optical spectroscopy that are necessary to understand the ultrafast measurements presented in this thesis. Detailed descriptions are found in references (1), (2) and (3).

Time-dependent quantum mechanics

The light-matter interactions, like any other time-dependent quantum mechanical process, is described by a generalized form of the time-dependent Schrödinger equation (Eq. 1):

$$i\hbar \frac{d}{dt} |\Psi\rangle = \hat{H} |\Psi\rangle \quad (1)$$

Here, Ψ is the wavefunction describing the system and $\hat{H}$ is the Hamiltonian operator. The following linear combination of the eigenstates describes the wavefunction of the system (Eq. 2):

$$|\Psi\rangle = \sum_n c_n e^{-iE_n t/\hbar} |n\rangle \quad (2)$$

We can also describe the total Hamiltonian of the system upon perturbation as the sum of the initial Hamiltonian of the system and the interaction term (Eq. 3):

$$H = H_{sys} + \hat{W}(t) \quad (3)$$

When the perturbation $\hat{W}(t)$ is caused by light, we consider the interaction of the electric field of light with the charges in the sample. Under dipole moment approximation, we can write $\hat{W}(t)$ as Eq. 4

$$\hat{W}(t) = -\hat{\mu} E(t) \quad (4)$$

When substituting Eq. 2 and Eq. 4 into Eq. 1, we can find the time evolution of the states m and n (Eqs. 5 and 6):

$$\frac{\partial}{\partial t} c_m(t) = -\frac{i}{\hbar} \sum_n c_n e^{-i(E_n - E_m)t/\hbar} \langle m|\hat{W}(t)|n\rangle \quad (5)$$

or

$$\frac{\partial}{\partial t} c_m(t) = -\frac{i}{\hbar} \sum_n c_n e^{-i(E_n - E_m)t/\hbar} \langle m|\hat{\mu}(t)|n\rangle E(t) \quad (6)$$

Upon interaction with light, a superposition of the ground and the excited states is created. Then we can write the time evolution of one individual state as a function of the other state in a two-state system (Eqs. 7 and 8):

$$\frac{\partial}{\partial t}c_1(t) = \frac{i}{\hbar}\sum_n c_0(t)e^{-i(E_0-E_1)t/\hbar}\langle 1|\hat{\mu}(t)|0\rangle E(t) \tag{7}$$

$$\frac{\partial}{\partial t}c_0(t) = \frac{i}{\hbar}\sum_n c_1(t)e^{-i(E_1-E_0)t/\hbar}\langle 0|\hat{\mu}(t)|1\rangle E(t) \tag{8}$$

where $|0\rangle$ is the ground state of the system, and $|1\rangle$ is the excited state.

We then have the superposition of the states propagating with time *t* to look like Eq. 9:

$$\left|\Psi(\mathrm{t})\right\rangle = c_0 e^{-\frac{iE_0 t}{\hbar}}\Big|0\rangle + ic_1 e^{-\frac{iE_1 t}{\hbar}}|1\rangle \tag{9}$$

Interaction of the sample with the laser pulse generates macroscopic polarization P(t). It described the induced electric field from the motion of the charges that. This is exactly the signal we detect in our spectroscopic experiments as shown in Fig.1.1. Time-dependent polarization can be written out as the expectation value of the transition dipole moment, which leads to Equations 10 and 11:

$$P(t) = \langle\mu\rangle = \langle\Psi(t)|\hat{\mu}|\Psi(t)\rangle \tag{10}$$

$$P(t) = (c_0 e^{\frac{iE_0 t}{\hbar}}\langle 0\Big|-ic_1 e^{\frac{iE_1 t}{\hbar}}\langle 1|)\hat{\mu}(c_0 e^{\frac{iE_0 t}{\hbar}}|0\rangle + ic_1 e^{\frac{iE_1 t}{\hbar}}\Big|1\rangle$$

$$= c_0 c_1\langle 0|\mu|1\rangle \sin\left(\frac{(E_1-E_0)t}{\hbar}\right) + c_0^2\langle 0|\mu|0\rangle + c_1^2\langle 1|\mu|1\rangle \tag{11}$$

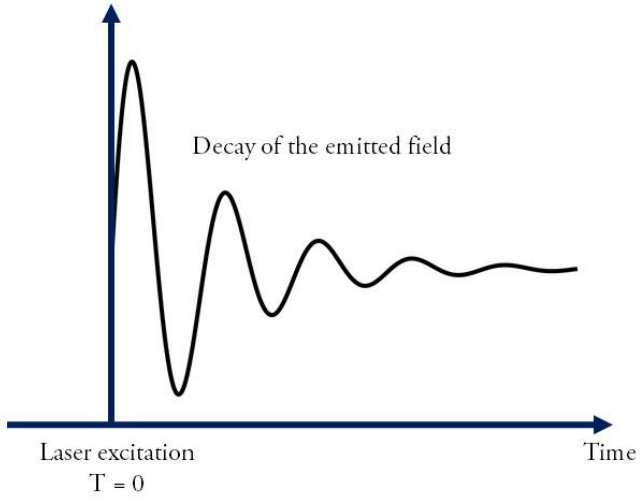

Figure 1.1. Decay of the emitted macroscopic polarization signal after a light-matter interaction at time T = 0

Density matrix formalism

The above notation is plausible for a single light-matter interaction in a two-state system. However, in the non-linear spectroscopic experiments that I describe later in this thesis it is a number of states and a number of pulses involved in the light-matter interaction. This is where we adopt the density matrix formalism as an important tool to describe this kind of interaction.

A density matrix is a mathematical function that describes the quantum of state of the system of interest. More applicably to our work, it describes the behavior of the ensemble of states that make up the chemical system. Mathematically, it is the sum of the outer product of the wavefunctions of the states – pure and mixed – in the system (Eq. 12):

$$\rho = \sum_k p_k |\Psi_k(t)\rangle\langle\Psi_k(t)| \tag{12}$$

Here p_k is the statistical probability of finding a system in the quantum state k.

From equation 10, we describe polarization – the quantity that we measure in the experiments – as an expectation value of the transition dipole moment operator. When we apply the dipole operator to the density matrix, we obtain the expectation value as a function of the density matrix (Eq. 13):

$$P(t) = \langle \hat{\mu}(t) \rangle = Tr[\hat{\mu}\rho(t)] \tag{13}$$

Here Tr is the trace operator.

Time dependence of the density matrix is calculated with the time derivative of the density matrix. This differential form is described by Liouville von Neumann equation (Eq. 14):

$$\frac{\partial \rho}{\partial t} = -\frac{i}{\hbar}[H, \rho] \tag{14}$$

Density matrix formalism is especially important in non-linear spectroscopies because it allows to measure the degree of coupling between the individual states of the system upon excitation.

Third-order polarization spectroscopy

Equation 14 can be expressed in the n^{th} order form (Eq. 15):

$$P^{(n)}(t) = \left[\langle \hat{\mu}\rho^{(n)}(t) \rangle\right] \tag{15}$$

Here $\rho^{(n)}$ is the n^{th} order of density matrix that is created by interacting with the electromagnetic waves n times. If we describe the light-matter interactions in a time-ordered fashion $\{t_1, t_2, \ldots\}$, we can write out the third-order polarization (Eq. 16):

$$P^{(3)}(t) \propto \int_0^\infty dt_3 \int_0^\infty dt_2 \int_0^\infty dt_1 \, E_3(t - t_3) E_2(t - t_3 - t_2) E_1(t - t_3 - t_2 - t_1) * R^{(3)}(t_1, t_2, t_{3)} \tag{16}$$

The third order response function is calculated with $R^{(3)}(t_1, t_2, t_{3)}$ and describes the response of the sample to its interaction with electromagnetic field three times (Eq. 17):

$$R^{(3)}(t_1, t_2, t_{3)} \propto -i\langle\hat{\mu}(t_3 + t_2 + t_1)[\hat{\mu}(t_2 + t_1), [\hat{\mu}(t_1, |\hat{\mu}(0), \rho(-\infty)]]]0\rangle \quad (17)$$

While the mathematical form of the third-order polarization and the response function is pretty complex, there is a great way to visualize the interactions of the light and the energy states of the sample as multiple interactions arrive with some time delay between them. They are described by the Feynman diagrams. These are ladder-like structures that describe the direction of linear momentum of each pulse, the changes in the energy states upon each interaction as time evolves.

Let's consider an example of a Feynman pathway. In Figure 1.2, we see that time evolves along y-axis. The red arrows represent the momentum of the pulse. The last interaction is generated as a geometric sum of k_1, k_2 and k_3, and is called k_s. When the arrows point toward the energy state in bra or ket form, it describes the absorption of the photons and evolving that state to the higher energy state. Alternatively, when the arrow points away from the bra or the ket, it shows the emission from the state to a lower-lying state. The final state after the emission of k_s must be in a population form, meaning the states involved should be the same. When the states are different, they are called coherences. Additionally, all the arrows that point to the right mean positive wave vectors, and the ones pointing to the left indicate the negative wave vectors.

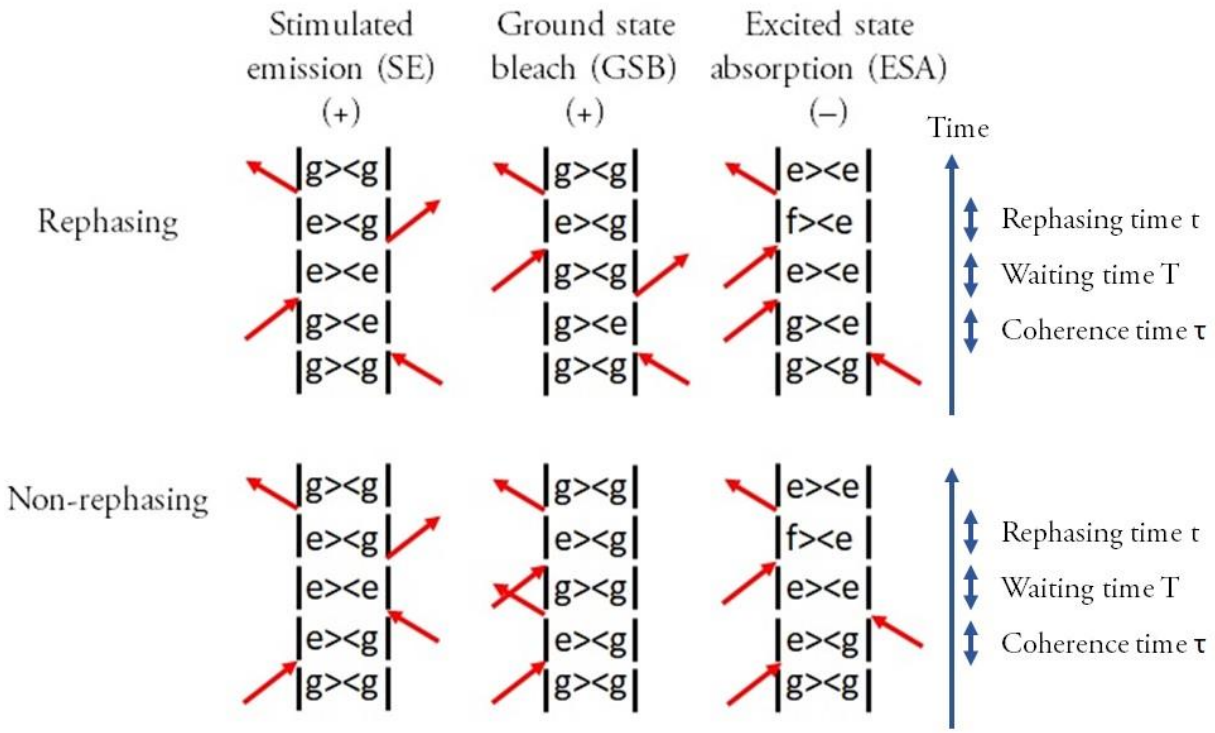

Figure 1.2. Feynman diagrams that describe the possible light-matter interaction pathways as laser pulses interact with the sample. Time evolution is shown along vertical dimension. The red arrows represent the directions of wavevectors k. The arrows pointing toward the diagram represent absorption, and away from the diagram – emission.

We further discriminate the signal wavevectors by the sign and the population in the final state after the signal emission. In ground state bleach, the signal is positive because the k_s is in phase with the final excitation field. Here, the final state is the population of the ground state. Similarly, the stimulated emission signal is positive and ends up in the population of the ground state. The difference comes from the type of population after the second light-matter interaction. In GSB, the population is always in the ground state, whereas in SE, the population after the first two interactions is in the excited state. The third type of signal is excited state absorption – a negative signal that involves a third state in its Feynman pathway.

Additionally, there is distinction between the rephasing and non-rephasing signals for each of the three types. In rephasing signal, the phases of the first and the third interactions are evolving in the opposite direction. In non-rephasing, these phases are evolving in the same direction. These distinctions give a total of six possible pathways for the signals in non-linear spectroscopy. In both transient absorption spectroscopy and two-dimensional electronic spectroscopy, it is possible to resolve some of the combinations of these signals.

It is worth noting that in transient absorption coherences are not observed. While this will be discussed in the next section, briefly, this is due to the fact the "first" and the "second" interactions happen simultaneously, promoting the charges straight to population in the excited state.

1.3. Methods of non-linear spectroscopy

Many processes, from photosynthetic to semiconductor transitions, occur on femtosecond to picosecond timescales. Triplet states can last on scales of nanoseconds to milliseconds. Thus, we need a reliable ultrafast measurement that will allow to investigate the processes happening at the fastest timescales (4 - 7). Many optical components are involved in the experimental setup in order to construct a reliable ultrafast measurement. The main components of the setup include ultrafast lasers, control of pulse compression and amplitude, transient absorption or 2DES components and a detection mechanism. Below I will describe the instruments used for both 2DES and pump-probe experiments, and the unique components of each setup.

Ultrafast oscillator

The Ti:Sapphire crystal in Micra (Coherent) is excited with a high power 532 nm beam generated with diodes. Stimulated emission from the crystal is traveling between the end mirrors of the

oscillator cavity. The length of the cavity sets the repetition rate of the pulsed output. In this laser, the repetition rate is 80 MHz. Due to effects like Kerr lens modelocking, the pulse is shaped into ~100 fs pulse with ~60 nm FWHM centered at 800-805 nm (8). The typical power output of the modelocked pulse is ~400 mW. The instantaneous power of this pulse output is usually not enough for the studies we perform in the Engel group, so this output is mainly used to seed the regenerative amplifier.

Regenerative amplifier

There are four components to the regenerative amplifier: pulse stretcher, pump beam diode, cavity and pulse compressor. The seed from the oscillator is stretched in time in order to avoid burning the Ti:Sapphire crystal in the cavity. The stretcher is a setup with a grating and a collection of mirrors to purposefully apply temporal chirp to the seed pulse. Simultaneously, a very high power (~20 W) 532 nm pump beam from the diode generates the excited states in the cavity crystal. The stretched seed generates stimulated emission that further travels through the cavity in roundtrips and is amplified (9). The ejection of the pulse from the cavity is controlled by the timings of the Pockels cells (10) – the electronically-controlled waveplates that, when activated, change the polarization of the light passing through them. The pulse coming out of the cavity is still stretched, so it needs to go through an ultrafast compressor. A compressor is a setup similar to stretcher, but reverse in action. The resulting output pulse is ~3 W, 35 fs and 30 nm FWHM centered at ~800 nm at 5 kHz repetition rate.

Generation of white light continuum

The bandwidth of the regenerative amplifier output is somewhat narrowband. A lot of experiments performed in the Engel group require much broader bandwidth going into 500s and 600s nm. To accomplish this goal, the output of the regen is focused in a pressurized argon tube (11). Argon atoms emit light with wavelengths between ~500-900 nm. The efficiency of this process is about 30%, meaning that the output power is ~1 W. The light is further cut off on red and/or blue sides to obtain the spectrum that is needed for further experiments. The filtered output is sent to combination of chirped mirrors (12) and/or MIIPS (13) – this accomplishes the compression of light down to sub-10 fs pulse. MIIPS also provides amplitude shaping of the pulse that allows to have more or less Gaussian pulse in amplitude for the experiments.

The broadened and Fourier transform-limited beam is further sent to either a transient absorption setup or a two-dimensional electronic spectroscopy setup. We will briefly discuss both further.

Transient absorption spectroscopy

The main principle of transient absorption spectroscopy is the excitation of the sample with a strong pump pulse and probing the excited states generated upon the first interaction with the probe pulse arriving at the sample after some time delay. This is accomplished by splitting the output of the regen or MIIPS into two pump and probe beam using a 90/10 or 95/5 (pump/probe) beamsplitter. The pump is further sent down to the automatic delay stage that controls the delay between the two pulses. It is also chopped at 2.5 kHz repetition rate to collect signals with and without sample's interaction with pump. The probe travels directly to the sample. The probe is set

to be significantly weaker than the pump pulse in order to avoid additional excitation of the sample with the probe. Both beams are focused at the sample position, overlapping for best signal strength.

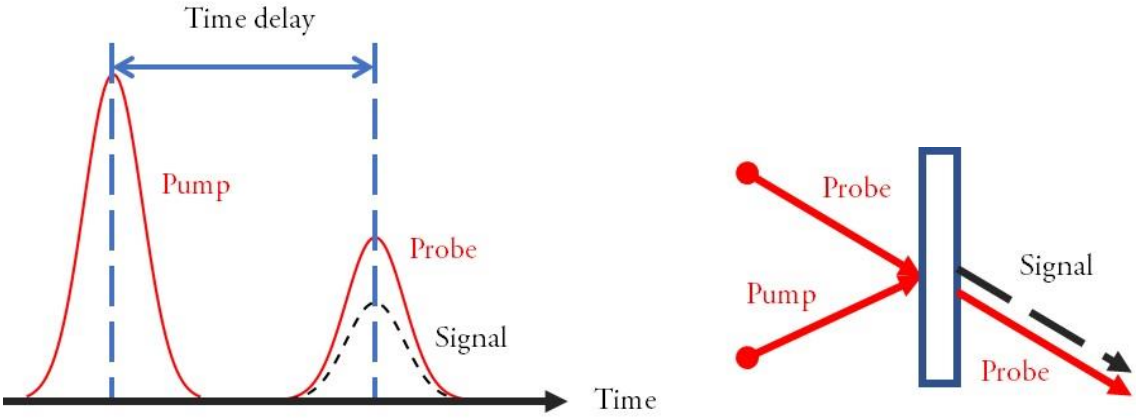

Figure 1.3. (Left) Schematic representation of transient absorption experiment. Pump and probe are separated by a time delay. (Right) Phase matching in pump-probe spectroscopy showing signal being emitted in the direction of probe pulse.

Due to phase-matching conditions, the signal from the interaction of pump and probe with the sample is emitted in the direction of the probe and they travel colinearly. The pump beam is blocked after the sample to avoid interference of the pump and the probe in the detector. The probe along with the signal are sent to the spectrometer grating to resolve the intensity of the signal at each wavelength. Post-grating the signal is spatially elongated and spatially chirped, and sent to a linescan CCD camera. This results in a collection of light intensity at certain wavelengths for each time delay. The data are collected for pump- and pumpless frames for further analysis. This will be described in detail in the next section.

Two-Dimensional Electronic Spectroscopy (2DES)

In 2DES, a level of complexity is added to the pump-probe experiment (14). What is used as a pump beam in transient absorption is now split into two beams. These beams are separated by a delay in time called coherence time. The third beam is delayed from the second one by waiting time. The fourth pulse acts as a probe beam and is highly attenuated to avoid additional excitations. The signal is emitted in many directions, however, the only collected signal comes in the phase-matched direction, i.e. in the direction of the geometric sum of the four pulses. A total of two delay stages are used to generate the time delays necessary for the experiment. The four pulses are focused at the sample in a boxcar geometry.

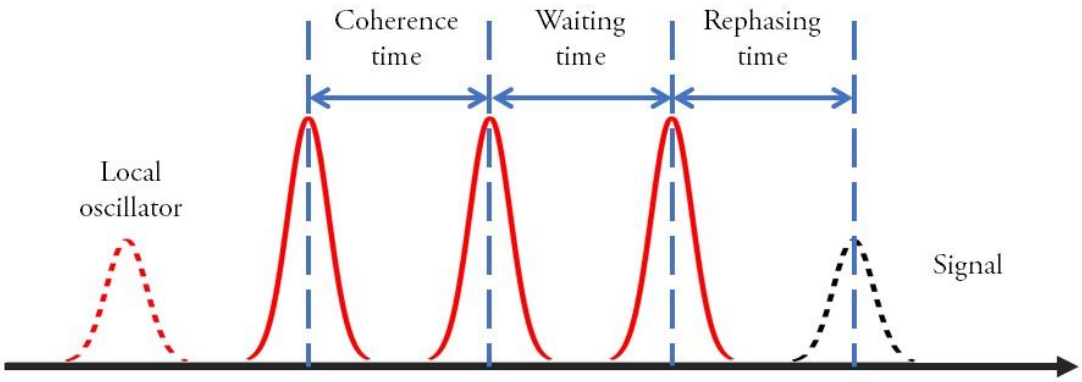

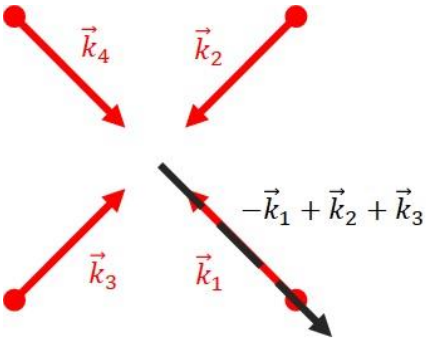

Figure 1.4. (Top) Pulse sequence for a two-dimensional electronic spectroscopy experiment as time evolves.

(Bottom) Boxcar geometry representation where signal is emitted in the direction of k_4.

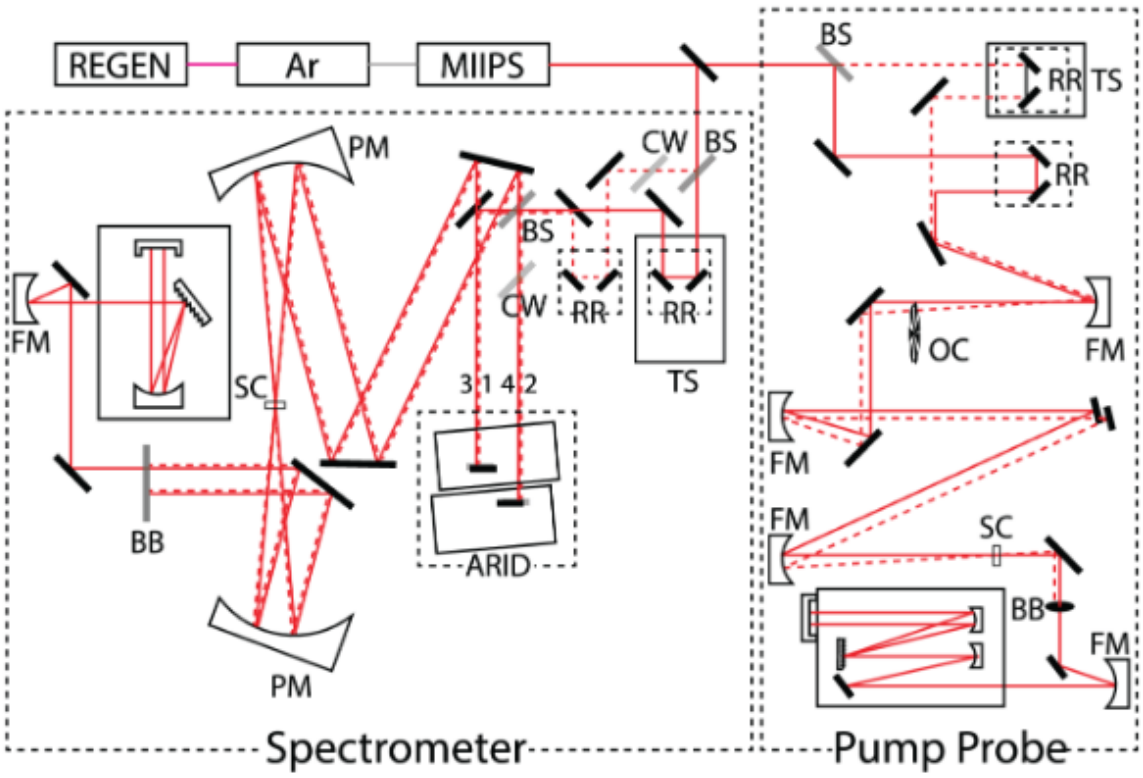

Figure 1.5. Schematic representation of 2DES and pump-probe spectrometers. Laser beam ejected from the laser passes through argon tube and MIIPS to generate broadband compressed pulse. The pulse is then split using beamsplitters (BS) and the reflected beam passes through compensating glass (CW) to correct for dispersion. Retroreflectors (RR) are placed on top of the translation stages (TS) to ensure that beams travel with controlled delay. All-reflective interferometric delay system (ARID) ensures correct coherence time. The beams are focused at the sample in boxcar geometry, and only local beam 4, along with the signal emitted in the same direction, is focused into the spectrometer and camera. On the right side is the pump-probe setup used to collect transient spectra for future phasing. Pump beam passes through RR on a delay stage, and its frequency is modulated with optical chopper (OC). The pump and probe beams are focused at the sample, and probe is then focused into spectrometer and CCD camera. Figure adapted from (14) with full permission.

The 2DES experiment is much longer than the pump-probe experiment. This is due to the fact than additional coherence time stage needs to be scanned to collect signals coming from coherences (described above). The end result of this experiment is a collection of 2D plots with the excitation and detection energies along x- and y-axis, intensity shown in color. The amount of these plots is defined by the the waiting time span and the time step at which waiting time data are collected. The data analysis is discussed in the section below.

1.4. Data processing in non-linear spectroscopy

Issues of noise and scatter arise as a result of our measurements. While some of these issues depend primarily on sample characteristics (scattery sample, low signal-to-noise ratio in spectral areas where absorption is little), many of the challenges associated with the data collection in ultrafast spectroscopy experiments are addressable in the data acquisition and analysis phases of the experiment. Some of these challenges can be also solved during the measurement by flowing the sample using the peristaltic pump for liquid samples, or moving the beam around to avoid burning through the sample for both liquid and solid samples. However, below I discuss the methods of data analysis for both pump-probe experiments and 2DES.

Transient absorption

The probe interacts with the sample every 200 μs, or at the repetition rate of 5 kHz. We collect every frame of this interaction. The pump, on the other hand, is chopped to interact with the sample half of the times – along with every other probe interaction. Hence, we collect pump-probe frames and probe-only frames. The probe frames are subtracted from the pump-probe signal. Even though the pump beam is blocked directly after the sample, there is still strong interference between the

scattered pump and the signal at delay times around T = 0. If the time step in the "waiting" time is fine enough, we can window out the scatter around T = 0 in the Fourier domain in post-processing. Otherwise, if we are interested in long time dynamics, we just omit the signals in the vicinity of T = 0. Additionally, we collect multiple runs of the same experiment to obtain statistical information for further averaging and error analysis. Finally, we collect the T<0 time points (where the probe precedes the pump, and no signal should be observed) in order to subtract the average of these points and eliminate the scatter for final analysis.

Two-Dimensional Electronic Spectroscopy (2DES)

The signals that are collected on the detector in a 2DES experiment make a rephasing frequency axis, or the detection axis mentioned above. This axis can be Fourier-transformed into a rephasing time axis. Much like in transient absorption spectroscopy, scatter is an issue in collecting these spectra, but in 2DES scatter appears from interactions of four beams rather than two. During data acquisition, frames with one or more beams blocked are collected to obtain the scatter intensities from individual beams Hence, windowing needs to be performed more than once.

The largest challenge in the 2DES experiment specifically in boxcar geometry is the loss of phase information along the way. This issue is resolved by taking a pump-probe measurement that retains phase information, and "phasing" the 2D data with respect to the pump-probe data. Projection-slice theorem allows to match the projection of 2D spectrum to the slice of the corresponding pump-probe spectrum. This heavily relies of the quality of the pump-probe spectra. A way to avoid a phasing issue it is possible to perform 2DES experiments in pump-probe geometry.

References

(1) S. Mukamel. Principles of nonlinear optical spectroscopy. Oxford University Press, New York, New York, 1995

(2) P. Hamm, M.T. Zanni. Concepts and methods of 2D infrared spectroscopy. Cambridge University Press, New York, New York, 2011

(3) A. Tokmakoff. Nonlinear spectroscopy. https://tdqms.uchicago.edu/2d-spectroscopy-notes/, 2011

(4) P.D. Dahlberg, P. Ting, et al. Mapping the ultrafast flow of harvested solar energy in living photosynthetic cells. Nature Communications, 8:988, 2017

(5) R.E. Wood, L.T. Lloyd, et al. Evidence for the dominance of carrier-induced band gap renormalization over biexciton formation in cryogenic ultrafast experiments on MoS_2 monolayers. J. Phys. Chem. Lett, 11(7):2658-2666, 2020

(6) R. E. Blankenship. Molecular mechanisms of photosynthesis. Blackwell Science, Malden, Massachusetts, 2002

(7) E. Harel, P.D. Long, G.S. Engel. Single shot ultrabroadband two-dimensional electronic spectroscopy of the light-harvesting complex LH2. Optics Letters, 36(9):1665-1667, 2011

(8) J. Kerr. A new relation between electricity and light: Dielectrified media birefringent. Philosophical Magazine and Journal of Science, 50:332, 337-348, 1875

(9) D. Strickland, G. Monrou. Compression of amplified chirped pulses. Optics Communications, 56(3):219-221, 1985

(10) A. Yariv, P. Yeh. Photonics – Optical electronics in modern communications. Oxford University Press, 2007

(11) M. Loy, Y. Shen. Study of self-focusing and small-scale filaments of light in nonlinear media. IEEE Journal of Quantum Electronics, 9(3):409-422, 1973

(12) P. Dombi, V.S. Yakovlev, et al. Pulse compression with time-domain optimized chirped mirrors. Optics Express, 13(26):10888-10894, 2005

(13) X. Zhu, T.C. Gunarante, et al. In-situ femtosecond pulse characterization and compression during micromachining. Optics Express, 15(24):16061-16066, 2007

(14) H. Zheng, J.R. Caram, et al. Dispersion-free continuum two-dimensional electronic spectrometer. Applied Optics, 53(9):1909-1917, 2014

CHAPTER 2

ENERGY MOVEMENT IN PHOTOSYNTHETIC ANTENNA COMPLEXES

2.1. A spectroscopist's view on photosynthesis

Photosynthesis is the process of harvesting solar power and turning it into chemical energy in plants, bacteria and algae (1). In high school biology we learn that photosynthesis is the process of converting carbon dioxide and water using sunlight into oxygen. While this is a correct assessment of the process, it does not describe the complete picture. In reality, this is a much more complex system. The path from sunlight entering the organism to producing carbohydrates and oxygen takes seconds (2). For us, ultrafast spectroscopists, a second is a very long time when we operate on timescales of femtoseconds, or a millionth of a billionth of a second.

We can divide the processes happening in a photosynthetic organism into chemical and nonchemical. The names speak for themselves – in chemical processes bonds are made and broken. Nonchemical processes involve the interaction of light with the organism, exciting the electrons into the excited states (3). This interaction is what makes us interested in the topic. As described in Chapter 1, we study the quantum mechanical properties of light-matter interactions, and into the next two chapters we will focus on discussing these quantum mechanical processes in photosynthetic organisms.

Photosynthetic events can be split into three main stages (Figure 2.1). In the first stage, light harvesting antenna complexes harvest energy from sunlight. An organism consists of a set of light harvesting antenna geometrically close together that funnel energy downhill. An exciton is generated when the most peripheral, and the bluest, antenna complex is excited.

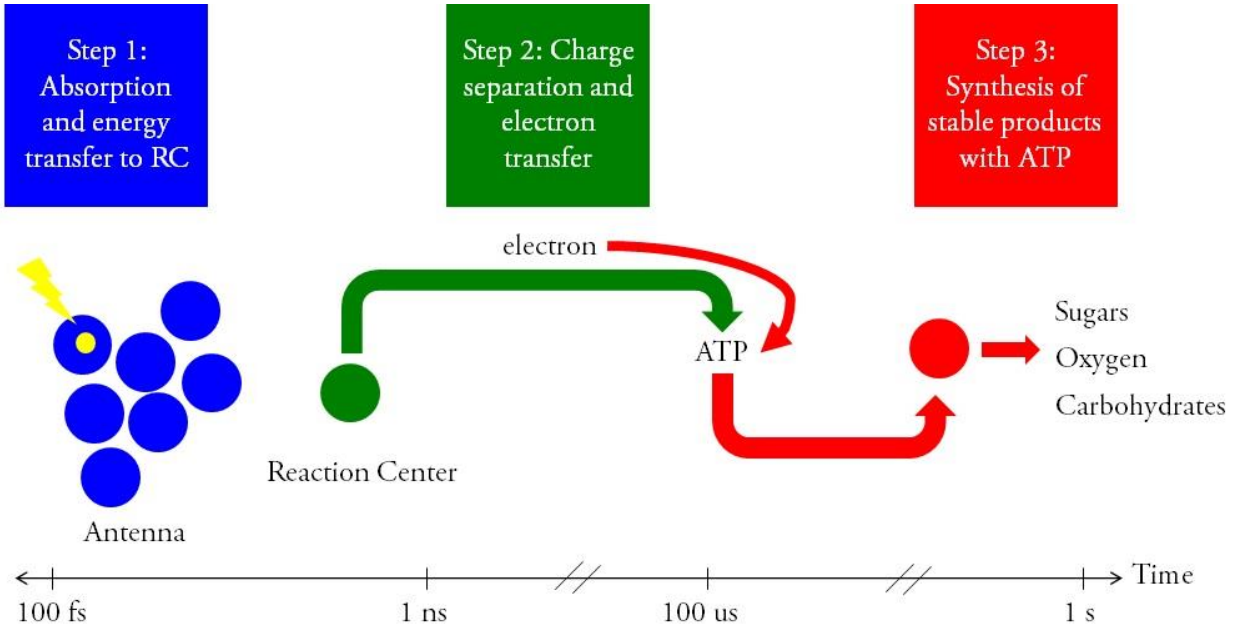

Figure 2.1. General stages of photosynthesis upon sunlight entering light-harvesting antenna in an organism. As light is absorbed by the antennae, it is transferred through a "funnel" of chromophores down to the reaction center. Charge separation and electron transfer to ATP happens in the second stage. Electrons facilitate synthesis of carbohydrates and/or oxygen in stage 3.

It moves downhill among the network of light harvesting antenna that have slightly different energy. There are reasons for the different energies in the chromophores to allow the energy to flow downhill: 1) the chromophores have slightly different chemical structure with different absorption and emission spectra (4), and 2) the environment around identical chromophores is different in such a way that the energy flow is facilitated thermodynamically (5). After hopping between chromophores, the exciton ends up in the reaction center (RC) because it is of lower energy than the chromophores where the light entered. This whole stage happens on a nanosecond timescale, and this is the stage we are most interested in as ultrafast spectroscopists.

The second stage involves the excitation in the reaction center moving to a pigment that gets ionized and releases an electron. This electron then binds to an acceptor, generating an anion. The anion physically travels further away from the pigment cation, decreasing the probability of cation-anion recombination. This happens on the order of hundreds of microseconds.

The third stage is characterized by moving ATP-synthase across a proton gradient to generate ATP. The ATP is then fueling the reactions to form carbohydrates and oxygen. This process occurs on seconds timescale from the initial excitation.

Photosynthetic processes happen incredibly efficiently despite all the competing mechanisms occurring in the light harvesting antennae simultaneously (1). The organisms have evolved over billions of years to harvest light as safely for the organism as possible, while keeping the forementioned three stages going properly and minimize photoinhibition (reduction in photosynthetic efficiency). This means that the organisms had to adapt to changes in the solar activity throughout the 24 hours of the day – daylight vs nighttime – and changes of intensity of light due to different solar activity on a given day. These protective mechanisms are designed to remove the excess energy from the system to prevent it from damage. When too much sunlight is supplied, the reactive singlet oxygen species that damage the photosynthetic machinery are formed (1, 6 – 9). Briefly, the photoprotective mechanisms are different in various organisms, but all rely on a conformational change (alternatively, electronic structure) of the chromophore or a chemical reaction that will pull the excess energy away from the photosynthetic machinery, or changes in physiological environment of the organism (6, 10). In this thesis I seek to understand the excess energy quenching mechanisms in cyanobacterial Synechococcus elongatus PCC 7942 phycosilisome.

2.2. Energy transfer in photosynthesis

Energy transfer upon excitation of a light-harvesting complex is the process that takes place on a nanosecond timescale. With the Engel group's ultrafast spectroscopic methods, we are capable of measuring the rates of energy transfer to understand the mechanisms of energy flow within the system. The three most known types of energy transfer in photosynthesis are the following:

1) Förster Resonance Energy Transfer – with the weak inter-chromophore coupling
2) Redfield Theory – with the strong inter-chromophore coupling
3) Quantum Coherent Energy Transfer – intermediate inter-chromophore coupling

The following sections will describe each type of energy transfer in more detail.

Förster Resonance Energy Transfer (FRET)

Because the chromophores in FRET are weakly coupled, the transfer occurs through hopping of excitations between the chromophores (11, 12). Therefore, FRET is heavily distance dependent, and the FRET rate is described with the following equation (Eq. 1):

$$k_{FRET}(r) = \tau_D^{-1}(\frac{R_0}{r})^6 \quad (1)$$

Here r is the distance between the donor and acceptor chromophores, R_0 is the distance where the energy transfer's efficiency is 50% and τ_D is the fluorescence lifetime of the donor chromophore.

The R_0 additionally is heavily dependent on J (Fig. 2.2) – the spectral overlap of the donor chromophore's fluorescence and the acceptor chromophore's absorption. We can calculate it using equation 2:

$$R_0^6 = \frac{8.97*10^{-5}J\kappa^2}{n^4} \quad (2)$$

Here n is the refractive index, κ is the overlap between the transition dipoles of the donor and acceptor chromophores.

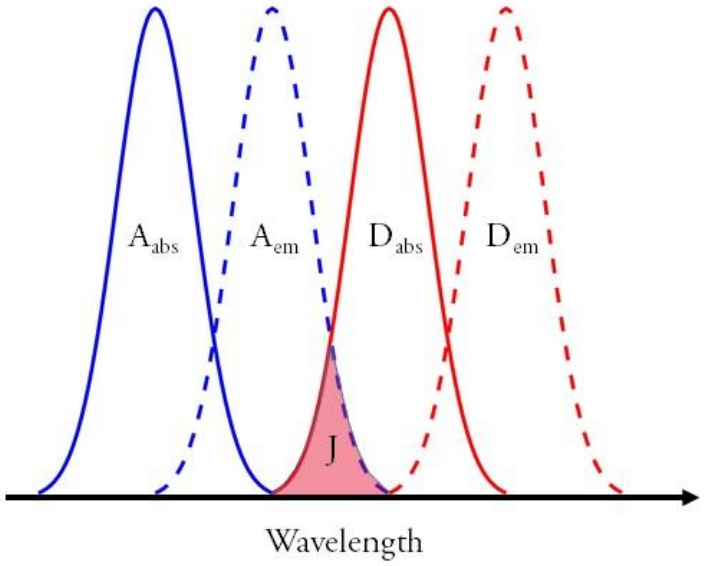

Figure 2.2. Spectral overlap J between the absorption spectrum of the donor molecule and the emission spectrum of the acceptor molecule in FRET.

For instance, the energy transfer mechanism in Rba. sphaeroides is mainly FRET for all the energy transfers down the funnel. FRET can also be expanded into generalized FRET that describes the interaction of delocalized excitons that are weakly coupled to each other.

Redfield theory

Redfield theory operates in the strongly coupled chromophore systems (13). This means that the excitons forming in the light harvesting complexes are highly delocalized. This is typically facilitated by system-bath coupling that is much weaker than the chromophore coupling in systems like Fenna-Matthews-Olson complex (5, 14). This system-bath coupling is heavily dependent on considering the bath as phonons, or vibrational modes of the lattice. Due to Born-Oppenheimer approximation, the bath is oscillating at much smaller frequency than the chromophores. The electronic states are now mixing forming a delocalized state (Fig. 2.3). The rate of the Redfield energy transfer is the following (Eq. 3):

$$k_{AB} = 2\gamma_{12} C^{Re(\omega_{12})} \tag{3}$$

Here $C^{Re(\omega_{12})}$ is the correlation function of the between the system and the bath, γ_{12} is the spatial overlap between the excitons 1 and 2 that is dependent on the distance between the chromophores.

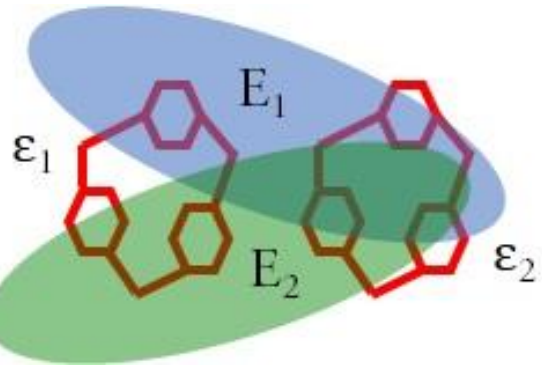

Figure 2.3. Strong electronic coupling between electronic states ε_1 and ε_2 results in two excitons with energies E_1 and E_2.

Additionally, there exists modified Redfield theory that describes the organisms with not only strong electronic coupling, but also strong vibronic coupling (15). This does not allow to treat the

system-bath interactions as a perturbation, but rather as part of the system complicating the overall Hamiltonian.

Quantum Coherent Energy Transfer

FRET and Redfield theory describe the chromophores or excitons as metaphorical particles that express particle-like behavior. Additionally, in these models the coupling between the chromophores is similar in magnitude to the coupling between the chromophores and the phonon modes from the bath. Thus, both these models ignore the fact that excitations are actually expressed as wavefunctions, which are heavily described with quantum mechanical principles (16).

In ultrafast spectroscopy, we generate an exciton that we can described as the superposition of the ground and excited states of the chromophore. The oscillations of these superpositions happen at the frequency of the energy gap between the states. As time progresses after the excitation, the oscillations decay in waiting time, and we can probe that by Fourier-transforming the signal along the waiting time domain to get the frequency of those oscillations. Hence, we generate a quantum coherence of the superposition of ground and excited states that decays over time. These coherences can include electronic states or vibrational states, or both. Quantum coherent energy transfer relies on quantum probabilities of the energy motion between the states, and can describe the energy transfer pathways in photosynthetic complexes more accurately (17).

2.3. Excess energy quenching in light-harvesting antennae

Photoprotective mechanisms are necessary to ensure that the photosynthetic organisms can function efficiently and safely (6, 18, 19). Quenching sites are generated in the antennae when the organism is under stress. These sites dissipate energy as heat using various photoprotective

mechanisms. There are as many photoprotective mechanisms as there are photosynthetic light harvesting complexes. However, we can group them into a few categories:

1) Orange Carotenoid Protein (OCP) conformational change
2) Redox changes in the system in response to light
3) pH-mediated quenching
4) Dissipation of sunlight as heat via exciton-exciton annihilation

Below I will briefly discuss the first three types of excess energy quenching in various photosynthetic complexes. Chapter 3 of this thesis will elaborate in detail on exciton-exciton annihilation specifically in S. elongatus PCC 7942.

Quenching via OCP conformational change

Cyanobacteria contain peripheral antenna complexes called phycobilisomes that absorb sunlight and move the energy downhill for photosynthesis (3, 20). These phycobilisomes typically consist of phycoerythrin (PE, encountered in some PBS) and phycocyanin (PC) rods, and the core containing allophycocyanin (APC). The excitations flow down the funnel from PE to PC to APC. While Chapter 3 will discuss energy quenching mechanisms in cyanobacteria S. elongatus PCC 7942, below I would like to describe a mechanism that some cyanobacteria employ to quench the excess light.

The Orange Carotenoid Protein, present in some cyanobacteria like S. spirulina PCC 6803, is the structure that undergoes conformational change upon interaction with light (21 – 23). The native form of OCP – the orange form OCP^o – converts into its red form OCP^r upon photoactivation (Fig. 2.4). The OCP^r is now capable of binding to the core of phycobilisome and heat is emitted as a

result of this binding. While the mechanism of how specifically OCP interacts with the core is not experimentally studied, there current hypothesis is that there is charge transfer between the excited core of the PBS and the OCP^r that allows for excess excitation quenching. Fluorescence Recovery Protein (FRP) is present nearby, binding to the OCP^r and assisting in reversal of OCP^r back to OCP^o. This mechanism allows to reuse the OCP and FRP for the next cycle in the quenching process.

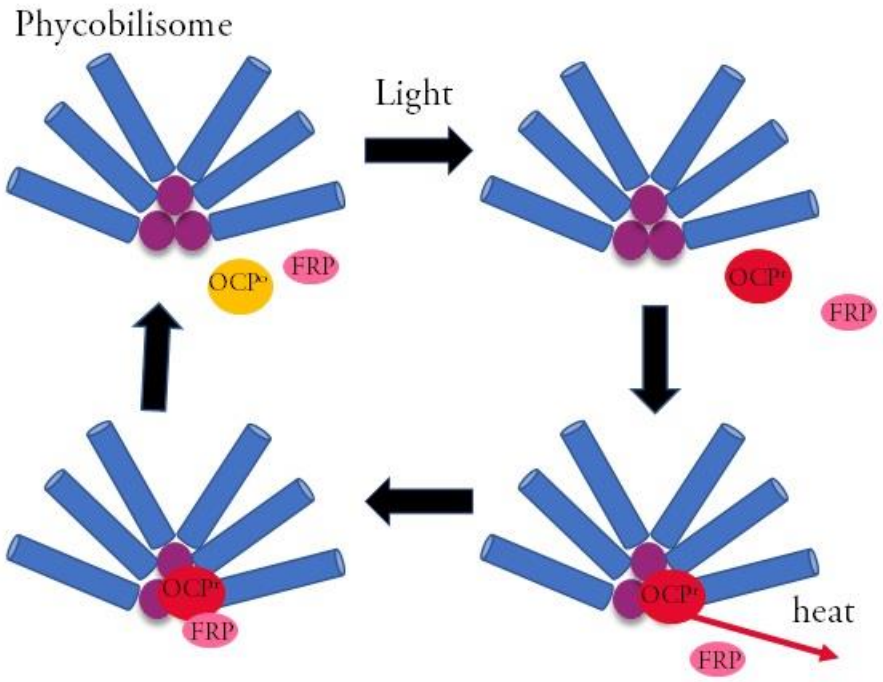

Figure 2.4. Excess energy quenching mechanism in OCP-containing cyanobacteria. The light is absorbed by phycobilisomes, while OCP remains in its orange from. Excess light isomerized OCP^o to red form OCP^r and binds to the core of the phycobilisome. The excess energy is then released as heat. Fluorescence recovery protein (FRP) binds to OCP^r and releases it from phycobilisome to continue the cycle.

OCP-related mechanism is also employed in some green sulfur bacteria in combination with other photoprotective mechanisms (24).

Redox changes in the system in response to light

In green sulfur bacteria, such as Chlorobaculum tepidum, excess energy quenching happens via mechanisms that are regulated with varying redox conditions (25, 26). A strong dependence of fluorescence lifetime on redox conditions within the organism was observed that led to the studies of the chemical compounds within the bacteria that can react so strongly to level of oxidation. Isoprenoid quinones were found in the structure, leading to believe that they undergo chemical reaction to assist in excess energy quenching (Fig. 2.5). These are generally observed in the peripheral antennae of the green sulfur bacteria, the bacteriochlorophyll c (BChl c).

Similar mechanism is employed in the next antenna of the Chlorobaculum tepidum, the Fenna-Matthews-Olson complex (27 – 29). It consists primarily of bacteriochlorophyll a (BChl a) that is embedded in the protein bath. This bath assists in the energy transfer from the highest energy BChl a down to the reaction center. Fluorescence lifetime measurements in isolated FMO have also revealed strong dependence on the redox conditions. It was further shown that this effect is supported by the cysteine (C-49 and C-353) residues in the bath that are located near some of the BChl a molecules. The thiol in the cysteine under oxidizing conditions gets converted to thiyl radical that further removes an electron from the excited BChl a.

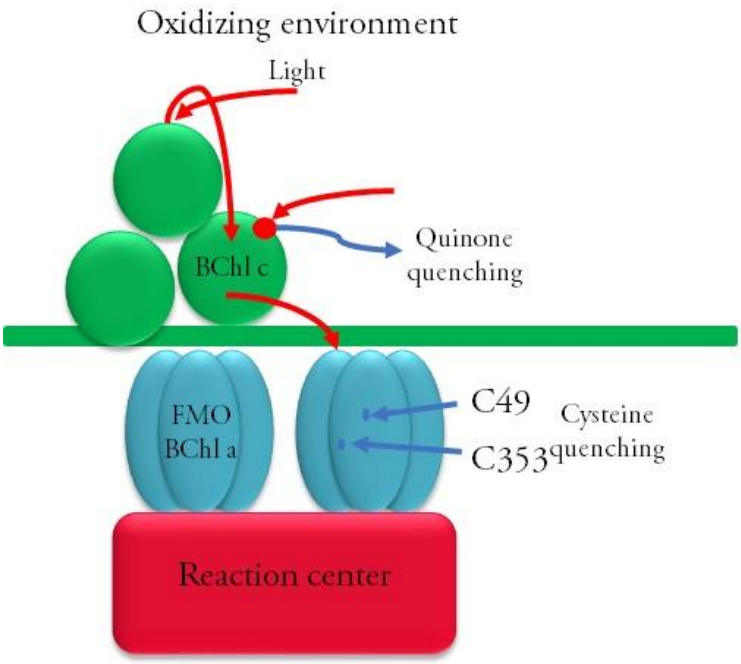

Figure 2.5. Dominant photoprotective mechanism in green sulfur bacteria employing changes in the redox potential. In BChl c, oxidizing conditions activate quinone isomerization. In BChl a of FMO cysteine-49 and cysteine-353 participate in excess energy quenching under oxidizing conditions.

pH-mediated quenching

Nonphotochemical quenching in green algae occurs through the light-harvesting complex stress-related protein (LHCSR) (30). Specifically in Photosystem II, LHCSR3 is responsible for quenching the excess energy in the high-light conditions. Upon excessive excitation the xantrophyll cycle is activated, upon which local pH is increased. Specifically, in Photosystem II, LHCSR3 is protonated. This further completes the xantrophyll cycle generating a quenching site in the membrane. In higher plants (Fig. 2.6), the protein responsible for activating the xantrophyll cycle is photosystem II subunit S (PsbS) (31). Both proteins are responsible for the conformational rearrangement of the thylakoid membrane that further facilitates the energy movement through charge and energy transfer. This is arguably the least understood quenching mechanism in biology,

and a lot of studies are underway to understand the location of the components that are responsible for the quenching.

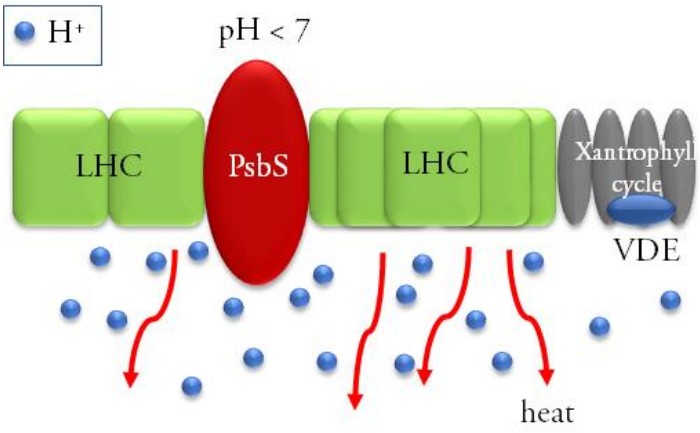

Figure 2.6. In green algae and higher plants, LHCSR and PsbS proteins respectively get activated in low pH conditions. Xantrophyll cycle is then turned on, where violaxanthin deepoxidaze (VDE) is responsible for deradicalizing BChl a in LHC

Understanding the mechanisms described above is essential to identifying conditions for artificial photosynthetic systems. Many organisms employ more than one type of mechanism, to facilitate long- and short-term protection. Moreover, high-light conditions are not the only requirements to activate photoprotection: nutrient deficiency, sudden and rapid change of environmental conditions add to the stress-related protection and complicate the studies of light-related mechanisms.

References

(1) R.E. Blankenship. Molecular mechanisms of photosynthesis. Blackwell Science, Malden, Massachusetts, 2002

(2) C.W. Cady, R.H. Crabtree, G.W. Brudvig. Functional models for the oxygen-evolving complex of Photosystem II. Coordination Chemistry Reviews, 252(3-4):444-455, 2008

(3) H. van Amerongen, L. Valkunas, R. van Grondelle. Photosynthetic excitons. World Scientific: Singapore, 2000

(4) A. N. Glazer. Light harvesting by phycobilisomes. Ann. Rev. Biophys. Chem, 14:47-77, 1985

(5) B.S. Rolczynski, H. Zheng, et al. Correlated protein environments drive quantum coherence lifetimes in photosynthetic pigment-protein complexes. Chem, 4(1):138-149, 2018

(6) S. Bailey, A. Grossman. Photoprotection in cyanobacteria: regulation of light-harvesting. Photochemistry and Photobiology, 84(6):1410-1420, 2008

(7) R. Berera, I.H.M. van Stokkum, et al. A mechanism of energy dissipation in cyanobacteria. Biophysical Journal, 96:2261-2267, 2009

(8) D. Tchernov, J. Silverman, et al. Massive light-dependent cycling of inorganic carbon between oxygenic photosynthetic microorganisms and their surroundings. Photosynthesis Research, 77:95-103, 2003

(9) C. Kami, S. Lorrain, et al. Light-regulated plant growth and development. Curr. Top Dev. Biology, 91:29-66, 2010

(10) K.K. Niyogi, Photoprotection revisited: Genetic and molecular approaches. Annu. Rev. Plant Physiol. Plant Mol. Biol. 50:333-359, 1999

(11) R.S. Knox. Förster's resonance excitation transfer theory: not just a formula. Journal of Biomedical Optics, 17(1), 011003, 2012

(12) T. Förster. Zwischenmolekulare Energiewanderung und Fluoreszenz. Annalen der Physik, 2:55-75, 1948

(13) A.G. Redfield. On the theory of relaxation processes. IBM Journal of Research Development, 1:19-31, 1957

(14) X. Chen, R.J. Sibley. Effect of correlation of local fluctuations on exciton coherence. The Journal of Chemical Physics, 132:204506, 2010
(15) M. Yang, G.R. Fleming. Influence of phonons on exciton transfer dynamics: comparison of the Redfield, Förster and modified Redfield equations. Chemical Physics, 282:163-180, 2002

(16) P. Rebentrost, M. Mohseni, et al. Environment-assisted quantum transport. New Journal of Physics, 11(3):033003, 2009

(17) G.S. Engel, T.R. Calhoun, et al. Evidence for wavelike energy transfer through quantum coherence in photosynthetic complexes. Nature, 446:782-786, 2007

(18) N.C.M. Magdaong, R.E. Blankenship. Photoprotective, excited-state quenching mechanisms in diverse photosynthetic organisms. J. Biol. Chem, 293(14):5018-5025, 2018

(19) B. Demmig-Adams, G.Garab, et al. Non-photochemical quenching and energy dissipation in plants, algae and cyanobacteria. Sprniger, Dordrecht, the Netherlands, 2014

(20) B.R. Green, W.W. Parson. Light-harvesting antennas in photosynthesis. Advances in Photosynthesis and Respiration, Vol.13, Kluwer Academic Publishers, 2003

(21) S. Bandara, Z. Ren, et al. Photoactivation mechanism of a carotenoid-based photoreceptor. PNAS. 114:6286-6291, 2017

(22) D. Harris, O. Tal, et al. Orange carotenoid protein burrows into the phycobilisome to provide photoprotection. PNAS, 113:E1655-E1662, 2016

(23) M. Sutter, A. Wilson, et al. Crystal structure of the FRP and identification of the active site for modulation of OCP-mediated photoprotection in cyanobacteria. PNAS, 110:10022-10027, 2013

(24) M. Gwizdala, R. Berera, et al. Controlling light harvesting with light, JACS, 138:11616-11622, 2016

(25) M.F. Hoffman-Marriott, R.E. Blankenship. Variable fluorescence in green sulfur bacteria. Biochim. Biophys. Acta, 1767:106-113, 2007

(26) N.-U. Frigaard, S. Takaichi, et al. Quinines in chlorosomes of green sulfur bacteria and their role in chlorophyll c aggregates. Arch. Microbiol. 167:343-349, 1997

(27) W. Zhou, R. LoBrutto, et al. Redox effects on the bacteriochlorophyll a-containing Fenna-Matthews-Olson protein from Chlorobium tepidum. Photosynth. Res. 41: 89-96, 1994

(28) G.S. Orf, R.G. Saer, et al. Evidence for a cysteine-mediated mechanism of excitation energy regulation in a photosynthetic antenna complex. PNAS, 113:E4486-E4493, 2016

(29) M.A. Allodi, J.P. Otto, et al. Redox conditions affect ultrafast exciton transport in photosynthetic pigment-protein complexes. JPCL, 9:89-95, 2018

(30) H. Xue, S.V. Bergner, et al. Novel insights into the function of LHCSR3 in Chlamydomonas reinhardii. Plant Signal. Behav. 10:e1058462, 2015

(31) M. Fan, M. Li, et al. Crystal structures of PsbS protein essential for photoprotection in plants. Nat. Struct. Mol. Biol., 22:729-735, 2015

CHAPTER 3

EXCESS ENERGY QUENCHING IN CYANOBACTERIAL PHYCOBILISOMES

3.1. Cyanobacteria as the oldest oxygenic photosynthetic organisms

Cyanobacteria, aka blue-green bacteria, are some of the oldest oxygenic prokaryotes known to date. For ~2.4 billion years cyanobacteria have played a key role in carbon and nitrogen fixation and generation of molecular oxygen and energy-rich carbohydrates (1). It is believed that cyanobacteria are responsible for converting the Earth's reducing atmosphere into an oxidizing one through photosynthesis, which largely benefited towards spreading of oxygen-tolerant organisms. This is known to be the Great Oxygenation Event (2). The photosynthetic functions are possible due to cyanobacteria's ability to harvest solar energy and convert it to useful chemicals in a chain of chemical reactions, collectively called as Calvin cycle (3). The vast diversity of cyanobacterial species accounts for all kinds of conditions they live in – from bottoms of the ponds to some of the driest environments encountered on Earth. It is the blooms of aquatic cyanobacteria that are responsible for the colors of some still bodies of water (4).

Typically, cyanobacteria are unicellular organisms, although there are species that are multicellular. They tend to have thick gelatinous walls protecting the DNA and photosynthetic machinery from the effects of their environment. The bacteria contain nucleoids in the form of DNA rings, ribosomes, carboxysomes and RuBisCO enzyme that are responsible for capturing carbon dioxide and reducing it respectively (Fig. 3.1). The photosynthetic machinery in cyanobacteria is represented by phycobilisomes attached to thylakoid membranes that are located

all around the cell. In fact, the shade of blue-green color of cyanobacteria is defined by the amount of phycocyanin protein – the component of phycobilisomes that is prevalent in their structure.

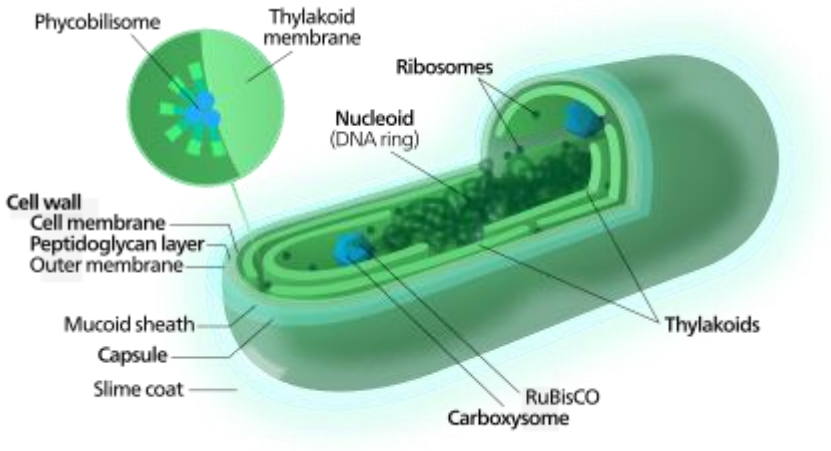

Figure 3.1. Generic structure of cyanobacteria. Thylakoids are bound to peripheral phycobilisomes that are responsible for light harvesting. Figure adapted from (41) within conditions set by Creative Commons License CC BY-SA 3.0

Peripheral phycobilisomes capture the solar energy and move it down the funnel to the thylakoid membrane that contains a reaction center, and photosystems I and II. The electron that is released from the reaction center is further sent to the Calvin cycle to produce carbohydrates, oxygen, or – depending on the type of bacteria – nitrogen or hydrogen (3).

Upon DNA-damaging stress, most cyanobacteria are known to be have DNA-repairing genes, thus allowing for DNA-repair (5). Through DNA-repair mechanisms cyanobacteria are capable of adapting to the new environments and spread further in the world.

Understanding oxygenic photosynthesis in model systems like cyanobacteria allows for designing methods for energy storage and transport in artificial systems. Mutagenesis is the first step to identify the portions of bacteria responsible for certain photosynthetic processes. Investigating the

changes in the bacteria structure in a billion-year-old evolution process of cyanobacteria can enable us to develop artificial photosynthetic systems alleviating the energy crisis and providing a source of clean energy for the ever-increasing demand of power for human needs.

3.2. Peripheral phycobilisomes

The entry point for sunlight in cyanobacteria is a light harvesting antenna called phycobilisome. These phycobilisomes have different structures depending on the organism they are present in, and the conditions the organism lives in. However, there is a generalized structure to phycobilisome antenna complex typically consisting of three types of phycobiliproteins (Fig. 3.2). These proteins are phycoerythrin (PE, bright red, abs. max. @560-580nm), phycocyanin (PC, bright blue, abs. max. @620nm) and allophycocyanin (APC, green, abs. max. @650-680nm) (6). All these proteins are well soluble in aqueous media. The phycobiliproteins are oriented in a way to allow the energy from the sunlight to flow downhill like in a funnel, meaning that PEs would be the first ones to interact with the light. Then the energy is passed down to PCs and further to APCs (3).

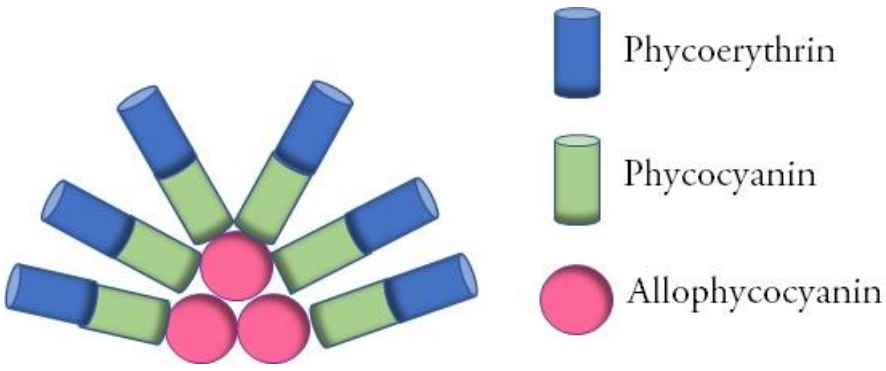

Figure 3.2. Generic structure of phycobilisomes. Phycoerythrin and Phycocyanin compose the rods, while allophycocyanin is present in the cylinders of the core. The amount of PE, PC and APC, as well as the amount rods and core cylinders varies depending on the organism.

The core is directly linked to the thylakoid membrane that contains the rest of the photosynthetic machinery. Many studies have shown the structural organization of these proteins to accommodate the energy flow. In phycobilisomes, there are two major components, collectively called as the rods and the core. The core is directly linked to the thylakoid membrane that contains the rest of the photosynthetic machinery. The rods typically contain PEs and/or PCs, while core primarily consists of APCs. The rods and the core are stabilized individually and bound together with non-chromophorylated linker proteins. Each of the phycobiliproteins has a mass between 15 and 25 kDa, and contains α and β subunits. These subunits contain the tetrapyrrole chromophores that absorb sunlight. The chromophores are associated with the phycobiliproteins and their absorption spectrum strongly depends on the conformation of the protein around them.

Microscopic studies show that the phycobiliproteins are assembled into trimeric discs or hexameric double discs (7). While PEs and PCs typically form hexamers, and APC are represented as trimers, the pH conditions can alter the configurations switching the structure between trimers and hexamers. Each disc is roughly 12nm in diameter and 3nm wide (8). Each rod consists of 3-4 hexamers of PE and/or PC depending on the organism. These rods are assembled onto a two- or three-cylinder core, each cylinder containing 4 trimers of APC. For instance, Synechocystis sp. PCC 6803 has six rods containing only phycocyanins, and three core cylinders containing APC (9). Alternatively, Porphyridium cruentum contains primarily phycoerythrins in the rods and APCs in the three-cylinder core (10). The species presented in this thesis is Synechococcus elongatus PCC 7942. Its detailed structure is presented in the next section, along with spectroscopic studies of the excess energy quenching in the phycobilisomes extracted from the organism.

3.3. Excess energy quenching in S. elongatus PCC 7942

This section is currently the manuscript in preparation, and is published in this thesis with permission from the authors.

3.3.1 Introduction

Cyanobacteria are important organisms in the biosphere that carry out nitrogen fixation, methanogenesis and oxygenic photosynthesis (11). The transfer-to-trap efficiency of cyanobacterial photosynthesis is remarkably high, and numbers between 80 and 95% are generally reported (3, 12). An energetic funnel in which photogenerated excitons move downhill from light harvesting antennae to the reaction center is responsible for the high transfer-to-trap efficiency (3, 13).

Cyanobacterial Photosystem II (PSII) and Photosystem I (PSI) reaction centers (RC) convert excitons at 680nm and 700nm respectively to separated charges, and the associated antenna complexes of cyanobacterial photosynthesis absorb all visible wavelengths shorter than 700nm efficiently. Carotenoid chromophores in the photosystems absorb the bluest wavelengths, and chlorophyll *a* molecules absorb the reddest. The spectral region between 550 and 700nm is covered by tetrapyrrole based phycobilin (PB) chromophores which are found in the antenna complex assembly known as the phycobilisome (PBS).

The PBS complex attaches to the stromal side of both PSI and PSII and funnels photogenerated excitons to them. Phycobilin chromophores are covalently bound to their water-soluble hycobiliprotein environments in the PBS complex. PB absorption properties are tuned exclusively by chromophore-protein interactions, and chromophore-chromophore interactions are negligible

in phycobiliproteins (14). FRET hopping describes exciton dynamics in the PBS complex and large interchromophore distances preclude other energy transfer mechanisms (15). The PBS structure for Synechococcus el. PCC 7942 is shown in Figure 1 along with its absorption spectrum. This PBS complex is made of six rods that are assembled onto a core. Each rod consists of three hexamers of the phycocyanin (PC) protein and each PC monomer binds three phycocyanobilin (PCB) molecules (9, 16) and the core consists of two tetramers of four trimers of the protein allophycocyanin (APC). The rods are connected to the core through linker proteins. PCB is the only phycobilin chromophore found in Synechococcus el. PCC 7942. Chromophore protein environments tune the absorption of PC to ~620nm and that of APC to ~650nm to maintain the energetic funnel (17).

The redox chemistry of the PSI and PSII reaction centers is typically slower than the photon absorption rate in high solar-fluence conditions (13, 18). On the ms timescale, abnormal focusing of sunlight at shallow water depths can also create a large imbalance between the photon absorption rate and the RC turnover rate (19, 20). In this scenario, numerous photoprotective strategies are employed to dissipate excess excitations without stressing the RC. For example, PSI RCs are surrounded by red chlorophylls, which absorb redder wavelengths than 700nm and hold funneled excitons to slow the exciton trapping process in the RC. A photoprotective role of these chlorophylls has been suggested (21). In Synechocystis sp. PCC 6803, a small protein called the Orange Carotenoid Protein (OCP) binds to the PBS complex to drive non-photochemical quenching of excess excitations (17, 22, 23). Intrinsic light-activated dissipation has also been shown in this species (24). However, the OCP is not found in Synechococcus el. PCC 7942, and the fate of excess excitations in this PBS complex is not as well-understood.

To observe excitation funneling from PC to APC in the PBS of Synechococcus el. PCC 7942 and pinpoint the site of excess exciton quenching, we perform fluence-dependent ultrafast broadband transient absorption measurements on isolated complexes in this work. This technique has been successfully used in the past to observe FRET frustration in Cy5 dyes on DNA (25), efficient exciton annihilation in monolayer MoS_2 (26), and decode exciton equilibration timescales in LHCII (27) trimers and LH2 membranes (28).

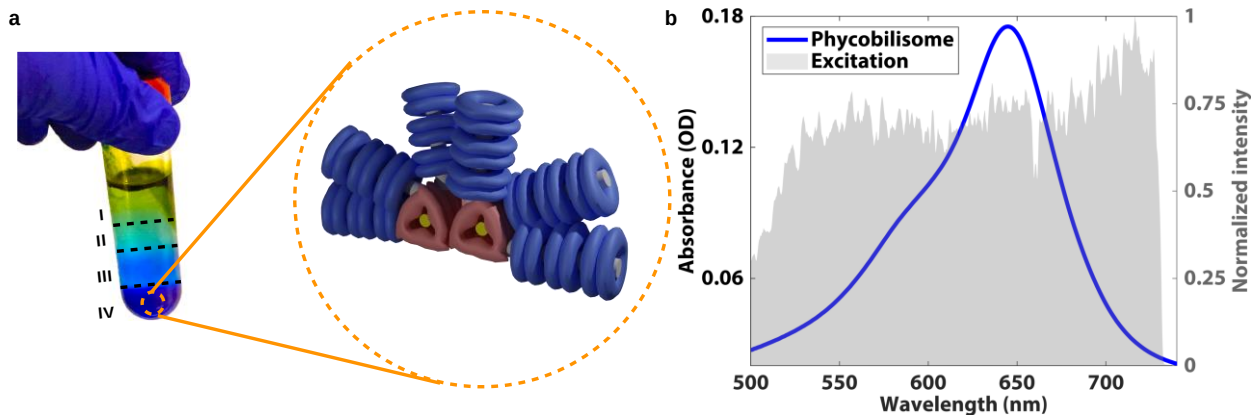

Figure 3.3: a) Phycobilisome isolated in the 1.5M sucrose layer and the structure of the Synechococcus el. PCC 7942 phycobilisome – the phycocyanin rods are shown in blue and the allophycocyanin core is shown in red. Linker proteins are shown in green and grey b) Absorption spectrum of the phycobilisome and laser spectrum used in study.

We look at pump fluence values corresponding to 250 W/m^2 to 2750 W/m^2 in comparison to the ~1000 W/m^2 value of solar fluence on a sunny day at the equator (3). Interestingly and counter-intuitively, we find that excess excitations created in the PC rods of the PBS are annihilated before they transfer to the APC core. The APC core has fewer chromophores than the PC rods (29, 30), and fast exciton equilibration within the rods in comparison to the PC to APC transfer timescale alleviates stress on these APC chromophores. Our transient differential transmission data for the

different pump fluences fits to a simple second order annihilation model well (26), and we recover exciton hopping times between PC chromophores with our model (14, 28). Our recovered hopping times are in excellent agreement with literature (15, 31).

3.3.2 Experimental Methods

Phycobilisome isolation: Phycobilisome complexes are isolated from wild-type Synechococcus elongatus sp. PCC 7942. Cells are grown in BG-11 medium under white room lights at room temperature. The isolation is adapted from the procedure of Kirilovsky and co-workers (32). Cells are pelleted for 40 minutes at 4000 rpm. The pelleted cells are resuspended in 1M potassium phosphate (KP) buffer and washed at 4000 rpm for 40 minutes multiple times before resuspension in minimal KP buffer. Visible impurities are removed after every wash. Resuspended cells are vortexed with glass beads in a 1:1 volume ratio of beads and suspension three times for 1 minute. To avoid local heating, the suspensions are placed on ice for 1 minute after every vortex cycle. The lysed cells are incubated for 30 minutes with Triton X-100 (2% v/v) at 28^{o}C in the dark. Phycobilisome supernatant is separated from cell and glass debris by centrifugation at 20000 rpm for 20 minutes. This procedure is repeated several times to maximize phycobilisome yield. The recovered supernatant is loaded on a discontinuous sucrose gradient of 1.5M, 0.75M, 0.5M and 0.25M sucrose in KP buffer (Figure 3.3a). The gradients are ultracentrifuged overnight at 24000 rpm. The deep blue 1.5M sucrose band is isolated and stored in -80^{o}C for subsequent spectroscopic measurements. Phycobilisome integrity is confirmed with gel chromatography (see Figure 3.6), fluorescence spectroscopy and circular dichroism (CD) spectroscopy (Figure 3.7). Our gel is in good agreement with an earlier reported gel of the PBS complex of Synechococcus el. PCC 7942

and shows a prominent PC band at ~20kDa, confirming that the PC complexes make it to the heaviest sucrose fraction as intact phycobilisomes (33).

Absorption, fluorescence, and circular dichroism spectroscopy: Absorption spectrum of the phycobilisome is obtained in a 1mm path length cuvette in an Agilent Cary 5000 spectrometer. Two-dimensional fluorescence spectra are obtained in a 1cm cuvette with 0.05OD sample in a Horiba JobinYvon Fluorolog-3 spectrophotometer. CD spectra are obtained in a 1mm cuvette on a 1.0 OD sample in a Jasco J-1500 CD Spectrometer.

Transient differential transmission spectroscopy: Sub-40 fs pulses centered at ~800nm with average power 2.7W and repetition rate of 5kHz are generated in a Ti:Sapphire Coherent Legend Elite regenerative amplifier seeded by a Coherent Micra Ti:Sapphire oscillator. The laser beam is focused in argon gas at 18psi. The resulting white light supercontinuum is compressed after extreme red and blue filtering to ~10 fs using an SLM based pulse shaper (Biophotonic Solutions Inc. MIIPSBOX640). A representative laser spectrum is shown in Figure 3.3b. The compressed pulse is split into pump and probe beams with a 90/10 beam-splitter. The pump beam is passed through a mechanical delay stage (Aerotech) and chopped at 2.5 kHz. The pump and probe were focused into a 200um sample cuvette and the beam size was characterized to be ~290um. The probe was then aligned to a Shamrock spectrometer and resolved at a Teledyne Dalsa Spyder 3 CCD camera. The pump energies are attenuated to 14nJ, 35nJ, 61nJ and 146nJ per pulse using neutral density filters for the annihilation measurements and probe intensity is attenuated by two orders of magnitude.

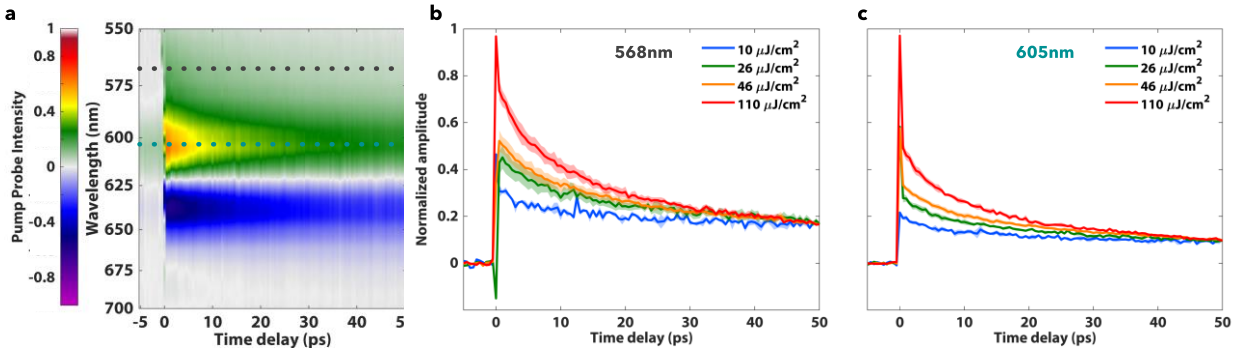

Figure 3.4: a) Averaged transient differential transmission map for the 46 μJ/cm^2 fluence. b) and c) Differential transmission as a function of pump-probe delay at 568 and 605nm for 10, 26, 46 and 110 μJ/cm^2 respectively.

3.3.3. Results and Discussion

Two main spectroscopic features are observed in the waterfall plot (Figure 3.4a) of the transient transmission data for all fluences: a decaying positive feature between 560 nm and 620 nm, peaking at 605 nm and a decaying negative feature red of 625 nm peaking at 632 nm. Here, positive features correspond to ground state bleach and stimulated emission signals and negative features correspond to photo-induced absorption signals. A strong fluence dependence of differential transmission signal decay is seen throughout the positive feature on the 50 ps timescale (Figure 3.4a). Weaker fluence dependence is seen in the negative feature and cannot be deconvoluted from the standard error of our measurements.

Pump-probe and time-resolved fluorescence studies have uncovered exciton dynamics in phycobilisome complexes of many cyanobacterial species. Earlier transient absorption studies also show prominent ground state bleach and photo-induced absorption signals in the phycobilisomes of Thermosynechococcus vulcanus (34), Synechocystis sp. PCC 6803 (17), and Arthospira platensis (35) in the same spectral region. The positive feature seen in our data has been previously

attributed to ground state bleaching of the PC and APC phycocyanobilin chromophores. Previous studies suggest that the red negative signature observed in the transient transmission plot is not caused by the excited state absorption of excited phycobilin molecules. Instead, an electrochromic shift of phycobilin chromophores neighboring excited chromophores has been suggested as the cause of this redshifted transient signal (35, 36).

Largely overlapping absorption spectra of phycocyanin and allophycocyanin chromophores lead to spectral congestion and make the deconvolution of phycocyanin specific dynamics difficult in this PBS complex (37, 38). To selectively observe exciton-exciton annihilation and decay dynamics in the PC rods, we look at the blue wavelength of 568 nm at which APC absorption is minimal (37). A previous pump-probe study on A. variabilis allophycocyanin trimers showed undetectable ground state bleach signal blue of 620 nm (39). We note that the deconvolution of APC specific dynamics is not possible in our data due to the strong PC-APC spectral overlap and the presence of the electrochromic photoinduced absorption signals at the reddest wavelengths. Fluence-dependent transient differential transmission plots at 568 nm for the different light fluences used in our experiment are shown in Fig. 3.4b. A dependence on the fluence is seen in the dynamics, with higher fluences leading to faster signal decays. This fluence dependence is also seen through the entire positive feature, but we restrict ourselves to the bluest signal region to prevent convolution of PC rod dynamics with APC core dynamics which are also excited in our broadband experiments. A biexponential fit (see Figure 3.9) for these curves yields a 7-10ps component (see Table 3.3), that remains relatively unchanged with fluence and a ~150ps time constant for the lowest fluences that systematically shortens to ~50ps with increasing fluence. Previous studies have attributed a 150-200ps time constant to exciton transfer from PC to APC

(35). This changing time constant confirms that a biexponential fit cannot explain the underlying dynamics, and higher order effects are at play.

To test if the fluence dependence arises from exciton-exciton annihilation, we first calculate the number of excitations on each rod for the four different light fluences (25, 37, 40). We obtain values of 0.5, 1.4, 2.4 and 5.7 initial number of excitations per rod, $N(0)$ for the 10, 26, 46 and 110 μJ/cm^2 fluences. We model the exciton-exciton annihilation process after a simple second-order differential equation (26):

$$\frac{dN(t)}{dt} = -\gamma_a N(t)^2 \quad (1)$$

where $N(t)$ is the number of excitations per rod at a given time t, and γ_a is the rate of exciton-exciton annihilation. Solving for $N(t)$ gives:

$$N(t) = \frac{N(0)}{1+\gamma_a N(0) t} \quad (2)$$

We fit the obtained transient differential transmission data for all fluences to this equation and the calculated $N(0)$ values. The fits of our data and the calculated initial number of excitations are shown in Fig. 3.5a. The annihilation rate is the unknown parameter in equation (2) and is obtained through our fits for the different fluences. A wide range of FRET hopping rates (500fs to 50ps) have been calculated for the PC rods (15), and annihilation likely occurs through a combination of these hops, with hopping between closest chromophores most likely to occur in the highest fluence.

Using the obtained exciton-exciton annihilation rate, we calculate the mean exciton hopping time for the four fluences using the formula (14, 28):

$$\gamma_a^{-1} = 0.5 * \eta * f_d * \tau_{hop} \quad (3)$$

where η is the total number of chromophores involved in the hopping process (54 per rod), f_d is the fractal dimension of the lattice on which exciton hopping occurs and τ_{hop} is the unknown parameter, the mean exciton hopping time. We assume f_d to be 1 for the phycocyanin rods because this value has not been calculated but ranges between 0.7 and 1 for most photosynthetic complexes (28). We obtain a τ_{hop} value of ~1.6ps using this formula. The chromophore lattice of phycocyanin rods is not ordered and its fractal dimension has not been reported to our knowledge. The hopping time obtained through our annihilation measurements is thus an approximate average of many different FRET hopping times that have been previously calculated and reported (14). Our fits coupled with the ~140ps time constant of PC to APC hops, confirm that the difference in fluence dependent dynamics at 568nm is seen due to exciton-exciton annihilation within PC rods and before transfer to APC cores.

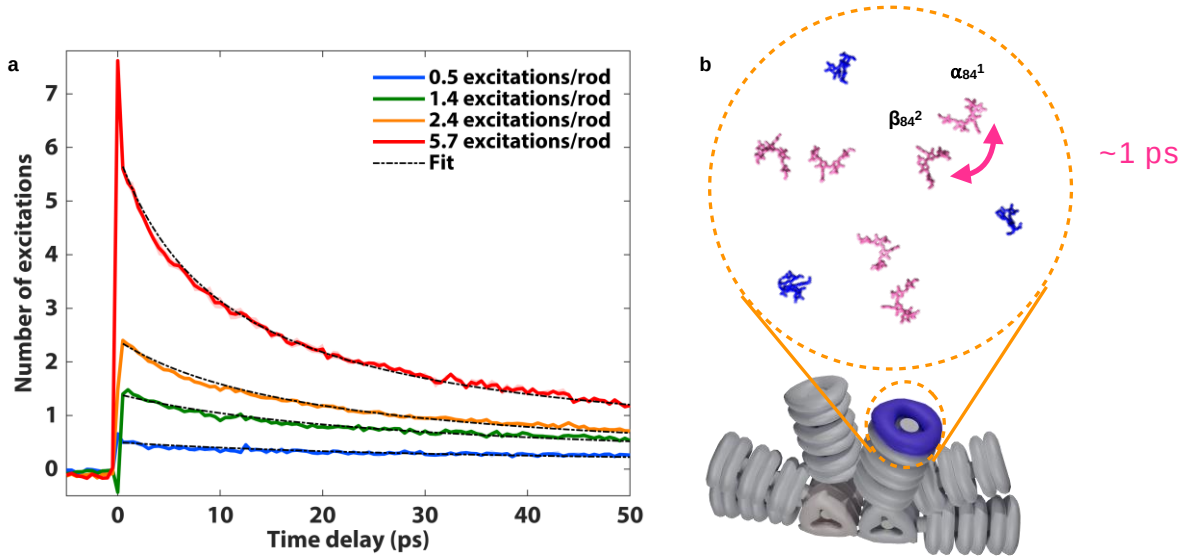

Figure 3.5: a) Second order fits for the transient differential data for the different number of excitations per rod calculated for our fluences b) Recovered hopping times off ~1 ps correspond to exciton hops between α_{84} and β_{84} (shown in pink) chromophores of adjacent monomers within a PC trimer.

In summary, we have shown that excess excitons created in the highest energy phycobilin chromophores in the cyanobacteria Synechococcus el. PCC 7942 are quenched through an exciton-exciton annihilation mechanism within the PC rods before they hop downhill to the APC core and then on to the photosystems. We show the viability of fluence-dependent pump-probe experiments in pinpointing sites of excess exciton quenching and modeling equilibration between isoenergetic and spectrally congested chromophore arrays. The photosynthetic design principle observed in our work prevents stress on the smaller APC cores, and on the photosystems which are also likely the sites of multiple exciton generation in the high solar fluence regime that we emulate in our experiments. This finding is especially relevant in the context of other phycobilisome quenching mechanisms, including OCP binding and fluorescence blinking (24) and shows that many layers of photoprotection have likely developed in the light harvesting phycobilisome complex.

3.4. Supplementary information

3.4.1 PBS integrity confirmation

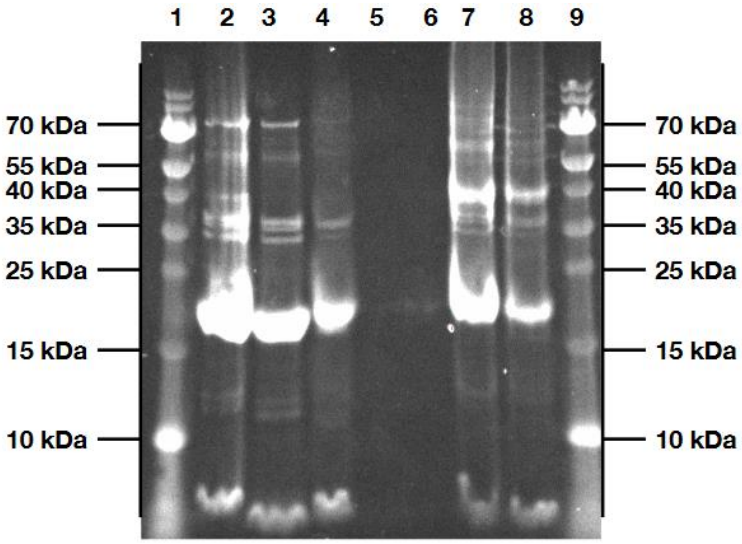

Figure 3.6. The sucrose gradient layer with the isolated phycobilisome was tested using SDS-PAGE for integrity. Gel was confirmed with Sato, et al. (33).

Lane Number	Details
1	Page Ruler – Prestained protein ladder – Thermoscientific 10 – 15 – 25 – 35 – 40 – 55 – 70 – 100 – 130 – 180 kDa
2	PBS + Gel Loading Buffer II (Denaturating PAGE) – 15 mins at 95 C.
3	PBS + Non-reducing Lane Marker Sample Buffer – 15 mins at 95 C
4	PBS native: not heated, no Sample Loading buffer
5	Blank
6	Blank
7	PBS + Non-reducing Lane Marker Sample Buffer – 15 mins at 95 C + Reducing Agent 2-Mercaptomethanol
8	PBS + Gel Loading Buffer II (Denaturating PAGE) – 15 mins at 95 C + Reducing Agent 2-Mercaptomethanol
9	Page Ruler – Prestained protein ladder – Thermoscientific 10 – 15 – 25 – 35 – 40 – 55 – 70 – 100 – 130 – 180 kDa

Table 3.1. SDS-PAGE lane descriptions

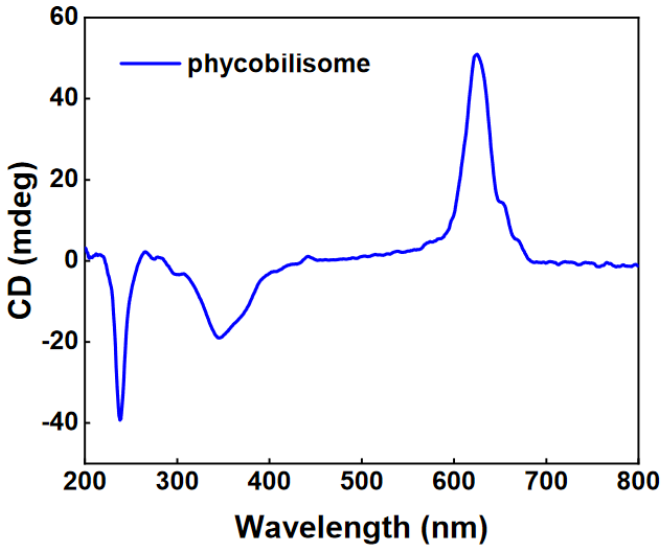

Figure 3.7. Circular dichroism spectrum of phycobilisome PCC 7942

3.4.2. Number of excitations in pump-probe experiment

In order to identify the amount of excitons generated upon excitation, we perform the calculation adapted form Dostal and co-authors (40). The following equation described the number of excitations per phycocyanin rod:

$$\frac{exc}{rod} = E_{pump} * A_{overlap} * \frac{\int Pump(\lambda) * \lambda * \left(1 - 10^{-A(\lambda)}\right) d\lambda}{hc \int Pump(\lambda) d\lambda} * \frac{1}{CN_A d}$$

Here, E_{pump} is the average energy of the pump pulse collected with Coherent LabMax-TOP powermeter, $A_{overlap}$ is the effective area of the pump and probe overlap, $Pump(\lambda)$ is the spectrum of the excitation pulse collected with Ocean Optics USB4000 Spectrometer, $A(\lambda)$ is the phycocyanin absorption spectrum, C is the molar concentration of the phycocyanin rods in the solution, N_A is the Avogadro's number and d is the thickness of the sample cell in pump-probe measurements.

3.4.3. Annihilation model fittings for multiple wavelengths in GSB region

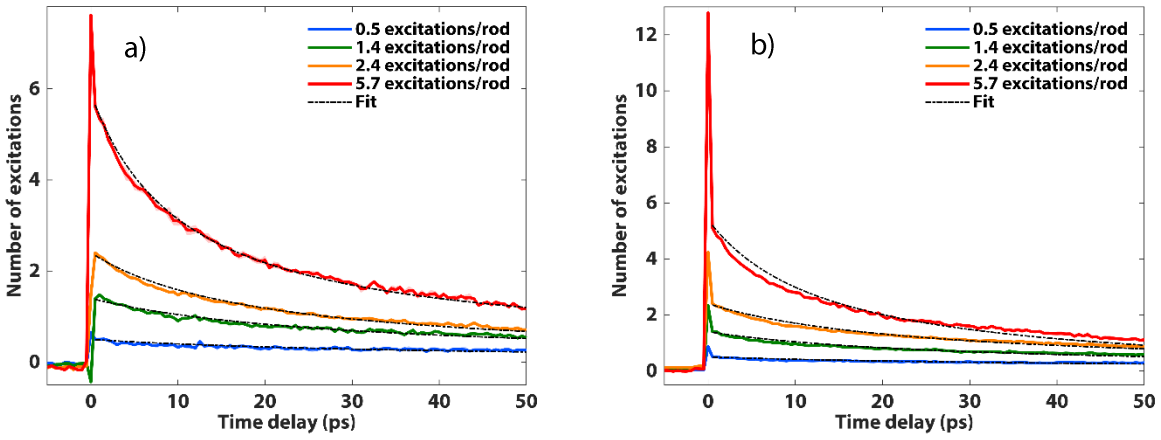

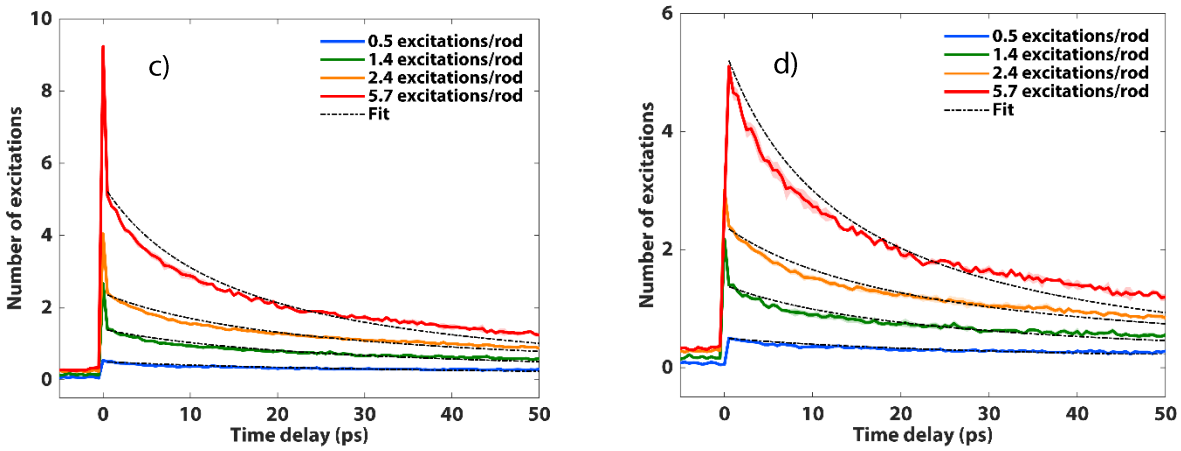

Figure 3.8. Fits to annihilation model at a) 568nm, b) 588nm, c) 596nm and d) 605nm. The quality of the fit decreases with the increased contribution from the allophycocyanin core.

		0.5 exc/rod	1.4 exc/rod	2.4 exc/rod	5.7 exc/rod
568nm	$\mathbf{R^2}$	0.72	0.95	0.98	0.99
	$\mathbf{k_{EEA}}$ **(1/fs)**	4.96×10^{-5}	2.44×10^{-5}	2.14×10^{-5}	1.49×10^{-5}
	$\boldsymbol{\tau_{hop}}$ **(ps)**	0.84±0.19	1.53±0.09	1.74±0.07	2.48±0.08
588nm	$\mathbf{R^2}$	0.80	0.92	0.96	0.96
	$\mathbf{k_{EEA}}$ **(1/fs)**	3.84×10^{-5}	2.51×10^{-5}	1.71×10^{-5}	1.16×10^{-5}
	$\boldsymbol{\tau_{hop}}$ **(ps)**	0.98±0.09	1.50±0.15	2.18±0.13	3.21±0.06
596nm	$\mathbf{R^2}$	0.75	0.91	0.94	0.94
	$\mathbf{k_{EEA}}$ **(1/fs)**	4.24×10^{-5}	2.58×10^{-5}	1.72×10^{-5}	1.06×10^{-5}
	$\boldsymbol{\tau_{hop}}$ **(ps)**	0.88±0.03	1.45±0.11	2.17±0.11	3.52±0.13
605nm	$\mathbf{R^2}$	0.75	0.90	0.94	0.93
	$\mathbf{k_{EEA}}$ **(1/fs)**	4.96×10^{-5}	3.01×10^{-5}	1.88×10^{-5}	1.15×10^{-5}
	$\boldsymbol{\tau_{hop}}$ **(ps)**	0.76±0.08	1.27±0.14	2.00±0.15	3.24±0.11

Table 3.2. Annihilation rates and hopping times from the annihilation model

3.4.4. Pump-probe biexponential fitting constants

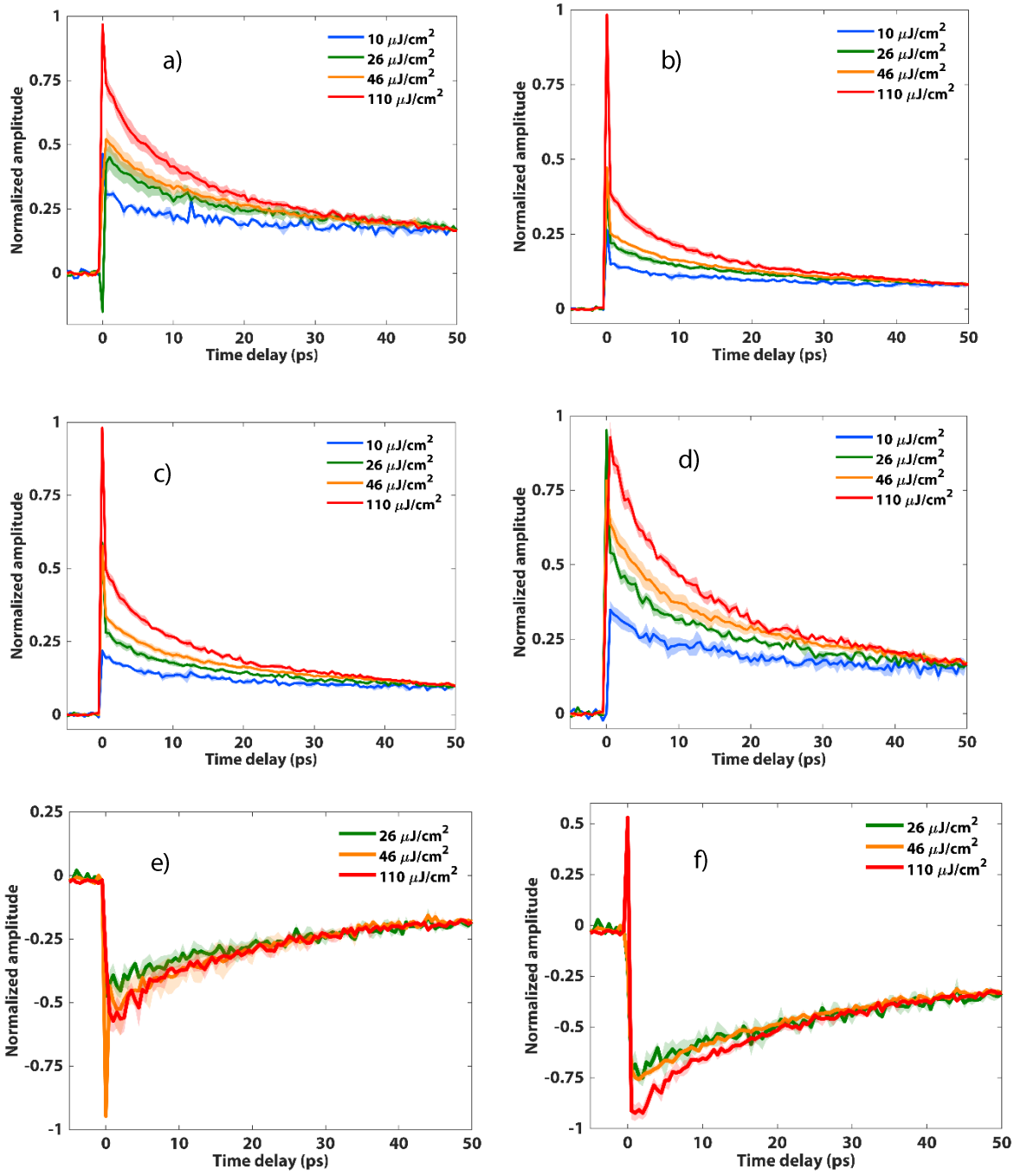

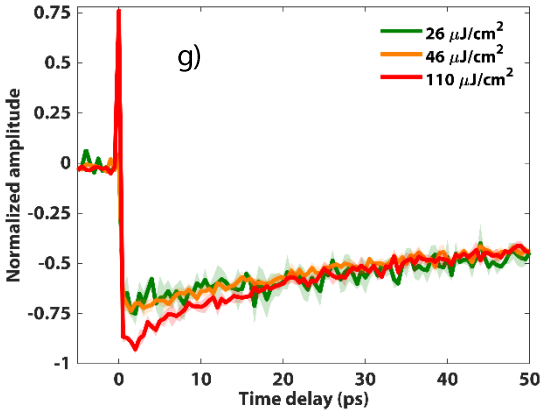

Figure 3.9. Pump-probe fluence dependence shown at a) 568nm, b) 588nm, c) 596nm and d) 605nm, e) 632nm, f) 642nm, g) 652nm.

Tables of fitting constants from the biexponential fit retrieved at different wavelengths

568nm

	R^2	**a_1**	**T_1 (ps)**	**a_2**	**T_2 (ps)**
10 μJ/cm^2	0.85	0.29	6.5	0.71	153
26 μJ/cm^2	0.98	0.42	11.3	0.58	140
46 μJ/cm^2	0.99	0.40	7.7	0.60	72
110 μJ/cm^2	0.97	0.49	7.0	0.51	50.2

588nm

	R^2	**a_1**	**T_1 (ps)**	**a_2**	**T_2 (ps)**
10 μJ/cm^2	0.74	0.28	8.02	0.72	206
26 μJ/cm^2	0.86	0.33	6.85	0.67	102
46 μJ/cm^2	0.85	0.36	7.50	0.64	88.5
110 μJ/cm^2	0.70	0.47	6.71	0.53	69.1

596nm

	R^2	**a_1**	**T_1 (ps)**	**a_2**	**T_2 (ps)**
10 μJ/cm^2	0.96	0.29	6.74	0.71	185
26 μJ/cm^2	0.78	0.35	6.84	0.65	110
46 μJ/cm^2	0.87	0.37	6.85	0.63	93.5
110 μJ/cm^2	0.87	0.47	6.90	0.53	81.9

605nm

	R^2	a_1	T_1 (ps)	a_2	T_2 (ps)
10 μJ/cm²	0.95	0.35	7.32	0.65	194
26 μJ/cm²	0.89	0.39	6.67	0.61	107
46 μJ/cm²	0.97	0.40	6.89	0.60	94.0
110 μJ/cm²	0.99	0.49	6.48	0.51	80.9

632nm

	R^2	a_1	T_1 (ps)	a_2	T_2 (ps)
10 μJ/cm²	0.49	0.14	5.78	0.86	112
26 μJ/cm²	0.93	0.45	19.3	0.55	168
46 μJ/cm²	0.79	0.99	52.2	0.01	48
110 μJ/cm²	0.97	0.68	19.8	0.32	65

642nm

	R^2	a_1	T_1 (ps)	a_2	T_2 (ps)
10 μJ/cm²	0.62	0.13	5.23	0.87	103
26 μJ/cm²	0.95	0.21	14.2	0.79	94.4
46 μJ/cm²	0.98	0.73	38.1	0.27	484
110 μJ/cm²	0.99	0.52	16.2	0.48	147

652nm

	R^2	a_1	T_1 (ps)	a_2	T_2 (ps)
10 μJ/cm²	0.19	0.03	5.29	0.97	149
26 μJ/cm²	0.75	0.0002	2.33	1	126
46 μJ/cm²	0.90	0.0006	113	1	117
110 μJ/cm²	0.97	0.55	28.6	0.45	536

Tables 3.3. Fitting constants for biexponential fits of the data at multiple wavelengths

3.4.5. Pump-probe spectra reproducibility

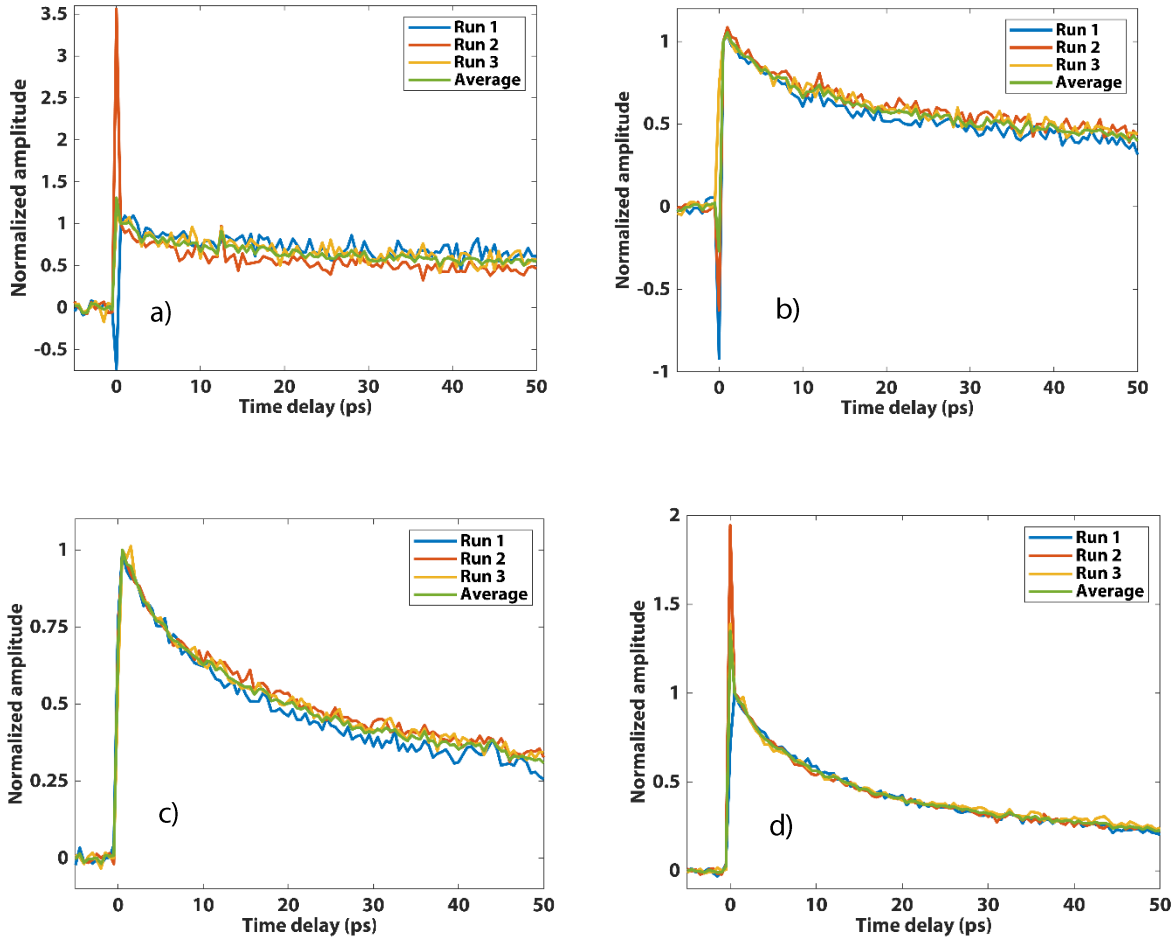

Figure 3.10. Reproducibility of pump-probe spectra at a) 0.5 excitations/rod, b) 1.4 excitations/rod, c) 2.4 excitations/rod and d) 5.7 excitations/rod

3.4.6. Long time dynamics in pump-probe spectra

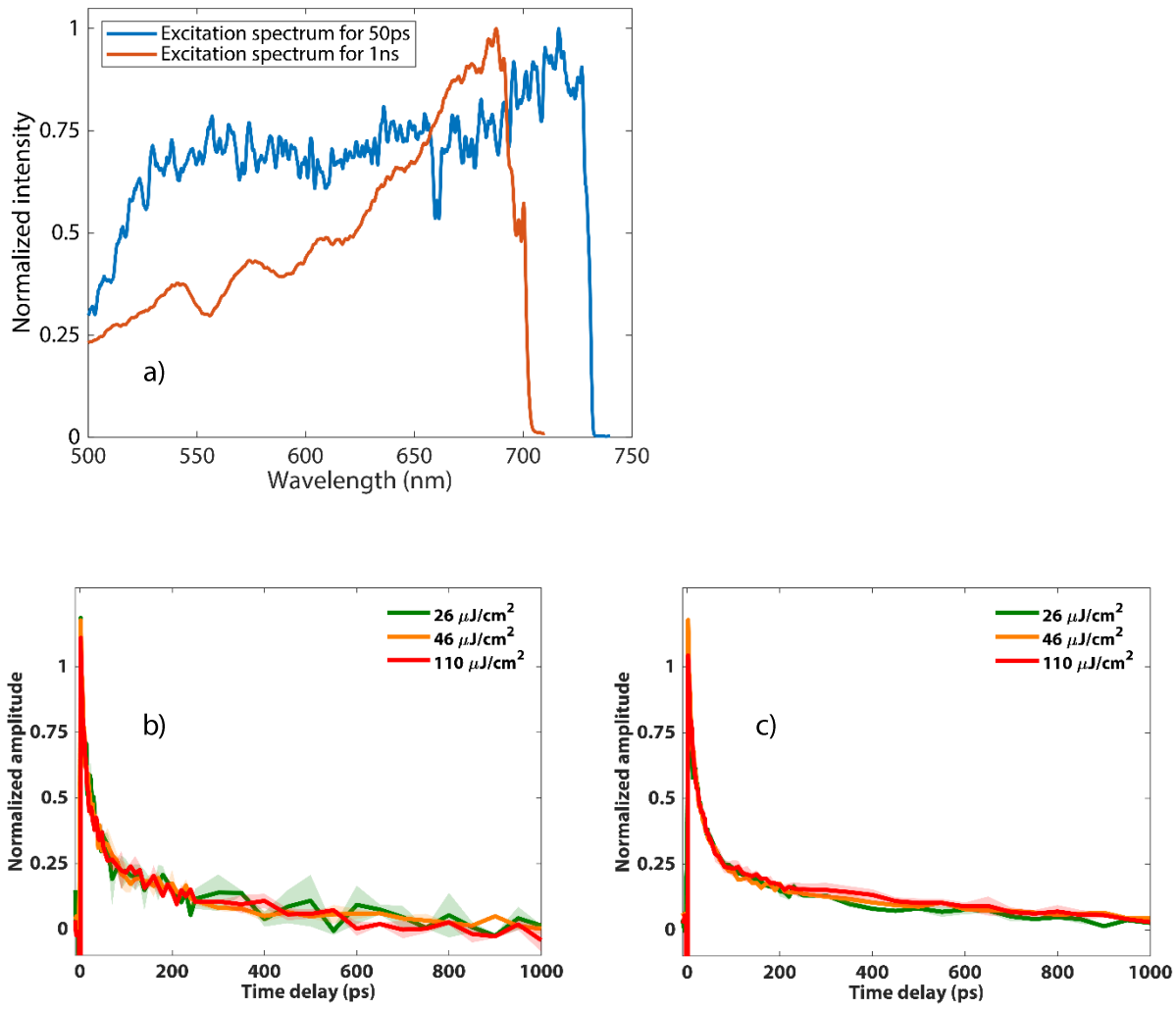

Figure 3.11. Pump-probe spectra collected to 1ns delays. a) Excitation spectra for 50ps vs 1ns spectra show the difference in relative excitations at various wavelengths; the overall number of excitations per complex remained the same throughout both measurements. b) 1ns spectra probed at 605nm. c) 1ns spectra probed at 632nm. In b) and c) the relatively low intensity of excitation light at blue wavelengths did not allow for collecting spectra at 568nm.

References

(1) P.G. Falkowski. Tracing oxygen's imprint on Earth's metabolic evolution. Science, 311:1724-1725

(2) L. Margulis, D. Sagan. Chapter 6, The Oxygen Holocaust. Microcosmos: Four billion years of microbial evolution. University of California Press, 1986

(3) R.E. Blankenship. Molecular mechanisms of photosynthesis. Blackwell Science, Malden, Massachusetts, 2002

(4) Govindjee, D. Shevela. Adventures with cyanobacteria: a personal perspective. Frontiers in Plant Science. 2(28), 2011

(5) C. Cassier-Chauvat, T. Veaudor, F. Chauvat. Comparative genomics of DNA recombination and repair in cyanobacteria: biotechnological implications. Frontiers in Microbiology, 7:1809, 2016

(6) A.R. Grossman, M.R. Schaefer, et al. The phycobilisome, a light-harvesting complex responsive to environmental conditions. Microbiological Reviews, 57(3):725-749, 1993

(7) A. Bennett, L. Bogorad. Properties of subunits of aggregates of blue-green algal biliproteins. Biochemistry, 10:3625-3634, 1971

(8) R. MacColl. Cyanobacterial phycobilisomes. Journal of Structural Biology, 124:311-334, 1998

(9) P.I. Calzadilla, F. Muzzopappa, et al. Different roles for ApcD and ApcF in Synechococcus elongatus and Synechocystis sp. PCC 6803 phycobilisomes. BBA Bioenergetics, 1860:488-498, 2019

(10) T. Redlinger, E. Gannt. Phycobilisome structure of Porphyridium cruentum. Plant Physiol. 68:1375-1379, 1981

(11) J. F. Kasting. Life and the Evolution of Earth's Atmosphere. Science, 296(5570): 1066–1068, 2002

(12) B. Green, W.W. Parson. Light-Harvesting Antennas in Photosynthesis; Advances in Photosynthesis and Respiration; Springer Netherlands, 2003

(13) G.D. Scholes, G.R. Fleming, et al. Lessons from Nature about Solar Light Harvesting. Nat. Chem., 3(10):763–774, 2011

(14) H. van Amerongen, R. van Grondelle, et al. Photosynthetic Excitons; WORLD SCIENTIFIC, 2000

(15) K. Sauer, H. Scheer. Excitation Transfer in C-Phycocyanin. Förster Transfer Rate and Exciton Calculations Based on New Crystal Structure Data for C-Phycocyanins from Agmenellum Quadruplicatum and Mastigocladus Laminosus. Biochim. Biophys. Acta BBA - Bioenerg., 936(2):157–170, 1988

(16) A. Marx, N. Adir. Allophycocyanin and Phycocyanin Crystal Structures Reveal Facets of Phycobilisome Assembly. Biochim. Biophys. Acta BBA - Bioenerg. 1827(3):311–318 2013

(17) I.H.M. van Stokkum, M. Gwizdala, et al. A Functional Compartmental Model of the Synechocystis PCC 6803 Phycobilisome. Photosynth. Res., 135 (1–3):87–102, 2018

(18) A.-M. A. Hays, I.R. Vassiliev, et al. Role of D1-His190 in the Proton-Coupled Oxidation of Tyrosine YZ in Manganese-Depleted Photosystem II. Biochemistry, 38(37):11851–11865, 1999

(19) H. Schenck. On the Focusing of Sunlight by Ocean Waves. J. Opt. Soc. Am. 47(7):653–657, 1957

(20) M. Darecki, D. Stramski, et al. Measurements of High-Frequency Light Fluctuations Induced by Sea Surface Waves with an Underwater Porcupine Radiometer System. J. Geophys. Res., 116:C00H09, 2011

(21) Y. Lee, M. Gorka, et al. Ultrafast Energy Transfer Involving the Red Chlorophylls of Cyanobacterial Photosystem I Probed through Two-Dimensional Electronic Spectroscopy. J. Am. Chem. Soc., 140(37):11631–11638, 2018

(22) A.H. Squires, P.D. Dahlberg, et al. Single-Molecule Trapping and Spectroscopy Reveals Photophysical Heterogeneity of Phycobilisomes Quenched by Orange Carotenoid Protein. Nat. Commun., 10(1):1172, 2019

(23) R. Berera, I.H.M. van Stokkum, et al. The Photophysics of the Orange Carotenoid Protein, a Light-Powered Molecular Switch. J. Phys. Chem. B, 116(8):2568–2574, 2012

(24) M. Gwizdala, R. Berera, et al. Controlling Light Harvesting with Light. J. Am. Chem. Soc., 138(36):11616–11622, 2016

(25) R.J. Mazuski, S.A. Díaz, et al. Ultrafast Excitation Transfer in Cy5 DNA Photonic Wires Displays Dye Conjugation and Excitation Energy Dependency. J. Phys. Chem. Lett., 11(10):4163–4172, 2020

(26) D. Sun, Y. Rao, et al. Observation of Rapid Exciton–Exciton Annihilation in Monolayer Molybdenum Disulfide. Nano Lett., 14(10):5625–5629, 2014
(27) V. Barzda, V. Gulbinas, et al. Singlet–Singlet Annihilation Kinetics in Aggregates and Trimers of LHCII. Biophys. J., 80(5):2409–2421, 2001

(28) P.D. Dahlberg, P.-C. Ting, et al. Mapping the Ultrafast Flow of Harvested Solar Energy in Living Photosynthetic Cells. Nat. Commun., 8(1):988, 2017

(29) A.R. Holzwarth. Structure-Function Relationships and Energy Transfer in Phycobiliprotein Antennae. Physiol. Plant., 83(3):518–528, 1991

(30) N. Adir, S. Bar-Zvi, et al. The Amazing Phycobilisome. Light Harvest.,1861(4):148047, 2020

(31) T. Gillbro, A.V. Sharkov, et al. Förster Energy Transfer between Neighbouring Chromophores in C-Phycocyanin Trimers. Biochim. Biophys. Acta BBA - Bioenerg. 1140(3):321–326, 1993

(32) M. Gwizdala, A. Wilson, et al. In Vitro Reconstitution of the Cyanobacterial Photoprotective Mechanism Mediated by the Orange Carotenoid Protein in Synechocystis PCC 6803. Plant Cell, 23(7):2631–2643, 2011

(33) T. Sato, S. Minagawa, et al. HtpG, the Prokaryotic Homologue of Hsp90, Stabilizes a Phycobilisome Protein in the Cyanobacterium Synechococcus Elongatus PCC 7942: Interaction of HtpG with an in Vivo Substrate. Mol. Microbiol., 76(3):576–589, 2010.

(34) C. Nganou, L. David, et al. Linker Proteins Enable Ultrafast Excitation Energy Transfer in the Phycobilisome Antenna System of Thermosynechococcus Vulcanus. Photochem. Photobiol. Sci., 15(1):31–44, 2016

(35) A. Fălămaș, S.A. Porav, et al. Investigations of the Energy Transfer in the Phycobilisome Antenna of Arthrospira Platensis Using Femtosecond Spectroscopy. Appl. Sci., 10(11):4045, 2020

(36) D.M. Niedzwiedzki, S. Bar-Zvi, et al. Mapping the Excitation Energy Migration Pathways in Phycobilisomes from the Cyanobacterium Acaryochloris Marina. Biochim. Biophys. Acta BBA - Bioenerg., 1860(4):286–296, 2019

(37) J. Grabowski, E. Gantt. Photophysical properties of phycobiliproteins from phycobilisomes: fluorescence lifetimes, quantum yields, and polarization spectra. Photochem. Photobiol., 28(1):39–45, 1978

(38) A.N. Glazer, S. Fang, et al. Spectroscopic Properties of C-Phycocyanin and of Its α and β Subunits. J. Biol. Chem., 248(16):5679–5685, 1973

(39) Y.J. Shiu, J.M. Zhang, et al. A Transient Absorption Study of Allophycocyanin. J. Chem. Sci., 114(6):611–621, 2002

(40) J. Dostál, F. Fennel, et al. Direct Observation of Exciton–Exciton Interactions. Nat. Commun., 9(1):2466, 2018

(41) Wikimedia Commons. File: Cyanobacterium-inline.svg - Wikimedia Commons, the free media repository. https://commons.wikimedia.org/wiki/File:Cyanobacterium-inline.svg, 2013

CHAPTER 4

DEVELOPMENT OF METHODOLOGY FOR PRECISE HAMILTONIAN MEASUREMENT AND CALCULATION

The following chapter is adapted with full permission from:

B.S. Rolczynski, S.H. Yeh, **P. Navotnaya, et al**. Time-domain line-shape analysis from 2D spectroscopy to precisely determine Hamiltonian parameters for a photosynthetic complex. Journal of Physical Chemistry B, 125(11):2812-2820, 2021

The SI for this research article is provided in the following link:

https://pubs.acs.org/doi/10.1021/acs.jpcb.0c08012

4.1. Overview

Fenna-Matthews-Olson (FMO) complex is a light-harvesting complex encountered in green sulfur bacteria. It is stable in bacteria in the form of a trimer, and facilitates the energy transfer from BChl c down to the reaction center. Each trimer consists of 8 BChl a chromophores in the site basis, and they form 8 excitons in the exciton basis. Each exciton is a combination of certain BChl a molecules that form an energy funnel. As one of the most studied pigment-protein complexes in photosynthesis, it provides a wealth of knowledge about energy transfer, photoprotection and quantum coherences. However, there is a debate in the FMO community about the participation of the 8^{th} exciton in the energy transfer down to the reaction center. Additionally, because it is so well studied, FMO is usually used as a model system for developing methodology to predict Hamiltonian of the system of interest. Both experimental and theoretical methods are being

developed based on the FMO knowledge to further use them in the less-studied systems. In this work, we use 2DES and HEOM along with new post-processing techniques to obtain the Hamiltonian of FMO complex and compare it to other existing models. I have contributed to the work in 2DES data collection and analysis.

4.2. Introduction

Optical spectroscopy can probe the energy levels and dynamics of chemical systems; but in complex systems, spectral broadening often complicates the analysis of the underlying electronic structure. Photosynthetic pigment-protein complexes are often challenging in this regard because they involve many identical, electronically coupled chromophores to perform electronic energy transport, yielding many optical transitions at similar frequencies. Despite the broadening, to understand the processes and dynamics in systems like these, it is important to understand the energies of the individual electronic states.

For instance, the energy levels have been pursued in the Fenna-Matthews-Olson complex (FMO). Like other pigment-protein complexes, FMO has attracted attention for its efficient energy transport, which is likely due to the proteins' abilities to control the alignment of their energy levels, coupling, and embedded chromophores' positions. FMO also has other convenient properties that contributed to its study, such as a linear absorption spectrum that overlaps well with the spectrum of a Ti:Sapphire light source, its history as the first photosynthetic protein to have a published X-ray structure (1), and its relatively simple structure for a pigment-protein complex. Its coherent quantum dynamics have been studied since 1998 (2, 3) and over that time, earlier interpretations have been supplanted by others that question the biological relevance (4).

However, the question of FMO's energy structure predates studies of its coherent dynamics, as knowledge of the energy structure is important to understand both its incoherent and coherent dynamics. The purpose of this study is to determine the energy levels of FMO's eigenstates.

FMO's Q_y band contains eight electronic energy levels in an 800 cm^{-1} window, and understanding the corresponding peak positions is important for simulating or understanding the dynamics of this system. In the last three decades, both the proposed exciton energies and the tools used to deduce them have advanced. In 1992, Pearlstein et al. applied a fit to the linear absorption spectrum of FMO to obtain peak positions (5). Later studies in that decade considered additional evidence such as linear dichroism (6), circular dichroism (7), and transient absorption spectra (8). More recent studies employed 2D spectroscopy, genetic algorithms, and quantum mechanical models (9 – 13). In 2009, an eighth bacteriochlorophyll site was reported in FMO, causing renewed investigation of the electronic energies because previous investigations had assumed that only seven peaks composed the spectrum (14). Subsequently, the energy level and dynamics of the eighth exciton were studied using a combination of experimental and theoretical techniques (15 – 17). Mutagenesis was used to knock out individual sites, and the resulting linear absorption and circular dichroism spectra were measured (18). While this method was revealing, mutations can also have side effects on neighboring sites and their vibrational couplings (19). Milder and co-workers have provided a review of many of these studies (19). While this sustained effort has made substantial progress in deducing the eigenenergies, it would be beneficial to observe the peak positions directly.

When excited optically, coupled chromophores emit a signal according to their excitonic transition energies and oscillator strengths. Rapid fluctuations of the energy levels over time can result in

decoherence (21). Stochastic, multimode, Brownian oscillator models provide analytical descriptions for these processes (22). These models describe exponential or Gaussian time-domain decay functions in the homogeneous or inhomogeneous broadening limits, respectively, and provide useful rules of thumb for the spectral characteristics in these limits.

Here, we take advantage of these dynamics to identify peak positions within the spectra. We acquire 2D electronic spectra of the Fenna-Matthews-Olson complex using a previously described non-collinear 2D spectrometer (23). In this spectroscopic method, the sample interacts with light four times, and the signal is measured as a function of the time delays between each of these interactions. These are known as the coherence-, waiting-, and rephasing-time domains, respectively. When the coherence- and rephasing-time domains are converted to their respective frequency domains by Fourier transform, 2D spectra are obtained as a function of the waiting time, which is analogous to the time delay in a transient absorption experiment.

The coherence- and rephasing-time domain dynamics discussed here are different from the waiting-time dynamics that have often been debated previously (4, 24). Whereas these discussions often involve signals that beat with respect to waiting time, due to zero-quantum coherences within that time domain, the signals we discuss here are one-quantum coherences in the coherence- and rephasing-time domains. Questions about the signal attribution in the waiting-time domain arise, in large part, because of the many possible electronic and vibrational configurations a system (initially in its ground state) can access after two interactions with light. The possibilities include vibrational wavepackets within a single ground or excited electronic state, electronic coherences between distinct excited states, and more variations such as vibrons that involve mixed electronic and vibrational states (9, 25, 26). In FMO, the spacing between vibrational modes, and those

between the excited electronic states, are similar in energy, so the assignment of particular beating signals to coherences between vibrational, electronic, or vibronic states requires care and has elicited debate. However, this issue is particular to the ambiguous contributions of the electronic and vibrational states to the zero-quantum signal patterns, which only appear in the waiting-time dynamics. In contrast, neither the coherence- nor rephasing-time domains feature zero-quantum coherences.

This study seeks the Hamiltonian's eigenvalues regardless of which physical states (electronic, vibrational, or vibronic) compose them. Its approach is to use a method that selectively filters the signal components producing the most spectral broadening, in order to deduce the peak positions of otherwise highly overlapping peaks within the spectra. By the use of 2D spectroscopy at 77 K, weak but persistent signals remain 1 ps after excitation from the coherences between the ground and excited states. Because of the low temperature and the low intensity of these signals, their existence at 1 ps does not address discussions of functionally or biologically relevant dynamics, but this study will demonstrate that the signals can nonetheless be used to distinguish overlapping spectral features in the optical spectra. A time-domain filtering method (27) is used to isolate narrowed spectral peak contributions in experimentally measured spectra and determine the eigenenergies of the system by direct observation. This method is first tested on calculated spectra obtained using the hierarchical equations of motions (HEOM) (28), which produces accurate spectral line shapes within the Drude approximation applied here.

4.3. Experimental methods

Sample preparation. FMO was extracted from C. tepidum, as described previously (29). It was prepared at pH = 8.0 in a 800 mM Tris-HCl buffer with 50 mM NaCl and 0.1% lauryldimethylamine oxide, and prepared in a 65:35 glycerol:buffer ratio. Subsequently, it was loaded into a cuvette treated with Sigmacote (Sigma Aldrich), with a path length of 200 μm. The sample was vitrified and held at 77 K using a liquid nitrogen cryostat.

Two-dimensional electronic spectroscopy. Using a spectrometer that was described previously (23), two-dimensional spectra were acquired from the FMO sample at 77 K. In this technique, four beams are incident on the sample in a boxcar geometry, with controlled time delays, resulting in a signal from the sample. Beams 1-3 interact with the sample once each, while the fourth beam is highly attenuated and acts as a local oscillator (30). The time-delays between the 1-2, 2-3, and 3-signal pulse pairs are the coherence (τ), waiting (T), and rephasing (t) times, respectively. For further information about the experimental design, see Sec. 1 of the Supporting Information (link above). The coherence time spanned -1001 to 2002 fs in 3.5 fs steps, while the waiting time spanned 0 to 1860 fs in 30 fs steps. The step size in coherence time induces aliasing. Nonetheless, it was selected in order to make the scan feasible using the picoseconds-long range in both the coherence- and waiting-time domains. With the current parameters, each complete set of 2D spectra took ~24 hours to measure. Prolonging a single experiment much longer than that risks laser instability, cryostat failures, sample degradation, and other faults. For further discussion of the aliasing, see Section 7 in the Supporting Information (link above).

The rephasing and non-rephasing components of the signal are measured at the positive and negative regions of τ, respectively. Data along the rephasing-wavelength domain were measured by spectral interferometry of the signal and local oscillator pulses (30). The pulses were compressed to 14 fs (fwhm), with a repetition rate of 5 kHz and a fluence of 640 pW/μm^2 within a 100 μm diameter. Scatter-subtraction was accomplished by using shutters in beams 1 and 2 together, and separately in beam 3, and by using these resulting signals to perform background subtraction (3).

Hierarchical equations of motion. The HEOM calculations were performed using previously published methods (see Section 1 of the Supporting Information, link above) (16, 28, 31, 32) to calculate the 2D spectra shown subsequently in Figure 4.1, as well as Figures S2 and S5 in the Supplemental Information. A weighted average is obtained of the seven- and eight-site spectra assuming a 1/3 site VIII occupancy, reflecting the fact that site VIII is not as tightly bound as the other chromophores and can be absent from some of the proteins in the ensemble (15). This model applies a Drude spectral density model, without the addition of embedded peaks representing the influence of particular additional vibrational modes, which could increase decoherence rates. However, the signal components investigated here, which persist at 1 ps, are already recognized to be a small portion of the power spectrum, and the approach used here does not depend on their having a large intensity as long as they can be measured.

4.4. Results and Discussion

In the coherence- and rephasing-time domains, signals appear as damped, sinusoidal time series (22). The line shape function initially decays often within tens to a few hundred femtoseconds, with a shape that is nearly Gaussian and/or exponential, but under the experimental conditions used here, this function has a tail that persists weakly to 1 ps. By focusing on the tail of this function, we can narrow the spectral line width. This benefit comes at the expense of the signal intensity.

The damping occurs due to interactions between the electronic system and its environment, potentially leading to multiple, distinct broadening contributions. When the environment is modeled by multiple harmonic oscillators undergoing Brownian motion, the homogeneous broadening contributions occur in the limit of strong electronic-nuclear interactions (Δ) and slow vibrational relaxation rates (Λ), while the opposite conditions produce inhomogeneous broadening contributions (22). This model also continuously interpolates between these limits. The homogeneous and inhomogeneous contributions dominate different regions of the coherence- and rephasing-time domains. This damping is represented by the dephasing term $g(t')$ (eq. 1). After expanding in a Taylor series and application the conditions specified above for Δ and Λ, $g(t')$ reduces to eqs. 2 and 3 in the inhomogeneous and homogeneous limits, respectively (22).

$$g(t') = \left[\left(\frac{\Delta}{\Lambda}\right)^2 - \frac{i\lambda}{\Lambda}\right][exp(-\Lambda t') + \Lambda t' - 1] \qquad \text{(equation 1)}$$

$$g(t')_i = \frac{\Delta^2}{2} t'^2 \qquad \text{(equation 2)}$$

$$g(t')_h = \left(\frac{\Delta^2}{\Lambda} - i\lambda\right) t' \qquad \text{(equation 3)}$$

Here, λ is the electronic-nuclear coupling strength, and t' is the given time domain (τ, T, or t). In the time-domain signal, eqs. 1-3 are applied as a decaying signal envelope by multiplication of $\exp\left(g(t')\right)$ to the undamped time-domain signal (22). $g(t')_i$ is proportional to t'^2 and yields a Gaussian envelope in the conjugate Fourier domain, while $g(t')_h$ is proportional to t' and yields an exponential decay in it. If all else is equal, the Gaussian contribution dominates at early time delays but quickly decays, while the exponential term persists afterward and therefore dominates at later times.

2D spectra of FMO were obtained both experimentally and computationally, as described in Section 4.2. Representative experimental rephasing-time-domain data are shown with line cuts at ω_τ = 12102, 12261, 12337, 12425, 12543, 12596, 12627, and 12712 cm^{-1} (Fig. 4.1). These wavenumbers subsequently will be assigned to excitons 1-8 in FMO.

Weak signal components persisting at 1 ps are evident in these time series. Our strategy is to use the Lorentz-Gauss filter to emphasize this long-lived signal component, in order to obtain more narrow spectral peaks.

To accomplish spectral narrowing, a coherence- and rephasing-time-domain filter is applied to reduce the influence of the strongest damping contributions. This general method is discussed by Hamm and Zanni in the context of 2D infrared spectroscopy (33), and here it is applied in 2D electronic spectra. Furthermore, coherence-time-domain data have previously been filtered in simulated 2D spectra to obtain information about the energy- or charge-transfer dynamics in diatomic or generic two-state systems (34, 35), to assign vibronic contributions in simulated spectra of FMO (36), and to observe its electronic-environmental interactions (37).

We use a filter similar to a Lorentz-Gauss function that was reported previously in NMR to produce narrow peak widths (27). A Lorentz-Gauss filter $L(t')$ contains Gaussian and exponential components (eq. 4).

$$L(t') = \exp\left(\ln 2 \frac{t'-t_0'}{a}\right) \exp\left[-\frac{\ln 2}{4a}\Gamma^2(t'-t_0')^2\right] \qquad \text{(equation 4)}$$

Here, t_0' is the lag time, Γ is a line-width reduction ratio, and a corresponds to the decay rate of the signal envelope. The subsequent analysis will show that applying $L(t')$ reveals peaks at their expected wavenumber positions in the 2D spectra. These expected positions are known exactly because, in the calculated spectra, the Hamiltonian is an input parameter. Unlike the original application of this filter in NMR, which exclusively sets t_0' = 0, we set t_0' > 0 to reduce the fastest-decaying components of the signal envelope, which contribute the most to spectral broadening (27). The experimental data are initially phased as discussed in section 6 of the Supporting Information (link above), while spectra calculated from HEOM do not require phasing. The Lorentz-Gauss filter is subsequently applied to both the coherence- and rephasing-time domains. Subsequent application of a Fourier transform with respect to the coherence and rephasing times yields the filtered 2D spectra. For further consideration of noise and vibrational mixing effects, see Sec. 8 of the Supporting Information.

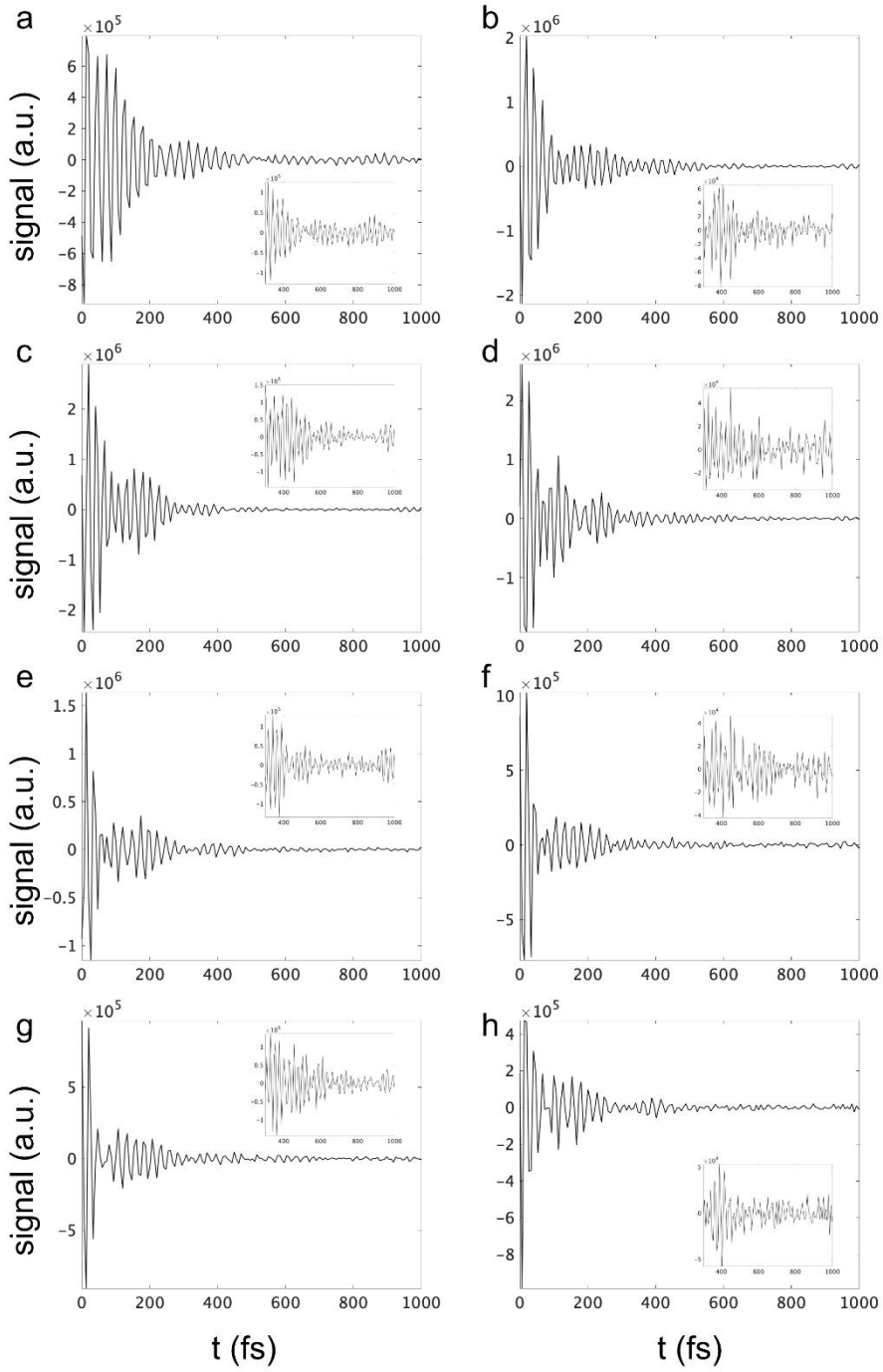

Figure 4.1. Measured rephasing-time-domain line-shapes are shown at $\omega_\tau =$ 12102, 12261, 12337, 12425, 12543, 12596, 12627, and 12712 cm^{-1} (a-h), which subsequently will be obtained as the exciton energies in FMO. The insets focus on the range from 300-1000 fs, to show the small signals that persist in that range. For reference, corresponding measured 2D spectra are shown in Fig. 4.3. The signal components persisting to 1 ps are a small component of the overall power spectrum.

HEOM treats the system-environment interactions of an individual complex explicitly using an Ohmic coupling model. The Lorentz-Gauss filter was applied to the calculated FMO spectrum. The Hamiltonian was constructed by using the values from Cho et al. for BChl a sites I-VII (9), plus an additional eighth site. Like the other sites, the off-diagonal elements of this eighth site were determined by modeling the dipole-dipole interactions (38) using coordinates from the X-ray structure of FMO from C. tepidum (PDB: 3ENI) (14). Site VIII was assigned to ω_{VIII} = 12700 cm^{-1}, and 2D spectra were calculated as described in Section 4.2 and Sec. 1 of the Supporting Information (Fig. 4.2). As t_0' increases, the individual peak frequencies become apparent at many diagonal- and cross-peak positions. We note that the calculated spectra were only intended to test outcome of the Lorentz-Gauss filtering, so a previously published Hamiltonian was used, except for the addition of site VIII as indicated.

The peak positions correspond to the expected values, based on the input Hamiltonian. At t_0' = 500 fs, significant negative shoulders appear at some of the peaks, so we use t_0' = 300 fs for the subsequent analysis and expect slight negative valleys in between spectral features. For further tests of the filtering method, see Sec. 3 of the Supporting Information.

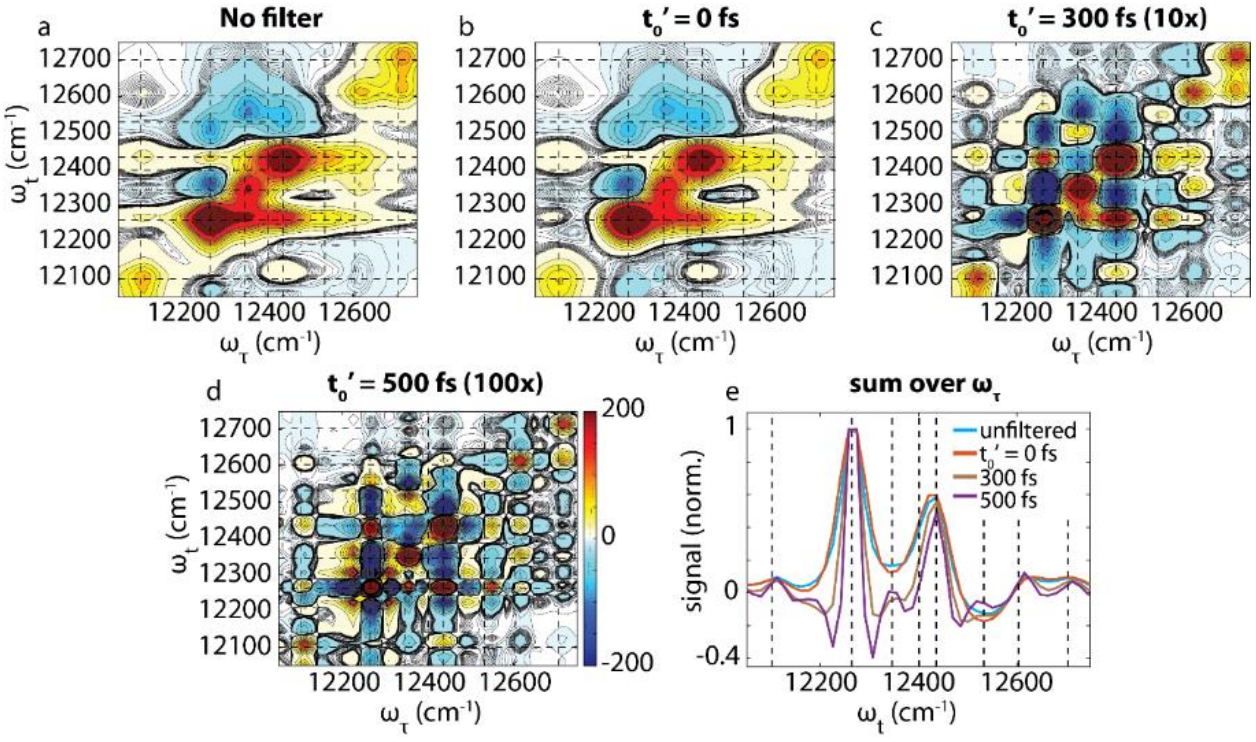

Figure 4.2. (a-d) 2D spectra of FMO are shown, which were calculated using HEOM. The application of the Lorentz-Gauss filter distinguishes peak positions, according to the parametrization of t_0'. The total signal diminishes as t_0' increases, so the color bar limits have been reduced by factors of 10 or 100 in panels c or d, respectively. (e) The normalized spectra are shown after summation over ω_τ. In each panel, black dotted lines represent the known exciton wavenumbers from the input Hamiltonian. They are not obtained by spectral fits. In these plots, the phased rephasing spectra are shown at T = 270 fs.

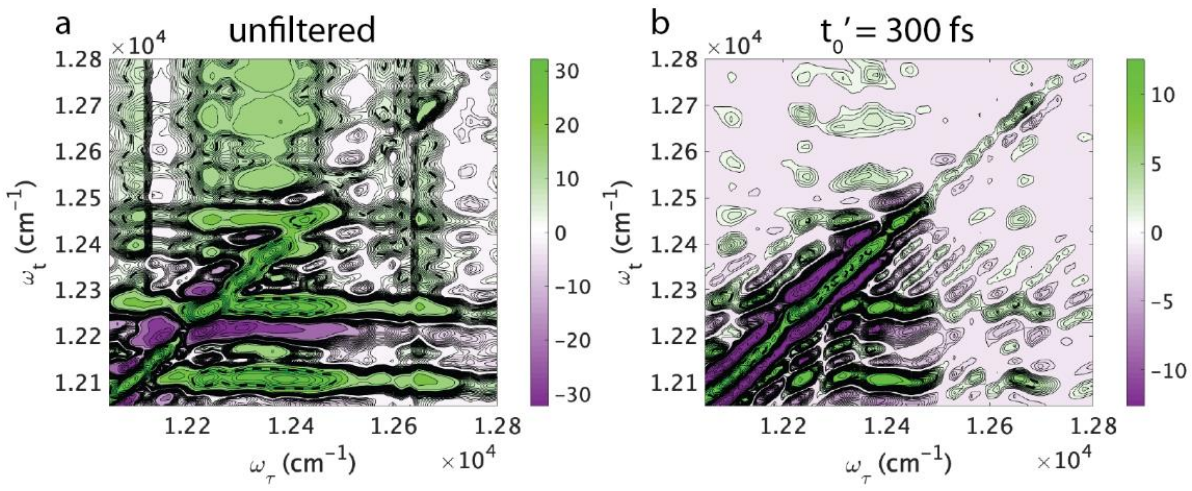

Figure 4.3. The underlying spectral peaks of the heavily overlapping regions within the spectrum can be resolved using the Lorentz-Gauss filtering method. The enhancement is especially evident, for example, in the area of 12100 – 12400 cm^{-1} in both frequency domains. Measured 2D combined (rephasing and non-rephasing) spectra of FMO are shown after averaging over T to improve the signal-to-noise ratio. (A representative unaveraged spectrum is shown in Fig. S6, Supplemental Information). The "unfiltered" spectrum was obtained without the Lorentz-Gauss filter, but the interferograms before beam 3 and 1000 fs after beam 3 were still apodized, to remove beam scatter, and the remaining signal was multiplied in the time-domain by a Hanning window function. The other spectrum was obtained by applying the Lorentz-Gauss filter at t_0' = 300 fs, as well as these other treatments. The dotted, black lines indicate cut-offs where the contour step size has been increased, for clarity.

The Lorentz-Gauss filter is applied to the experimentally obtained time series at t_0' = 300 fs (Fig. 4.3). All else being equal, a faster decay envelope in the time domain corresponds to broader peaks in the corresponding wavenumber domain. Many diagonal- and cross-peaks become apparent at t_0' = 300 fs. As a cautionary note, while random noise does not appreciably affect the signal in the optical spectral range (Fig. S8 in the SI), the diminished signal will still lower the S/N ratio. There are two ways that the approach used here can do so. First, because the coherence-domain range spanned picoseconds instead of a few hundred femtoseconds, it introduced more low-signal contributions at the later time delays. As a result, the noise contribution is larger, compared to

spectra obtained by using a few hundred femtosecond coherence-time range. Second, the Lorentz-Gauss filter can amplify some of the region at later time delays where the signal intensity is lower (Fig. S4 in the SI), while diminishing the highest-intensity part of the signal near time zero. This effect also diminishes the signal more than the noise. As a result, the signal maxima are lowered with respect to the background.

Figure 4.4 shows the individual rephasing and non-rephasing contributions to the 2D spectra. Although the rephasing and non-rephasing spectra look distinct due to their different Liouville pathways, their peak positions are both derived from the same energy levels within the chemical system, and therefore these positions should coincide.

To compare these peak positions, first the rephasing and non-rephasing spectra are reduced to an easily comparable format by summing over ω_τ and T, yielding a data set along ω_t (Figure 4.5b). The peaks' wavenumber positions obtained using this method are 12102, 12167 , 12261, 12337, 12425, 12543, 12596, 12627, and 12712 cm^{-1}. At t_0' = 300 fs, many of the peaks are distinguished in both the rephasing and non-rephasing spectra (Fig. 4.5).

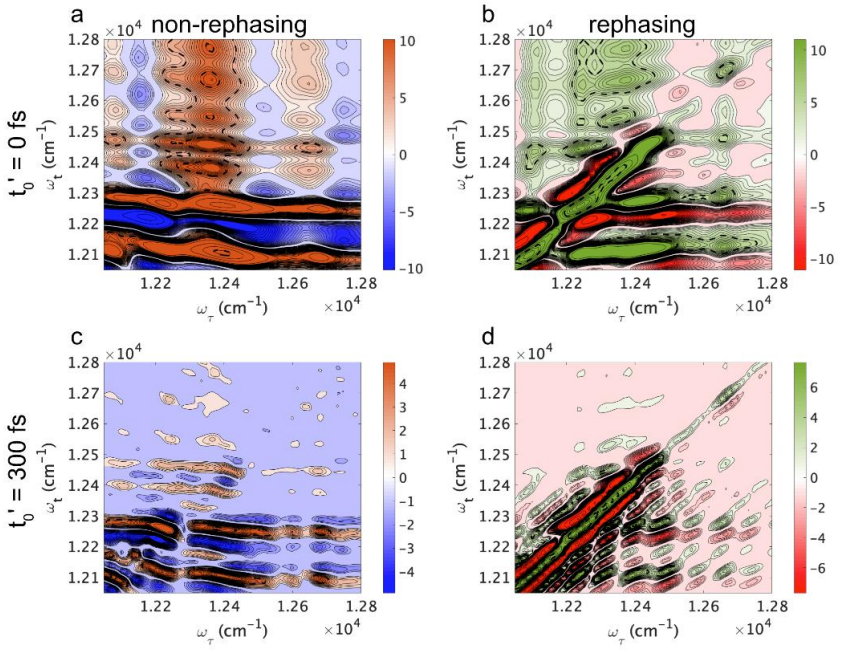

Figure 4.4. The rephasing and non-rephasing components of the measured 2D spectra for FMO are shown, after summation over T. The t_0' position is set to either 0 (top) or 300 fs (bottom), and the rephasing ($\tau > 0$ fs) or non-rephasing ($\tau < 0$ fs) components of the spectra are indicated in the figure. The more distinct peaks at larger t_0' is evident not only in the combined spectra (Figure 4.3), but also in the individual rephasing and non-rephasing components of the spectra. The dotted, black lines indicate cut-offs where the contour step size has been increased, for clarity.

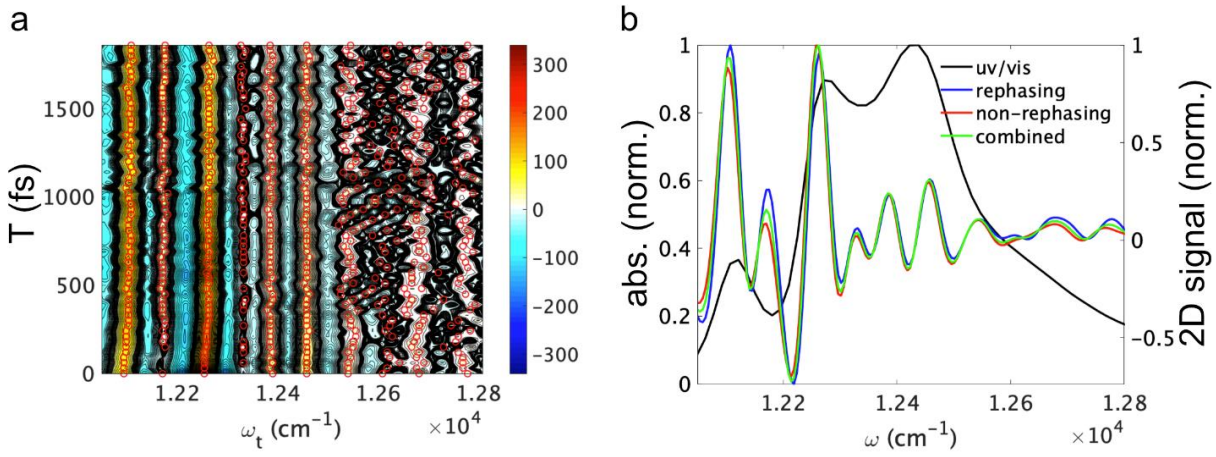

Figure 4.5. (a) The spectra are plotted after summation of the ω_τ axis, as a function of T. The red circles in each row indicate the peak positions located by the findpeaks algorithm in MATLAB. The average peak wavenumbers, and their standard deviations, are tabulated in Table 4.1 (b) The measured linear absorption spectrum (black) at 77 K is plotted along with the rephasing (blue), non-rephasing (red) and combined (green) measured 2D spectra after summation over ω_τ and T. The peak positions in the rephasing and non-rephasing spectra match, as theoretically expected, indicating that the filter acts consistently on signals generated from both sets of Liouville paths.

Several of the peak assignments made here coincide with those made by previous studies (Table 1). The second peak at 12167 cm^{-1} is likely due to the second-lowest (n=1) vibrational mode of exciton 1, or a vibronic alternative. Because of the presence of this peak, which ostensibly partially overlaps with the n=0 exciton 1 signal in the UV/vis spectrum, we find an exciton 1 energy assignment of 12101 cm^{-1} that is about 10 cm^{-1} redder than the closest previous assignment made by Vulto et. al. For exciton 2, the value of 12261 cm-1 is exactly the same as that by Vulto et. al. The assignments for excitons 3 and 4 are within the range of those from previous studies. Exciton 5 is 42 cm^{-1} blue of the closest assignment by Schmidt am Busch et al., perhaps explained the its standard deviation of 35 cm^{-1}.

The assignment ranges are especially large at 149, 129, and 168 cm^{-1} for excitons 6-8, respectively. The disparity is likely explained by the low intensity of these peaks compared to the others, which makes it so that samples dilute enough to reduce signal reabsorption in the most intense peaks render these less intense peaks too weak to observe easily. Here, the primary interest is to measure the positions of the smaller-intensity peaks with the largest diversity of assignments, especially that for exciton 8. To obtain signal from this low-intensity region of the spectrum, it was necessary to use an increased sample concentration (Fig. S1 in the SI). Therefore, we note that the OD in the window of 12,300 – 12,500 cm^{-1}, the region with the highest extinction coefficients, was in the range of 0.3-0.4, instead of the recommended range of <0.3. This increase can lead to some signal reabsorption and reduce their peak intensities within the nonlinear spectra. By the same token, because these peaks are so prominent, the reduced intensity does not harm the ability to determine their peak positions. Furthermore, as discussed previously, the values obtained for peaks within this wavenumber range are consistent with previous assignments (Table 4.1), corroborating their

assignments here. Meanwhile, at this concentration, exciton 8's OD was ~0.05, which is near the detection limit for our spectrometer. As a result, the signal is weaker at the bluer wavenumbers, as seen in Figure 4.5a.

Two more issues add to the difficulty of obtaining these eigenenergies. First, the spectral overlap of these last three peaks with each other produces a featureless, smooth decline in the linear absorption spectrum from approximately 12550 – 12800 cm^{-1}, rather than the peak structures more evident from 12000 to 12550 cm^{-1}, which makes it more difficult to identify their peak positions (Figure 4.5b). Second, exciton 8 has fewer assignments than the other excitons, because it was first reported in 2009 (14).

At 12596 cm^{-1}, our exciton 6 assignment supports the bluer side of the range from previous assignments. Meanwhile, our assignment of 12627 cm^{-1} for exciton 7 is in the middle of the range of previous assignments, very similar to the value of 12622 cm^{-1} assigned by Cho et. al. The assignment of exciton 8 to 12712 cm^{-1} exactly matches that proposed earlier by Schmidt am Busch et al (15). Though our exciton 8 assignment has a standard deviation of 48 cm^{-1} due to the weak intensity of the peak, this value is still smaller than the range of assignments, and our result supports the blue edge of the distribution from previous assignments.

	Hamiltonian								
Exciton	Vulto, 1998 (39)	Cho, 2005 (9)	Adoplh, 2006 (10)	Hayes, 2011 (12)	Schmidt am Busch, 2011 (15)	Kell, 2016 (17)	Olbrich 2016 (13)	Thyrhaug 2016 (40)	This work
1	12112	12116	12181	12121	12171	12128	12001	12121	12102±5
2	12261	12275	12284	12274	12342	12275	12044	12275	12261±6
3	12355	12363	12358	12350	12361	12350	12079	12348	12337±4
4	12414	12405	12454	12415	12458	12391	12147	12415	12425±19
5	12448	12422	12479	12454	12501	12434	12221	12487	12543±35
6	12610	12592	12584	12520	12560	12461	12250	12581	12596±16
7	12650	12622	12679	12606	12674	12556	12291	12685	12627±8
8	-	-	-	-	12712	12615	12544	12650	12712±43

Table 4.1. Exciton energies of previously published Hamiltonians are listed, as well as the one proposed here. All numbers are listed in units of wavenumbers (cm^{-1}), and the standard deviations of this work are reported, as obtained from multi-Gaussian spectral fits shown in Fig. 4.5a. The work by Adolphs & Renger assigned four sets of coupling constants in the site basis, using different electrostatic models. We listed the set obtained using the MEAD program. The results from the other models are available in reference 10. The numbers obtained from Olbrich et al. include a 42 meV offset referenced in that work (13). Where available, monomer Hamiltonians were used rather than trimer ones, and eight-site Hamiltonians were used rather than seven-site ones.

4.5. Conclusion

Weak one-quantum coherence signals were observed in FMO's 2D electronic spectra that persist at 1 ps delay. This component allows Lorentz-Gauss filtering methods (27) to be used, reducing the broadest contributions to the peak widths in the corresponding frequency-domain spectra, and therefore producing more narrow spectral features. We establish that the filtering method works correctly on these signal components in spectra calculated using HEOM. Finally, we obtain the peak positions from the narrowed 2D spectral peak structure.

References

(1) R.E. Fenna, B.W. Matthews. Chlorophyll arrangement in bacteriochlorophyll protein from Chlorobium limicola. Nature, 258:573-577, 1975

(2) S. Savikhin, D.R. Buck, et al. Toward level-to-level energy transfers in photosynthesis: the Fenna-Matthews-Olson Protein. JPCB, 102(29):5556-5565, 1998

(3) G.S. Engel, T.R. Calhoun, et al. Evidence for wavelike energy transfer through quantum coherence in photosynthetic systems. Nature, 446(7137):782-786, 2007

(4) J. Cao., R.J. Cogdell, et al. Quantum biology revisited. Sci. Adv., 6:1-12, 2020

(5) R.M. Pearlstein. Theiry of the optical spectra of the vacterichlorophyll a antenna protein trimer from Prosthecochloris aestuarii. Photosynth. Res., 31:213-226, 1992

(6) D. Gulen. Interpretation of the excited state structure of the Fenna-Matthews-Olson pigment protein complex of Prosthecochloris aestuarii based on the simultaneous comulaton of the 4K absorption, linear dichroism and singlet-triplet absorption difference spectra: a possible excitonic explanation? JPC, 100:17683-17689, 1996

(7) R.J.W. Louwe, J. Vrieze, et al. Toward an integral interpretation of the optical steady-state spectra of the FMO-complex of Prosthecochloris aestuarii. 2. Exciton simulations. JPC, 101:11280-11287, 1997

(8) S.I.E. Vulto, M.A. de Baat, et al. Excited state dynamics in FMO antenna complexes from photosynthetic green sulfur bacteria: a kinetic model. JPCB, 103(38):8153-8161, 1999

(9) M. Cho, H.M. Vaswani, et al. Exciton analysis in 2D electronic spectroscopy. JPCB, 109(21):10542-10556, 2005

(10) J. Adolphs, T. Regner. How proteins trigger excitation energy transfer in the FMO complex of green sulfur bacteria. Biophys. J., 91(8):2778-2797, 2006

(11) F. Muh, M.E.A. Madjet, et al. Alpha-helices direct excitation energy flow in the FMO protein. PNAS, 104:16862-16867, 2007

(12) D. Hayes, G.S. Engel. Extracting the excitonic Hamiltonian of the Fenna-Matthews-Olson complex using three-dimensional third-order electronic spectroscopy. Biophys. J., 100(8):2043-2052, 2011

(13) C. Olbrich, T.L.C. Jansen, et al. From atomistic modeling to excitation transfer and two-dimensional spectra of the FMO light-harvesting complex. JPCB, 115(26):8609-8621, 2011

(14) D.E. Tronrud, J. Wen, et al. The structural basis for the difference in absorbance spectra for the FMO antenna protein from various green sulfur bacteria. Photosynth. Res., 100(2):79-87, 2009

(15) M. Schmidt am Busch, F. Muh, et al. The eight bacteriochlorophyll completes the excitation energy funnel in the FMO protein. JPCL, 2(2):93-98, 2011

(16) S.H. Yeh, S. Kais. Simulated two-dimensional electronic spectroscopy of the eight-bacteriochlorophyll FMO complex. JCP, 141(23):234105, 2014

(17) A. Kell, R.E. Blankenship, et al. Effect of spectral density shapes on the excitonic structure and dynamics of the Fenna-Matthews-Olson trimer from Chlorobaculum tepidum. JPCA, 120(31):6146-6154, 2016

(18) R.G. Saer, V. Stadnytskiy, et al. Probing the excitonic landscape of the Chlorobaculum tepidum Fenna-Matthews-Olson (FMO) complex: a mutagenesis approach. Biochim. Biophys. Acta, Bioenerg., 1858)4):288-296, 2017

(19) M.L. Flanagan, P.D. Long, et al. Mutations to R. sphaeroides reaction center perturb energy levels and vibronic coupling but not observed energy transfer rates. JPCA, 120(9): 1479-1487, 2016

(20) M.T.W. Milder, B. Bruggemann, et al. Revisiting the optical properties of the FMO protein. Photosynth. Res., 104(2-3):257-274, 2010

(21) G.D. Scholes, G.R. Fleming, et al. Using coherence to enhance function in chemical and biophysical systems. Naturem 543(7647):647-656, 2017

(22) S. Mukamel. Principles of nonlinear optical spectroscopy. Oxford University Press: New York, 1995

(23) H. Zheng, J.R. Caram, et al. Dispersion-free continuum two-dimensional electronic spectrometer, Appl. Opt., 53(9):1909-1917, 2014

(24) G. Panitchayangkoon, D. Hayes, et al. Long-lived quantum coherence in photosynthetic complexes at physiological temperature. PNAS, 107(29):12766-12770, 2010

(25) E.A. Arsenault, Y. Yoneda, et al. Vibronic mixing enables ultrafast energy flow in light-harvesting complex II. Nature Communications, 1-8, 2020

(26) V. Butkus, L. Valkunas, et al. Vibronic phenomena and exciton-vibrational interference in two-dimensional spectra of molecular aggregates. JCP, 140(3):034306, 2014

(27) A.G. Ferrige, J.C. Lindon. Resolution enhancement in FT NMR through the use of a double exponential function. J. Magn. Reson., 31:337-340, 1978

(28) Y. Tanimura, R. Kubo. Time evolution of a quantum system in contact with a nearly Gaussian-Markoffian noise bath. J. Phys. Soc. Jpn., 58:101-114, 1989

(29) A. Lohner, K. Ashraf, et al. Fluoreschence-excitation and emission spectroscopy on single FMO complexes. Sci. Rep., 1-7. 2016

(30) T. Brixner, T.S. Mancal, et al. Phase-stabilized two-dimensional electronic spectroscopy. JCP, 121(9):4221-4236, 2004

(31) A. Ishizaki, G.R. Fleming. Unified treatment of quantum coherent and incoherent hopping dyanmics in electronic energy transfer: reduced hierarchy equation approach. JCP, 130(23):234111, 2009

(32) Q. Shi, L. Chen, et al. Efficient hierarchical Liouville space propagator to quantum dissipative dynamics. JCP, 130(8):084105-5, 2009

(33) P. Hamm, M. Zanni. Concepts and methods of 2D infrared spectroscopy; Cambridge University Press, Cambridge, 2011

(34) J. Albert, A. Schubert, et al. Two-dimensional vibronic spectroscopy of molecular predissociation. New J. Phys., 15:025008, 2013

(35) M. Kess, V. Engel. Two-dimensional femtosecond optical spectroscopy of trapping dynamics in a charge-transfer process. Chem. Phys. Lett., 650:41-46, 2016

(36) C. Kreisbeck, T. Kramer, et al. Disentangling electronic and vibronic coherences in two-dimensional echo spectra. JPCB, 117(32):9380-9385, 2013

(37) B.S. Rolczynski, H. Zheng, et al. Correlated protein environments dribe quantum coherence lifetimes in photosynthetic pigment-protein complexes. Chem, 4(1):138-149, 2018

(38) J. Strumpfer, K. Schulten. The effect of correlated bath fluctuations on exciton transfer. JCP, 134(9):095102-095109, 2011

(39) S.I.E. Vulto, M.A. de Baat, et al. Exciton simulations of optical spectra of the FMO complex from the green sulfur bacterium Chlorobium tepidum at 6K. JPCB, 102(47):9577-9582, 1998

(40) E. Thyrhaug, K. Zidek, et al. Exciton structure and energy transfer in the Fenna-Matthews-Olson complex. JPCL, 7(9):1653-1660, 2016

CHAPTER 5

SPECTROSCOPIC STUDIES OF INTERACTION OF ORBITAL ANGULAR MOMENTUM OF LIGHT WITH MATTER

5.1. Overview

When electromagnetic field of light interacts with the sample, we observe various processes associated with the absorption of the energy or emission from the excited states. We collectively call these observables "macroscopic polarization". Light carrying linear and/or spin angular momentum excites the charges in the system to an excited state governed strictly by the selection rules allowed for such transitions. Usually, these transitions are so-called electrically dipolar, rarely (and less detectable) quadrupolar. With the discovery of orbital angular momentum of light in 1992 by Allen and coworkers, a new field of studies has emerged where light-matter interactions with different (from conventional) selection rules are of high interest. This new degree of freedom – orbital angular momentum of light – has opened up the opportunities for a wide variety of applications from imaging to astrophysics. However, due to the challenging nature of capturing the interactions and transfer of OAM to the material, spectroscopic aspect of this field has not been widely explored. In this work we attempt to shed light on how twisted light interacts with bulk semiconductors with the future applications for information detection and sensing.

5.2. Functions of angular momentum of light: spin and orbital angular momenta

Imagine a lone electron in a hydrogen atom. It is moving around the atom's nucleus at a certain distance away from the nucleus bound by Coulombic forces with the latter (1). In quantum mechanics one can characterize that electron with four quantum numbers:

- Principal quantum number n that describes the energy of the electron in the electronic shell. It can take values of 1 to potentially infinity;
- Angular momentum quantum number *l* that emphasizes the subshell of the electron's location on the orbit. The values range between 0 and n – 1, and can only be integers.
- Magnetic quantum number m_l showing the projection of orbital angular momentum *l* on a particular axis. Electron can have m_l between $-l$ and $+l$
- Spin quantum number ms that explains the spin orientation of the electron with respect to the other electrons in the same shell or subshell. The electron can only have two values of m_s, and those are +1/2 or –1/2

These quantum numbers can also be described in the electron's wavefunction. The values that n, *l*, m_l and m_s take are directed by the fact that electrons are fermions, and follow Fermi-Dirac statistics.

Light, however, is different. Photons are also described as bosons, following Bose-Einstein statistics (2 – 4). They form a transverse electromagnetic wave that can be classically described with electric and magnetic fields that are orthogonal to each other. From here and on we will express light as an electric field, since the magnetic field component of the electromagnetic wave is smaller than the electric field component by a factor of speed of light. Light travels in a seemingly straight line (with some deviations as the beam path approaches the Rayleigh length in a laser pulse) (5). However, while maintaining the straight-line path, electric field of light can rotate or spin around the axis of beam propagation. This is where the electrons and the photons are similar. The invisible to our eye rotation and spinning of the electromagnetic field is caused by the

orbital (L) and spin (S) angular momenta of light respectively (6). These two quantities add to quantify the total angular momentum of light T.

In contrast to electronic angular momenta, the photon's spin can take values of $+\hbar$ or $-\hbar$. We normally call light with spin angular momentum (SAM) circularly-polarized light, where the sign of the value determines the direction of the polarization of light in the paraxial beams. This means that the direction of SAM vector is aligned with direction of beam propagation, or its wavevector k. In other words, the intrinsic spin angular momentum of light is longitudinal (2, 7). If we assign the direction of beam propagation as vector z, the electric field of circularly polarized light is broken down into two orthogonal components with unit vectors of x and y. The phase shift between the individual electric field components E_x and E_y is 90 degrees, or a quarter wavelength (Fig. 5.1). If the magnitudes of the components are identical, this is the case of circularly polarized light. Otherwise, the beam has elliptical polarization.

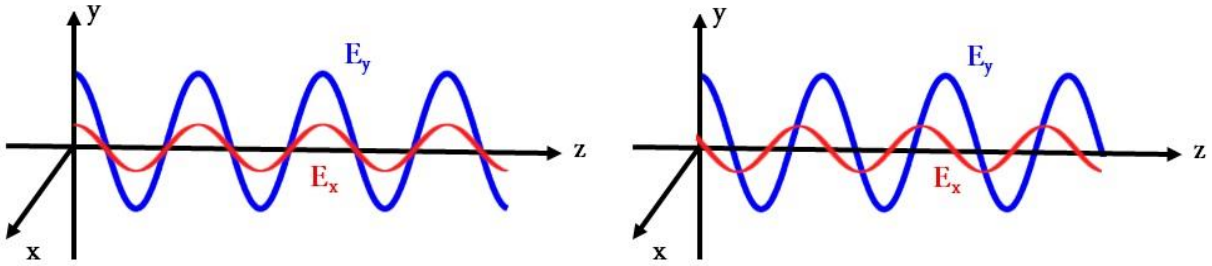

Figure 5.1. (Left) Orthogonal x and y components of the electric field in the direction of beam propagation z. There is no phase shift between the components. (Right) The x and y components of electric field are shifted by a quarterwave forming circularly-polarized light.

Physically, we can describe the electromagnetic wave with the following general electric field equation 1:

$$\vec{E} = E_x\hat{x}\cos(kz - wt) + E_y\hat{y}\cos(kz - wt + \varphi) \quad (1)$$

Generally, in linearly polarized light the phase shift φ = 0°, while in circularly polarized light φ = 90°. This relationship proves that linearly polarized light can be described as a linear combination of right and left circularly polarized light waves.

The direction of polarization of light can be changed universally by reflecting the beam off a reflective surface. Hence, horizontally polarized light can be reflected to form vertically polarized light, and vice versa. The same principle works for the circularly polarized light, where right circularly polarized light can be transformed into left circularly polarized light via reflection. The same effect can be achieved with a birefringent half waveplate – an optical element that introduces a phase shift of a half wave, or 180°. Similarly, linearly polarized light can be converted into circularly polarized light (and vice versa) using a quarter waveplate – a waveplate with the phase shift of 90° (8). Finally, it is important to note that both linearly- and circularly-polarized lights carry energy in planar areas of constant phase, called wavefronts.

Electromagnetic field can also carry orbital angular momentum. It does not describe polarization of light, but the spatial distribution of the electric field. In other words, the wavefront of light carrying orbital angular momentum is not planar, but rather helical. We call this light “twisted light” and “light with OAM” interchangeably (9). Because the spin and orbital angular momenta are fundamentally different properties of light, they can coexist in the electromagnetic field. Thus,

one can generate linearly- or circularly-polarized twisted light. The rest of this chapter will focus on properties of orbital angular momentum of light and its interaction with matter.

5.3. Orbital angular momentum of light: Potential and applications

In the age of ever-increasing demand to provide reliable means of data consumption and transfer, the pressure is growing to discover new ways to store and transfer information safely. Angular momentum of light adds a new degree of freedom to classical and quantum communications (10). Spin angular momentum, or polarization, is already used in optical technologies to encode information into light. However, due to limitations of the amount of spin being imparted into photons, the technology is limited. Using orbital angular momentum of light provides potentially infinite amount of angular momentum quanta and adds an opportunity to encode more information and transfer it to the recipient securely. Free-space and optical fiber propagation of light carrying OAM has been shown to date. It has been possible to multiplex 16 OAM values in free space with spectral efficiency comparable to multiplexing with SAM. In an optical fiber, the speed of 1.6 Tbit/s was reached with multiplexing two values of OAM over 10 wavelengths, and 400 Gbit/s with two OAM modes over one wavelength value (11, 12). Underwater communications are currently being actively explored as well. However, turbulent environments such as underwater currents, affect the OAM state purity due to its heavy dependence on the phase stability, adding complexity to developing communication technology using twisted light (13).

Orbital angular momentum of light found another major use in optical tweezers. In optical tweezers, a laser beam that is focused very tightly traps the sample of interest for further microscopic analysis. Arthur Ashkin and coauthors were the first to report an interesting discovery where the focused beam of light could trap and hold a microscopic particle stably (14). The main principle behind the technology lies in the gradient of the electric field at the beam waist that attracts dielectric particles and traps them. Adding OAM to the focused laser beam allows for the angular momentum transfer forcing the trapped particle to rotate according to the amount of OAM supplied (15, 16). This allows for imaging the dielectric particle from different sides, providing a more accurate image of the surface.

Finally, imaging in micro- and macroworld is another important application of the twisted light. Astronomers use optical vortex coronograph that allows to find dim objects near a bright object in the cosmos (17, 18). The telescope with the spiral phase plate is centered on the bright spot – this turns the circular bright spot into a weaker donut shaped image. The contrast between the now-not-so-bright spot and the dim spot is not as stark allowing for looking at the properties of the dim spot in the telescope. On the other end of the size scale, twisted light is used in super-resolution stimulated emission depletion (STED) microscopy – an imaging method with enhanced resolution compared to conventional confocal microscope (19, 20). Here, the conventional beam is focused to a diffraction-limited spot on the sample of interest and is followed by the donut-shaped STED pulse. This STED pulse suppresses fluorescence from the unnecessary molecules and enhances the signal from the compound of interest, improving the resolution of the image of the desired spot. Additionally, technology is in development to use twisted light for imaging with X-rays and electron microscope.

Exceptional purity of the twisted light mode is needed for all precise measurements mentioned above. Improvements need to be implemented to ensure the purity and stability of the phase of the twisted beam; however, the techniques involving twisted light have a lot of promise, which is why it is important to understand the interactions of OAM with matter, and the transfer of that momentum to the electronic states.

5.4. Physical interpretation of orbital angular momentum of light

Solutions to Maxwell's equations in free space with no charges or current result in electromagnetic wave equation (3, 4). One can separate the electric field and magnetic field terms to obtain wave equation for each field individually (Eq. 2 and 3):

$$\nabla^2 E = \frac{1}{c^2}\frac{\partial^2 E}{\partial t^2} \tag{2}$$

$$\nabla^2 B = \frac{1}{c^2}\frac{\partial^2 B}{\partial t^2} \tag{3}$$

Here, E and B represent electric and magnetic fields respectively, and c is the speed of light in vacuum. We will omit the magnetic wave equation for the purposes of this work, but the following derivations can equally apply to it.

Additionally, we consider paraxial approximation, or a small angle approximation, where the angle between the wave vector k and the axis of beam propagation z is negligibly small (Eq. 4):

$$\left|\frac{\partial^2 E}{\partial z^2}\right| \ll \left|k\frac{\partial E}{\partial z}\right| \tag{4}$$

When combined, the resulting electric field can be represented as the following (Eq. 5):

$$\vec{E}(\vec{r},t) = \vec{e}(\vec{r},t)u(\vec{r})e^{i(kz-\omega t)} \tag{5}$$

Here, the field amplitude u and the polarization of light can be controlled separately. The term $\vec{e}(\vec{r},t)$ can include SAM and OAM components of light.

The next step is to introduce Gaussian profile into electric field equation. The Gaussian electric field in the paraxial approximation is the following (Eq. 6):

$$E(r,z) = E_0\left(\frac{\omega_0}{\omega(z)}\right)\exp\left[-ik\frac{r^2}{2R(z)}\right]\exp\left[-\frac{r^2}{\omega^2(z)}\right]\exp[-i\psi z] \tag{6}$$

Here ω_0 is the beam waist at the focal point, $\omega(z)$ is the beam waist and R(z) is the radius of curvature at position z along the axis of beam propagation. $\psi(z)$ is the Gouy phase that is defined with Eq. 7:

$$\psi(z) = \arctan\left(\frac{z}{z_R}\right) \tag{7}$$

One can consider the different coordinate systems to describe the Gaussian beam profile. For instance, the solutions to Helmholtz wave equation with paraxial approximation in Cartesian coordinates result in Hermite-Gaussian modes (21, 22), with the description of the beam propagation along x, y, and z axis. The field amplitude u is described as Eq. 8:

$$u_{m,n}^{HG}(x,y,z) = C_{m,n}^{HG}\left(\frac{1}{\omega(z)}\right)\exp\left[-ik\frac{x^2+y^2}{2R(z)}\right]\exp\left[-\frac{x^2+y^2}{\omega^2(z)}\right]\exp[-i(m+n+1)*$$

$$\psi(z)]\,H_m\left(\frac{x\sqrt{2}}{\omega(z)}\right)H_n\left(\frac{y\sqrt{2}}{\omega(z)}\right) \tag{8}$$

where $C_{m,n}^{HG} = \sqrt{\frac{2}{\pi n!m!}}2^{-(m+n)/2}$ and $H_m(a) = (-1)^m e^{u^2}\frac{d^m}{du^m}(e^{-a^2})$

Alternatively, Laguerre-Gaussian mode is the solution to Helmholtz wave equation with paraxial approximation in cylindrical coordinates with the following mathematical description in Eq. 9 (21 – 23):

$$u_{l,p}^{LG}(r,\phi,z) = C_{l,p}^{LG}\left(\frac{1}{\omega(z)}\right)\exp\left[-ik\frac{r^2}{2R(z)}\right]\exp\left[-\frac{r^2}{\omega^2(z)}\right]\exp[-i(|l|+2p+1)*$$

$$\psi(z)]\,L_p^{|l|}\left(\frac{2r^2}{\omega^2(z)}\right)\exp[-il\phi]\,[\frac{r\sqrt{2}}{\omega(z)}]^{|l|} \quad (9)$$

where $C_{l,p}^{LG} = \sqrt{\frac{2p!}{\pi(|l|+p)!}}(-1)^p$ and $L_p^{|l|}(a) = x^{p+l}e^{-a}\frac{d^p}{da^p}\frac{a^{-l}e^a}{n!}$

It is worth noting that $u_{0,0}^{HG}$ and $u_{0,0}^{LG}$ represent the same Gaussian mode, and the laser output that we use for spectroscopic experiments is typically HG_{00}.

Physical picture of the equations described above results in Laguerre-Gaussian, or twisted beams where *l* describes the amount of OAM, and p is the number of radial nodes. For the purposes of this work we will keep p=0. However, it would be an interesting problem to investigate the spectral changes in the samples as a function of p.

The resulting LG_l modes are characterized with the maximum intensity of the beam towards the edges of the profile, with singularity in the center of the beam. The wavefront in twisted beams is helical, where the azimuthal component of the wavevector is resembling a spiral, with single spiral-like rotation from 0 to 2π (Fig 5.2). Similarly, for OAM = 5, the phase changes five times in the interval from 0 to 2π. The higher the value of OAM, the faster the light moves around its own axis. As a result, the Poynting vector, or the vector of energy motion, is orthogonal to E and B, and points in the same direction as the wavevector.

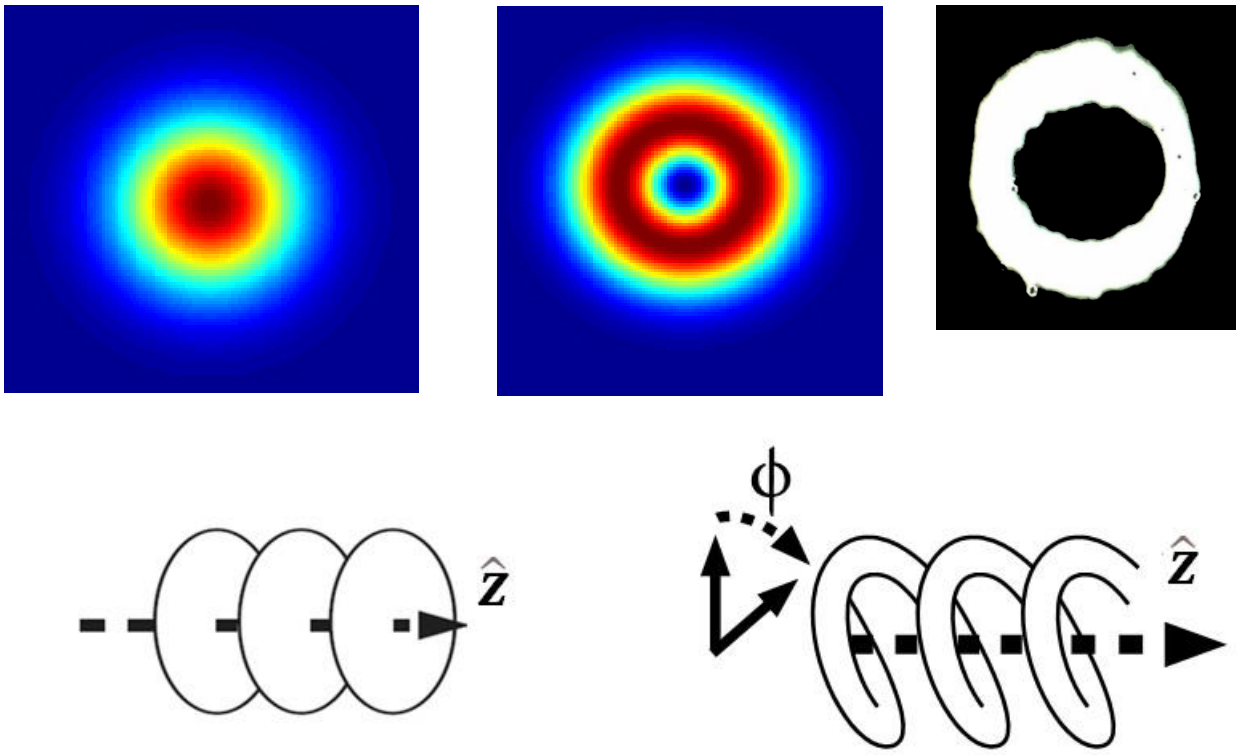

Figure 5.2. (Top left) Intensity profile of light with no orbital angular momentum. (Top middle) Intensity profile for light with OAM = 1; this beam contains a phase singularity in the middle with intensity increasing circularly towards the edges of the beam. (Top right) Image of light with OAM = 5 collected on a camera in the laboratory. (Bottom left) Planar wavefront of light with no OAM in the direction of beam propagation z. (Bottom right) Helical wavefront of light with OAM defined by Gouy phase φ

Finally, when considering individual photons, they will carry OAM of $l\hbar$, similar to circularly polarized light with $\sigma\hbar$ quanta of angular momentum.

We will further consider the interaction of light carrying OAM and SAM with matter, and the experimental implications of such a challenge.

5.5. Generating orbital angular momentum of light

Generation of arbitrary amount of angular momentum in the electromagnetic field is a complicated matter, as imperfections in optical elements that are used to introduce OAM to beams cause defects in the beam shape. These defects interfere with the high-quality information transfer that was described previously, and the spectroscopic measurements that are described later in this chapter. There are multiple ways of introducing "twist" into the light, all of which rely on changing the phase relationship within the components of the electric field. While none of the methods are ideal, there is the most advantageous way of generating twisted light. Multiple methods will be discussed below.

Spiral phase plate

A spiral phase plate, or a vortex lens, is a plate of varying thickness made of glass or plastic (Fig. 5.3). The disk with a certain refractive index has a helical shaped surface, where thickness varies as a function of ϕ, the angle complimentary to the OAM value in the electric field equation (24 – 26). The amount of orbital angular momentum imparted into the beam with an SPP is calculated via the following equation 10:

$$l = \frac{h_s(n-n_0)}{\lambda} \tag{10}$$

Here, n and n_0 are indices of refraction of material of the plate, and the surrounding medium respectively, h_s is the step height and λ is the wavelength of light.

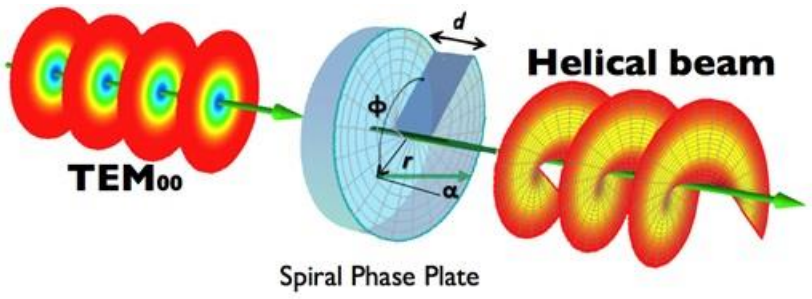

Figure 5.3. Generation of twisted light using spiral phase plate. The dimensions of the plate are defined with thickness of the spiral d, and the angle ϕ. Figure adapted from (51) within conditions set by Creative Commons License CC BY-SA 3.0

One of the limitations of the SPP is that it is wavelength specific since index of refraction in the medium is wavelength-dependent. Additionally, in order to obtain relatively small values of OAM through an SPP, the step height should be on the order of hundreds of nanometers, which requires precise manufacturing of the plate. In order to avoid manufacturing multiple spiral phase plates to achieve multiple values of OAM, and replacing the optical elements compromising the optical setup alignment, a wedged plate from the same material is used to alter the thickness of the plate. With the development of high-precision 3D printing it has become possible to easily create spiral phase plates of varied thickness and azimuthal angle and manipulate the light more efficiently.

Q-plate

A q-plate operates on the principle of coupling the spin orbital angular momentum of light with its orbital angular momentum (Fig. 5.4) (27, 28). A film of liquid crystals that have tunable orientation is placed between glass slides. The electronically controlled liquid crystals are capable of shaping a pattern that will convert circularly polarized light into twisted light. That pattern is unique to the

amount of orbital angular momentum one wishes to obtain. The handedness of circularly polarized light defines the helical direction in twisted light.

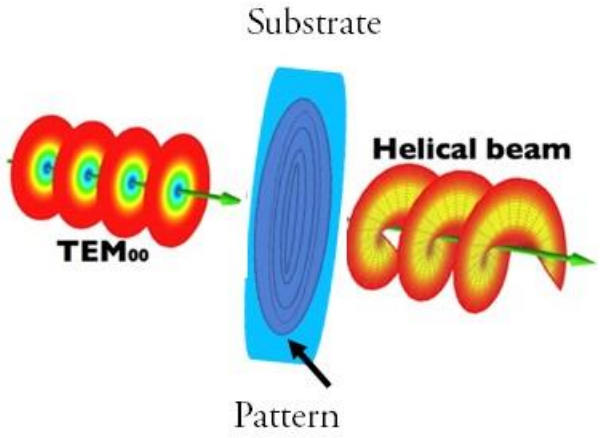

Figure 5.4. Generation of twisted light with q-plate – a glass substrate plate with a pattern imprinted on it that converts circularly-polarized light into light with helical wavefront.

There are multiple advantages to using q-plate to generate twisted light. The main one is that it is a very thin optical element, thus preventing from generating to much spectral dispersion upon transmission for pulses. Another advantage comes from the fact that the materials typically used for a q-plate are highly transmissive and efficient with barely any light deflection in the outcoming beam. However, a strong disadvantage against using q-plate in the laboratory setting is that the input beam should contain spin angular momentum. Generating very precise circularly-polarized light is not impossible, but is very challenging. Any distortion in the quality of CP light will lead to distorted twisted beam.

Cylindrical lens mode converter

Another way to generate orbital angular momentum in light is by using cylindrical mode converters. Essentially, this method relies on sending a Hermite-Gaussian mode at 45 through two cylindrical lenses (29). The HG mode is diagonally aligned with respect to the lenses, so it can be decomposed into its horizontal and vertical components (Fig. 5.5). The cylindrical lenses introduce Gouy phase shift between these components that result in a Laguerre-Gaussian mode of certain helicity. While this is a very efficient way of making twisted light, its main limitation is that a certain HG mode should be used to generate the desired LG mode.

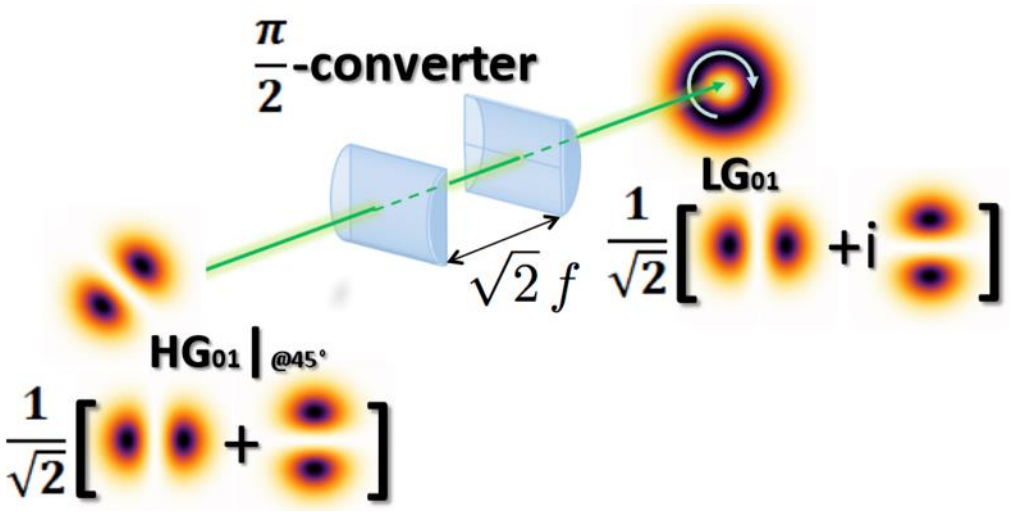

Figure 5.5. Generation of twisted light using cylindrical lens mode converter. The pair of lenses introduce a Gouy phase into x and y components of Hermit-Gaussian modes emitted from the laser. Figure adapted from (52) within conditions set by Creative Commons License CC BY-SA 3.0

For instance, if the goal is to generate the twisted beam with l = 3, one should use HG mode with m = 3, and n = 0. Generating complicated Hermite-Gaussian modes is a challenging task as specific mode converters are needed to go from conventional HG_{00} mode to non-zero modes.

Computer-generated holograms

Arguably, the most efficient way of generating twisted light is by using computer generated holograms that can be applied to the spatial light modulator (SLM). An SLM is a grid of liquid crystals, where each crystal is controlled by voltage applied to it to take a programmed orientation. SLMs can control the phase and the amplitude of the beams passing through or reflected of its surface (Fig. 5.6). A forked diffraction grating is applied to the SLM (30, 31). The forked diffraction grating is calculated from the interference pattern of the incoming beam with OAM = 0, and the beam with desired OAM.

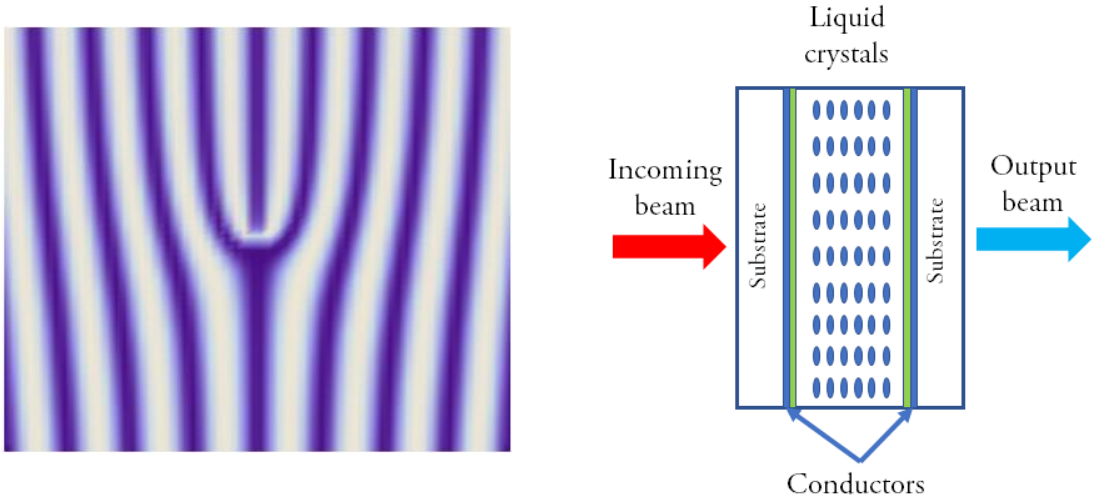

Figure 5.6. (Left) The "fork" diagram encoded into a spatial light modulator, calculated from Eq.14. (Right) Structure of the spatial light modulator to control phase of the beam. This figure shows transmissive SLM, however, reflective SLMs are commonly used as well.

First, we need to express the electric fields of the two beams with their respective phase components (Eq. 11):

$$E_{HG} = E_{HG}^{0} * \exp\left(i(\omega t + kx)\right) \text{ and } E_{LG} = E_{LG}^{0} * \exp\left(i(\omega t + l\phi)\right) \quad (11)$$

Then the intensity is proportional to E_{total}^2, where E_{total} is the sum of E_{HG} and E_{LG} (Eq. 12):

$$I \propto E_{total}E_{total}^* \tag{12}$$

From here follows Eq. 13,

$$E_{total}E_{total}^* = |E_{HG}|^2 + |E_{LG}|^2 + E_{HG}^*E_{LG} + E_{HG}E_{LG}^* \tag{13}$$

Solving for the last two terms in the sum yields the interference pattern (Eq. 14):

$$E_{HG}^*E_{LG} + E_{HG}E_{LG}^* = 2\cos\left(l\phi - \frac{2\pi}{\Lambda}rcos\theta\right) \tag{14}$$

where Λ is the distance between the lines in the grating equation.

As this is a grating, multiple orders of Bragg diffraction are observed. The 0th order contains no OAM, while the 1st order on each side of the 0th corresponds to desired OAM with opposite helicities. We arbitrarily select a 1st order to have +OAM, while the other 1st order will carry –OAM. At OAM = 0, the pattern on the SLM will resemble a regular diffraction grating (Fig. 5.7).

It is important to identify the proper fork diagram parameters to increase the efficiency of twisted light output. The 0th order diffraction in any grating is the most efficient, with the efficiency dependent on the angle of the incoming beam, the distance between the lines in the grating and the amount of lines. Typically, the efficiently of the 0th order is 60-70% of total intensity of the incoming beam. That leaves us with 30% of power remaining for all other diffraction orders combined.

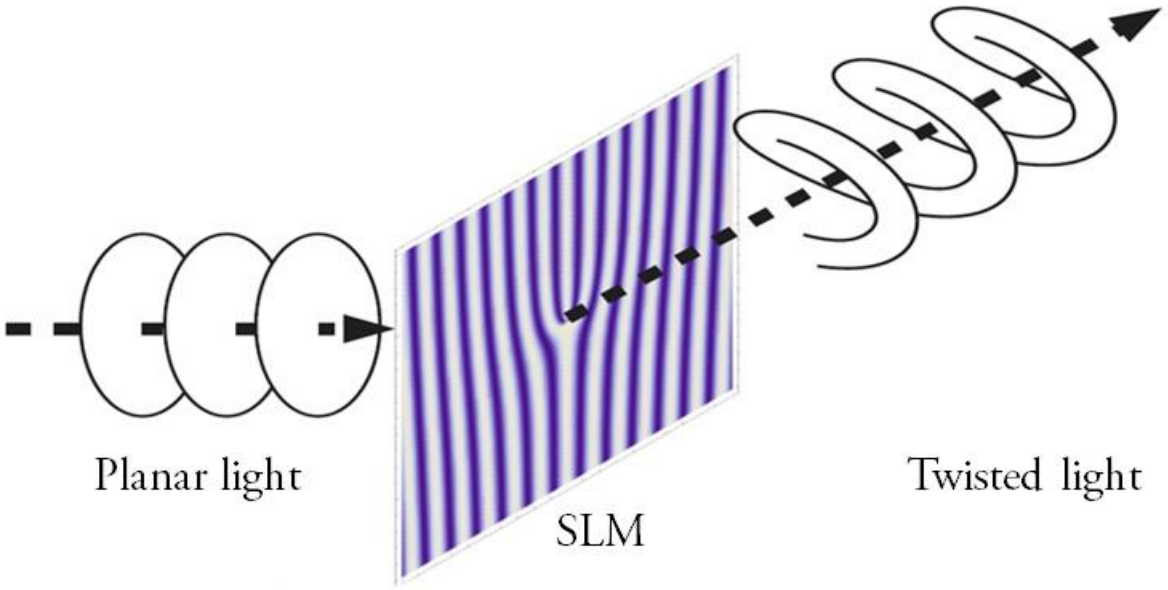

Figure 5.7. Conversion of plane-polarized light to twisted light using a spatial light modulator. The output beam is not normal to the plane of the SLM because we collect the first diffraction order for desired OAM.

The single first order intensity is about 12% of the intensity of the incoming beam which limits how much power is carried with the output beam. An additional concern is the damage threshold of the SLM. These considerations limit how much instantaneous power can be sent to the SLM surface and be output for the experimental purposes. However, the advantages of using SLMs for generating twisted light – easy control of OAM, large range of values – outweigh the disadvantages of the technique.

5.6. Twisted light transient absorption setup

We use transient absorption spectroscopy to perform the first measurements of the interaction of orbital angular momentum of light with matter. An ultrafast Ti:Sapphire oscillator (Micra,

Coherent) seeds an ultrafast regenerative amplifier (Coherent Legend Elite). The output is a 36 fs pulse with repetition rate of 5 kHz and average power of 2.7 W. The pulse compression is verified with FROG. The beam is directed to a 95/5 beamsplitter to split into pump and probe beams. The pump beam is converted into twisted light and focused through an iris Fourier filter. It is further retroreflected in the automatic delay stage to generate the delay between the pump and the probe pulses. The pump beam is then chopped at the repetition rate of 2.5 kHz. Simultaneously, probe is traveling without any special treatment. The pump and the probe are then focused at the sample. The probe beam is significantly weaker than the pump beam to avoid additional excitations by the beam with the energies of 0.1 nJ/probe and 5.4 nJ/pump. Upon interaction with the sample the probe beam that is colinear with the field emitted from the light-matter interaction is focused in the spectrometer, and further resolved on the linescan Teledyne Dalsa Spyder 3 CCD camera.

The pump undergoes special treatment to add the orbital angular momentum to the beam (Fig. 5.8). It is collimated and reflected off a spatial light modulator (SLM; Meadowlark) with the following mask (Eq. 15):

$$T(r,\phi) = T_0 exp\left[i\alpha\, cos\left(\ell\phi - \frac{2\pi r}{\Lambda} cos(\phi)\right)\right] \tag{15}$$

Initially, *l*, or OAM, is set to 0 generating a conventional diffraction grating pattern. The first order of diffraction is selected and incident on a spherical mirror two focal lengths away. Further, at a distance of another two focal lengths away is the SLM2 that has the phase mask of the desired value of orbital angular momentum to be imparted into the beam. This results in a "fork" diffraction grating pattern described in the previous section. A diffraction grating portion of the mask is necessary to be able to separate the twisted portion of the output. Again, the first order

carrying twist in the light is selected and focused on the iris that acts as a Fourier filter. This allows to "clean" the beam mode by filtering out the contributions from other diffraction orders.

The radius of the pump beam from its center changes as a function of orbital angular momentum according to the equation 16:

$$r(I_{max}) = \sqrt{\frac{|l|}{2}}w(z) \tag{16}$$

Here, *l* is the amount of orbital angular momentum of light, and w(z) is the beam waist of the original beam that is independent on OAM (32). This is calculated for Laguerre-Gaussian modes, where the intensity of the beam in the center is zero. So it is no surprise that when solved for *l* = 0, the radius becomes 0 as well. This is because the maximum intensity is exactly in the center of the beam. Because it is important for the pump and the probe beams to overlap at all times at the sample position, the probe beams need to have the size of the largest pump beam that is used for excitation. The beam waist for OAM = 0 was measured to be 4.7 μm, and for OAM = 10 measured as 12 μm. Inaccuracies in the beam size measurements are attributed to the insufficient sensitivity of the powermeter at very low powers of the pump beam supplied to the sample.

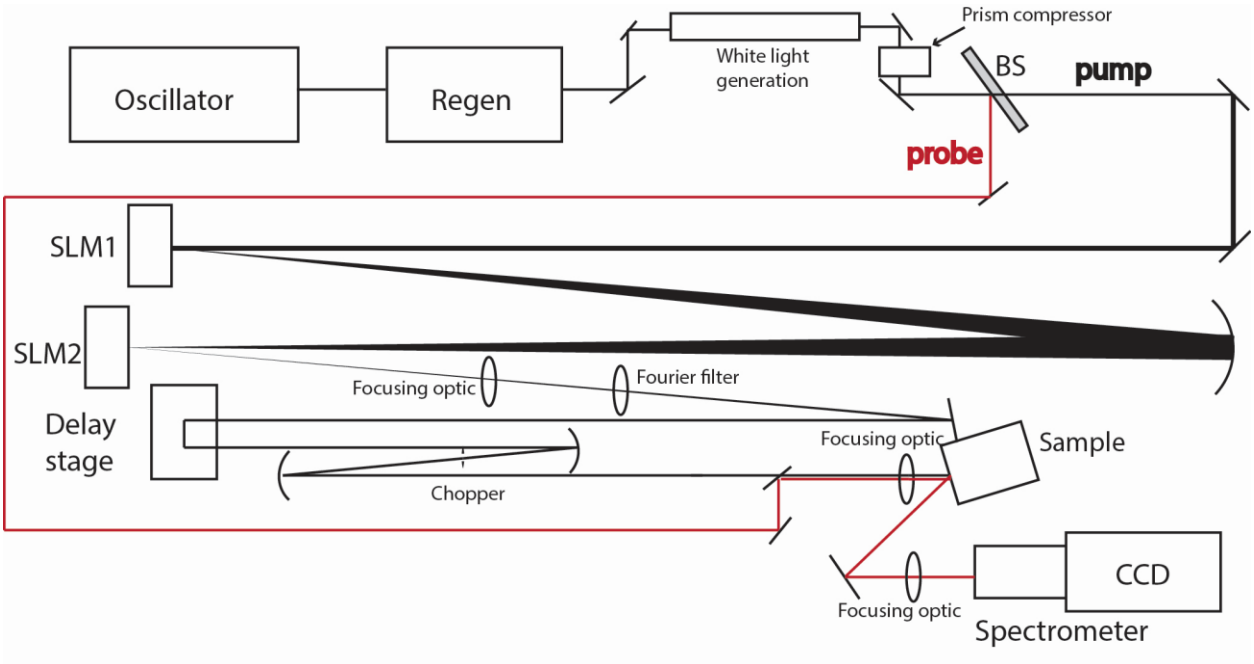

Figure 5.8. Twisted light transient absorption setup. The regenerative amplifier can be passed through argon tube for supercontinuum generation (not needed for bulk GaAs). The beam is then split with the beamsplitter into pump and probe. Pump undergoes conversion to twisted light, and Fourier filtering to eliminate unnecessary diffraction orders. It is further passed through a retroreflector on a delay stage to control the time delay between pump and probe, and is subsequently chopped. The probe beam undergoes no special treatment and propagates to the sample. Both beams are focused at the sample and the probe is sent to the spectrometer for spectral resolution, and to the CCD camera.

5.7. Bulk gallium arsenide: considerations in sample choice

As described in the previous section, the light intensity is the strongest away from the center of the twisted pump beam, and the radius of the beam increases with OAM. Therefore, certain considerations need to be taken into account when selecting a sample for the initial proof of concept experiment. A large delocalization of the exciton is needed to be able to observe the interaction of light with OAM and matter. Alternatively, systems with electrons traveling long distances can be used as well. This is governed by the spatial overlap of the light mode and the sample, and the transition probability from the ground state to a certain excited state, the latter being directed by Fermi's Golden Rule. A two- or three-dimensional lattice is needed to support delocalized free carriers.

Therefore, GaAs is chosen to be the sample for the first set of experiments. This material is a direct gap semiconductor with the bandgap of 1.51eV (816.2nm) at 5K and 870nm at room temperature when undoped (33) (Fig. 5.9). The <100> crystal is chosen due to comparison with previously obtained experimental data by Li, et al. for OAM = 0 (34, 35).

GaAs supports Wannier-Mott excitons, which exhibit large delocalization and relatively small exciton binding energy. The bulk GaAs wafer is purchased from MTI Corp. Three distinct wafers of GaAs are obtained: undoped, Si-doped with concentration of 3.80-6.20×101^{6} cm^{-3}, and Si-doped with concentration of 1.07-1.90×10^{18} cm^{-3}. Doping blue-shifts the absorption spectrum, and its effect can be studied on the light-matter interaction as well. All wafers are double-sided polished with light reflectivity of 30%.

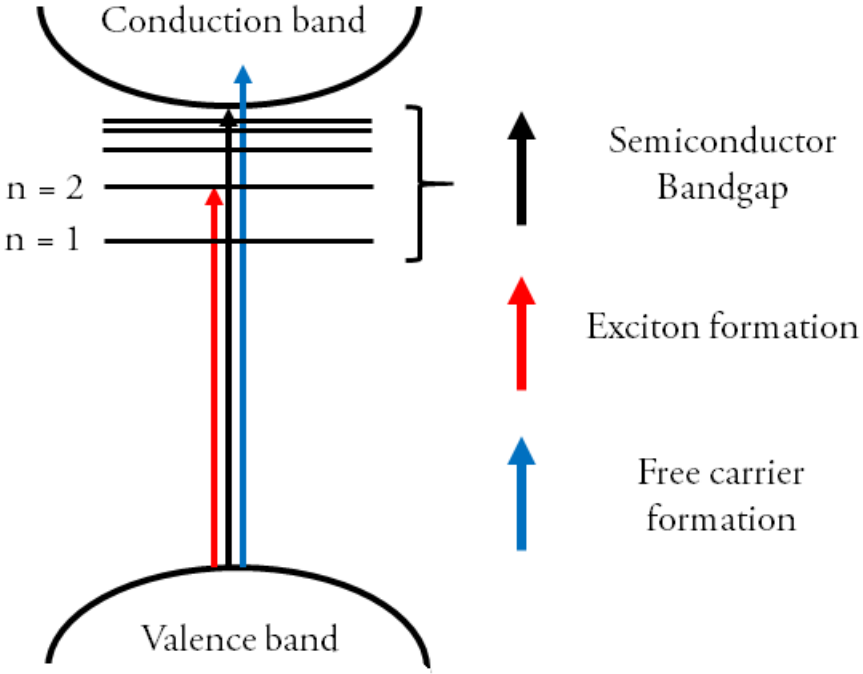

Figure 5.9. Simplified semiconductor band structure representing the excitonic and free carrier bands. The electronic transition happens between the valence and conduction bands. The bandgap is temperature-dependent.

The abundance of data on free carrier and exciton dynamics with conventional laser light allows us to compare our measurements at OAM = 0 to previous results.

The bandgap is dependent on the crystalline face and on temperature as shown in Eq. 17:

$$E_g = 1.519 - \frac{5.405 * 10^{-4} * T^2}{T + 204}\ eV \tag{17}$$

Additionally, lattice phonon modes are dominating the signal at high temperatures. Phonons act as vibrations of the lattice, adding vibrational and vibronic signals to the spectral features. Since we look for changes in the electronic signals of the sample as a function of orbital angular momentum, it is especially important to reduce the contribution of phonon modes. Cooling the sample to cryogenic temperature helps alleviate the issue. We have the capability of cooling the sample down to 4K using liquid helium. While the technical challenges associated with introducing cryostat in the setup are significant, it is important to implement the cooling for successful measurements. Coincidentally, the bandgap of bulk GaAs at 4K overlaps very well with the excitation spectrum, allowing us to simplify the experimental setup by avoiding using white light generation methods.

Additionally, doping concentration is capable of shifting absorption (36). The lineshape corresponds to the absorption under different doping conditions, and the rising feature that appears with the increased dopant concentration is indicative of an increased and shifted absorption peak. Doping alters the mobility of the charges in the lattice affecting the extent of motion of the charges. The effects of doping on the light-matter interaction can be measured as a function of doping concentration.

5.8. Macroscopic polarization and magnetization in spectroscopy: twisted light view

In order to describe the light-matter interaction, we need to understand the distribution of charges within the sample, and the interactions between these charges and incident fields. We assume the interactions to be semiclassical, where the sample is described in quantum mechanical terms, and the field is classical. Once the electric field of light is incident on the sample, the charges within the lattice experience a force that pushes them out of their equilibrium distribution. Once the field is gone, the charges start oscillating, creating time-dependent current density. The amplitude of the oscillations decreases with time after the initial excitation, and Here, we consider the minimal-coupling Hamiltonian, where the light-matter interaction is represented with the term p*A, where p is the canonical momentum operator, and A is the vector potential of the field (37). This Hamiltonian is simple and conventional when we consider the interactions in the dipole moment approximation. This, we can describe the Hamiltonian as Eq. 18:

$$H_{int} = p \cdot A = -i\hbar\nabla \cdot A \tag{18}$$

The vector potential of the field is derived from its electric field, and looks like the following for conventional light and twisted light (Eqs. 18, 19):

$$A(x, y, t) = \epsilon_{\pm} A_0 HG_{mn}(q_x, q_y) e^{i(qz-\omega t)} + c.c. \tag{19}$$

$$\text{and } A(r, t) = \epsilon_{\pm} A_0 LG_l(q_{r,} r) e^{i(qz-\omega t)} e^{il\phi} + c.c. \tag{20}$$

The current density associated with the light-matter interaction is generally described by the following equation 21 (4):

$$J = \frac{\partial P}{\partial t} + \nabla \times M \tag{21}$$

Here P is the macroscopic polarization, and M is the magnetization. In non-magnetic materials magnetization is typically neglected. Each of the terms can be written in the forms of multipolar expansion (Eq. 22):

$$P = P_{dipole} + P_{quadrupole} + \cdots \text{ and } M = M_{dipole} + M_{quadrupole} + \cdots \quad (22)$$

With this in mind, we can rewrite the interaction Hamiltonian through Power-Zienau-Wooley transformation (38) as a function of polarization from Eq. 23:

$$H_{int} = -\int P(r) \cdot D^{\perp}(r) dr \quad (23)$$

where D(r) is the transverse electric field displacement vector. This equation now accounts for all the terms in the polarization's multipolar expansion and allow us to deviate from the dipole moment approximation.

Electronic transition probability is governed by Fermi's Golden Rule (Eq. 24) (3):

$$\Gamma(i \to f) = \frac{2\pi}{\hbar} < f|H_{int}|i >^2 \Theta = \frac{2\pi}{\hbar} < f\left|C * e^{il\phi}\right|i >^2 \Theta \quad (24)$$

Θ is the density of states, i and f are the initial and the final states of the system, C is the constant associated with extracting the angular momentum terms out of the interaction Hamiltonian, $e^{il\phi}$ is the phase term for twisted light interaction.

Physically this means that the angular momentum and the energy of the photons in the excitation pulse are transferred to the sample to initiate the motion of the charges. When light without any orbital angular momentum interacts with the sample, the charges start oscillating in the dipolar fashion. This is governed by the selection rules for the transitions, as seen in Table 5.1 for transitions with combinations of various angular momenta (39, 40):

Transition	Selection rules (J – total angular momentum, L – orbital angular momentum, S – spin angular momentum)
Electric dipole	$\Delta J = 0, \pm 1$; $\Delta L = 0, \pm 1$; $\Delta S = 0$; states have to be of opposite parity
Electric quadrupole	$\Delta J = 0, \pm 1, \pm 2$; $\Delta L = 0, \pm 1, \pm 2$; $\Delta S = 0$; states have to be of same parity
Magnetic dipole	$\Delta J = 0, \pm 1$; $\Delta L = 0$; $\Delta S = 0$; states have to be of same parity

Table 5.1. Selection rules for electronic and magnetic transitions upon interaction with light

When the excitation pulse carries orbital angular momentum, due to its helical electric field vector potential, a geometrically non-uniform electric current density is generated and the charges begin to oscillate in a circular fashion. In other words, twisted light has spatial variations in the electric field, so the light-matter interactions also inherit spatial dependence. These oscillations are now governed by the higher order terms in polarization or magnetization, so the dipole moment approximation is not valid anymore. We expect the signal for the states that were previously negligible to increase as the multipolar terms in the interaction Hamiltonian become more significant.

Two competing effects happen upon interaction of twisted light with bulk semiconductors. Instead of vertical excitations typical to those of planar light, interband cone-shaped transitions are generated in the k-space due to the broadband nature of the pulse. Thus, we are accessing a number of states that support certain energy and OAM. These are responsible for the circular current observed upon excitation (Fig. 5.10) (41 – 45). On the other hand, the intraband transitions are responsible for the transfer of OAM to the electronic population in the conduction band.

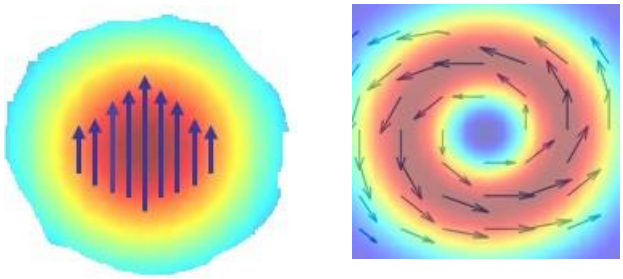

Figure 5.10. (Left) Dipolar oscillations of charges upon excitation. The largest magnitude of oscillations occurs in the center of the beam with OAM = 0 where the intensity is the strongest. (Right) Multipolar circular oscillations of the charges upon excitation with OAM = 1. The maximum oscillation intensity is along the maximum intensity of the beam.

In conclusion, the OAM of light transfers to the charges in the semiconductor lattice causing them to oscillate in a circular fashion. The transfer of orbital angular momentum allows to access the electronic transitions that were previously not accessible using conventional light due to selection rules. Because conservation of angular momentum AND energy is physically guaranteed, the newly-accessed electronic states in the conduction band will have a certain angular momentum and energy associated with them. Thus, spectroscopically we expect to see a shift in the signal as a function of OAM. The challenges of energy difference calculations will be discussed further.

5.9. Preliminary measurements of transient spectra of bulk GaAs as a function of OAM

Transient spectra of bulk GaAs were collected for OAM values of 0 through 5, and 10 (Fig 5.11). We resolve the transient signals by wavelength, represented on the x-axis, and the time delay between the pump and the probe beams, shown on the y-axis. The intensity of the signal at each time-wavelength point is represented with color. We can take a slice of data across the wavelength domain and obtain the signal decay profile at a certain wavelength. Alternatively, we can select a time point and take a slice of the transient spectrum at that time. We observe two main features in the collected transient spectra – a positive one centered at 815nm, and a negative one at 835nm.

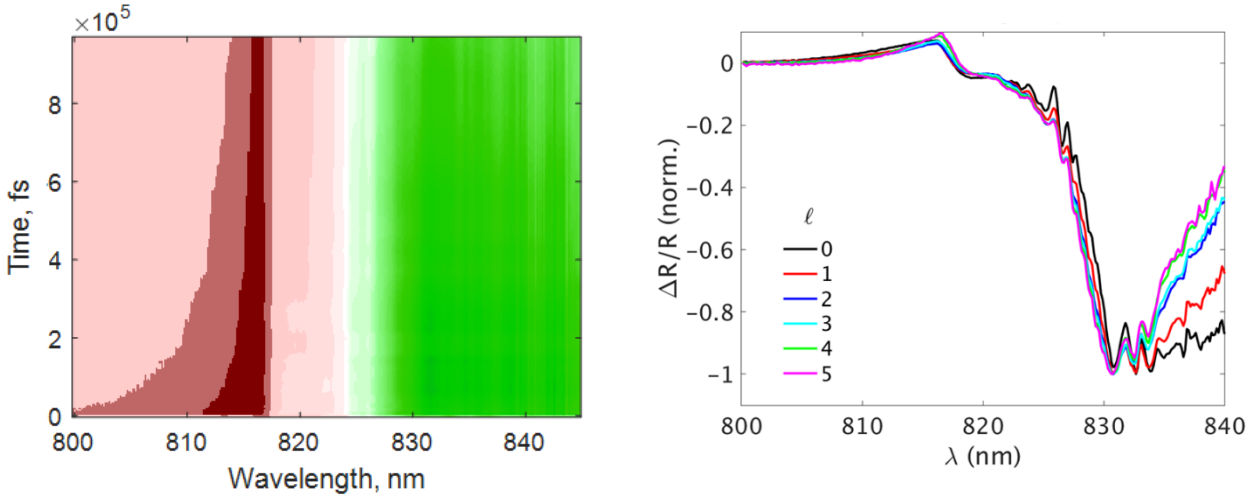

Figure 5.11. (Left) Waterfall plot of the transient absorption spectra we obtain experimentally for OAM = 0 showing the dependence of intensity (shown in color, red – positive, green – negative) on both time (y-axis) and wavelength (x-axis). (Right) The spectrum collected at 200ps as a function of OAM. Positive feature at ~815nm and negative feature at ~832nm are attributed to excitonic and free carrier features respectively.

The positive feature is in the vicinity of the bandgap of bulk GaAs at 4K and is assigned to the ground state bleach signal. This feature corresponds to the Wannier-Mott excitonic signal from the semiconductor (46). The negative feature is assigned to the excited state absorption due to its sign. We assign this feature to free carrier motion that is caused by exciting with energy far higher than the bangda. To test this assignment, we have filtered the excitation pulse's wavelength to 810-840nm (compared to 790-840nm spectrum originally), and observed significant drop in the amount of negative signal (Fig. 5.12).

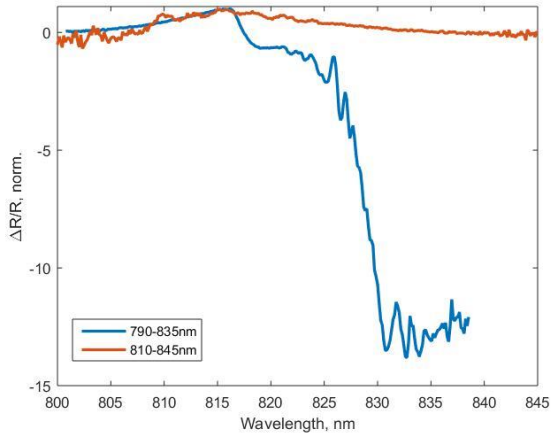

Figure 5.12. Elimination of free carrier signal upon filtering the blue edge of the excitation pulse from 790nm to 810nm. A significant change in the amount of negative signal is observed confirming the assignment of the positive feature to excitonic transitions, and negative feature of free carrier transitions.

The excitonic feature shows a red spectral shift as a function of orbital angular momentum (Fig. 5.13). Here we plot the transient spectra at OAM from 0 to 5 at the time delay of 200ps. It is worth noting that similar shifts are observed at other time delays too. As we increase the amount of OAM imparted in the beam, we observe the trend breaking for OAM = 10, and the excitonic feature signal returns to OAM = 0 position. These results can be explained by existence of spatial coherence, which was previously observed in GaN excited with twisted light (47). This effect cannot be explained with heating effect from the high beam fluence at the focal spot, because we observe identical shifts at early and late times across the different delay measurements. The strongest heating effect should be observed directly after excitation resulting in different spectral signal compared to later times. Because we can assume this kind of interaction is similar to particle-on-a-hollow-cylinder model, that accounts for the beam diameter change, leading to different exciton sizes at OAM = 0 and OAM = 10. This also proves that this effect is due to properties of twisted light, and not local excitation artifacts.

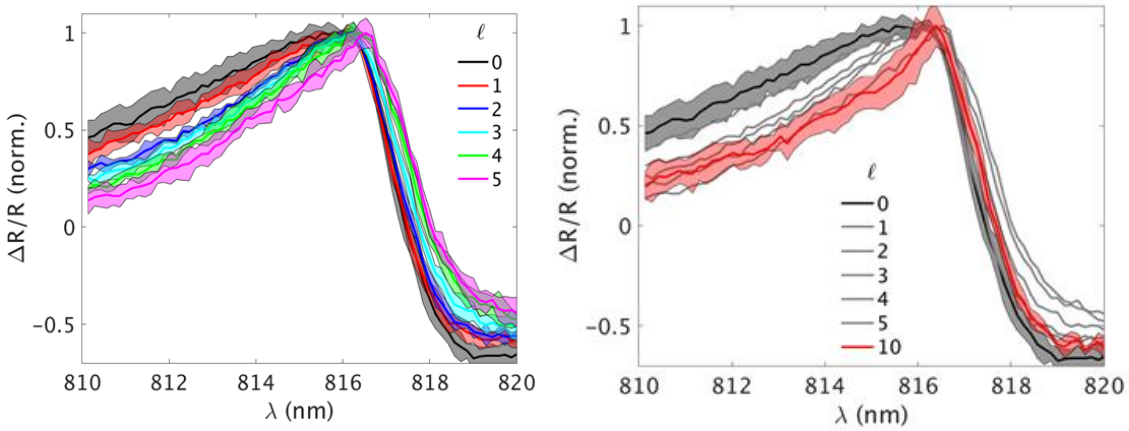

Figure 5.13. A close look on the excitonic feature as a function of OAM. (Left) A red spectral shift is observed as OAM is increased from 0 to 5. (Right) At high OAM values the excitonic feature resembles OAM = 0 trace, indicating that there is a limit to how much OAM can be transferred into the sample.

The free carrier interactions as a function of OAM are represented in Figure 5.14. The negative feature, that is assigned as the excited state absorption, shows the shift in the direction of higher energy as the OAM increases. This shows that the electronic states in the conduction band with higher energy support the higher amount of orbital angular momentum, according to conservation of momentum and energy. A similar effect, where the OAM = 10 spectrum overlaps with the OAM = 0 spectrum, is observed. At small values of OAM, it is possible for the center of the twisted beam to create a coherent excitation in the center of the beam. This is due to a small node in the center of the beam. When the low intensity region becomes too wide to generate a spatially coherent excitation in the center of the beam, each charge essentially "feels" a planar-like momentum, experiencing only a small arc of the beam's twist. It is possible to conclude that the small values of OAM generate center-of-mass motion of the charges, while the large values of OAM exceed this radius possible for this kind of motion.

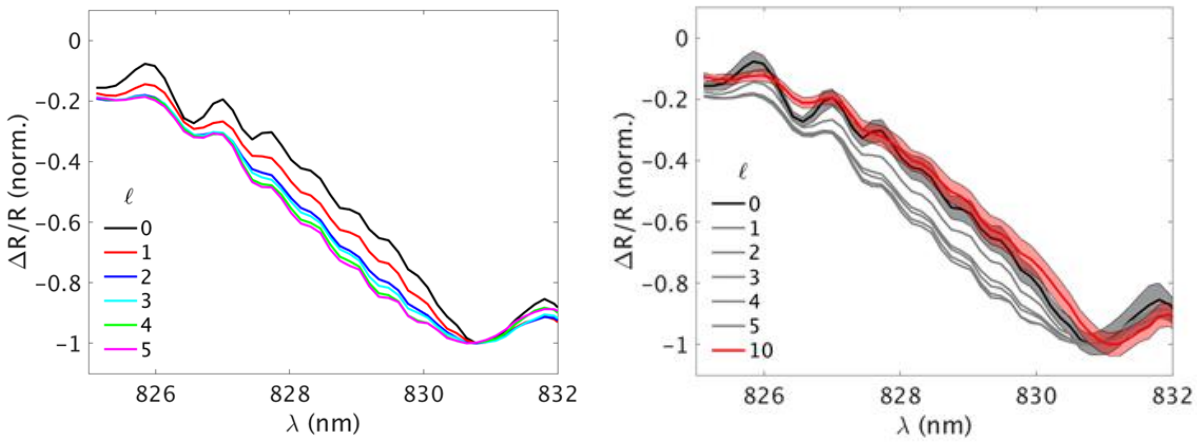

Figure 5.14. A close look on the free carrier feature as a function of OAM. (Left) A blue spectral shift is observed as OAM is increased from 0 to 5. (Right) At high OAM values the free carrier feature resembles OAM = 0 trace, indicating that there is a limit to how much OAM can be transferred into the sample (similar to figure 5.13).

5.10. Direct measurement of induced magnetization with OAM of light

We have collected the transient spectra for negative values of OAM. The range we've selected was from OAM = -5 to OAM = -1 due to previously observed spectral changes at their counterparts. We have observed the differences in the excitonic feature when comparing +OAM and -OAM spectra. This led to the discovery that the differential signal is the sign of induced magnetization upon excitation. Let's consider the current density (Eq. 25):

$$J = \frac{\partial P}{\partial t} + \nabla \times M \tag{25}$$

Back of the envelope derivations have shown that the polarization term in the current density is independent on the sign of the OAM, whereas the magnetization term is. It makes sense, as the charges flowing circularly generate magnetic field that is dependent on the direction of that current.

It was, however, unexpected that this would result in resolvable spectral and intensity changes (Fig. 5.15).

In order to extract the magnetization term, we perform subtraction of the signals from +OAM and -OAM (Eq. 26):

$$J_{+OAM} - J_{-OAM} = \frac{\partial P_{+OAM}}{\partial t} + \nabla \times M_{+OAM} - (\frac{\partial P_{-OAM}}{\partial t} + \nabla \times M_{-OAM})$$

$$J_{+OAM} - J_{-OAM} = \nabla \times M_{+OAM} - (-\nabla \times M_{+OAM})$$

$$J_{+OAM} - J_{-OAM} = 2\nabla \times M_{+OAM} \quad (26)$$

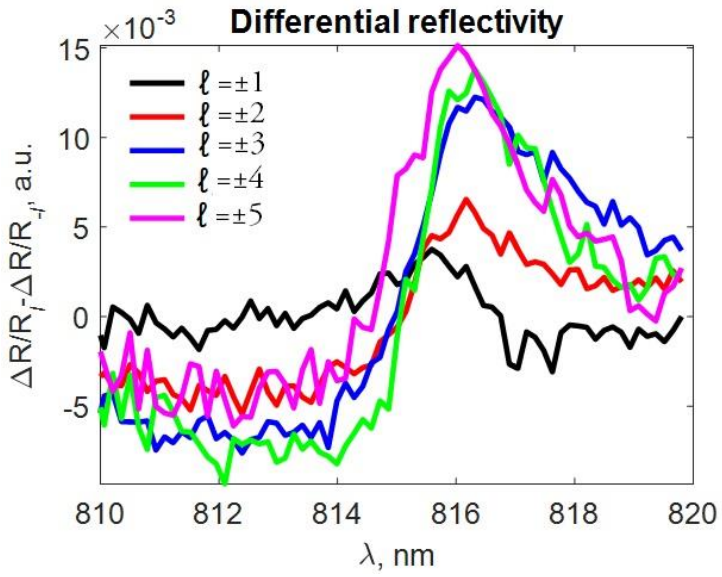

Figure 5.15. Direct measurement of magnetization obtained from subtraction of spectra with +OAM and -OAM. The magnitude of magnetization increases as a function of |OAM|.

Thus, we can claim that we can directly measure macroscopic magnetization that is induced in bulk GaAs upon interaction with OAM. Unfortunately, this magnetization is extremely hard to measure externally to prove the concept, as the magnitude of magnetization is extremely small and

5.11. Challenges in modeling interactions of orbital angular momentum of light with bulk semiconductors

Modeling interaction of orbital angular momentum of light with bulk semiconductors is extremely challenging. One challenge comes from the vastness of the 3D lattice of the sample. With the large excitation volume comes a huge amount of excitations created – both excitons and free carriers depending on the excitation spectrum. Approximations are made to simplify the modeling of interactions of semiconductors with light. Many-body interactions are simplified using so-called GW method – where one-body Green's function is combined with the screened Coulombic interaction (48). Addition of spin-orbit coupling is possible in this model. Tight-binding parametrization and classical treatment of electrostatic screening (49, 50) allow for making the calculations more efficient. Optical properties calculated with these methods are using the light in the form of a conventional Gaussian beam, where dipole-moment approximation is applied, and the charges oscillate in a uniform fashion. Additionally, because most excitation occurs in the center of the beam, it is possible to just model the small area that will describe the motion of charges, and then account for the decay in the beam's intensity. This decay can be propagated to the whole excitation area to account for many-body interactions, but this is still a computationally expensive problem to solve.

Moreover, a set of challenges arise from the twist in the electromagnetic field when exciting with light carrying orbital angular momentum. This is because the current generated upon excitation now follows circular trajectory and is non-uniform. As mentioned in previous sections, dipole moment approximation cannot be used anymore. We cannot treat the excitations in the center of the beam anymore because there is no light intensity in the center of the beam. The interactions get increasingly more complex as the amount of OAM increases. There are possible ways of simplifying the calculations involving twisted light both for excitonic and free carrier interactions.

When the bulk semiconductor is excited below the bandgap, Wannier-Mott excitons are formed. These excitons can be modeled as a modified positronium atom (Fig. 5.16). A positronium atom resembles an exciton because it is a Coulombically bound pair of an electron and a positron. Due to its similarities to hydrogen atom one could use the rigid rotor model to calculate the energy states associated with the transfer of energy and momentum from light to the atom. Quantum mechanical description of rigid rotors accounts for the orbital angular momentum of the system and explains the selection rules for electronic transitions. For systems that are more complex than a simple pair of electron and positron – like bulk semiconductors – one should use the effective masses of the electron and the hole for that particular system. However, this method does not account for multiexcitonic interactions in upon excitation which will skew the energy levels due to the coupling.

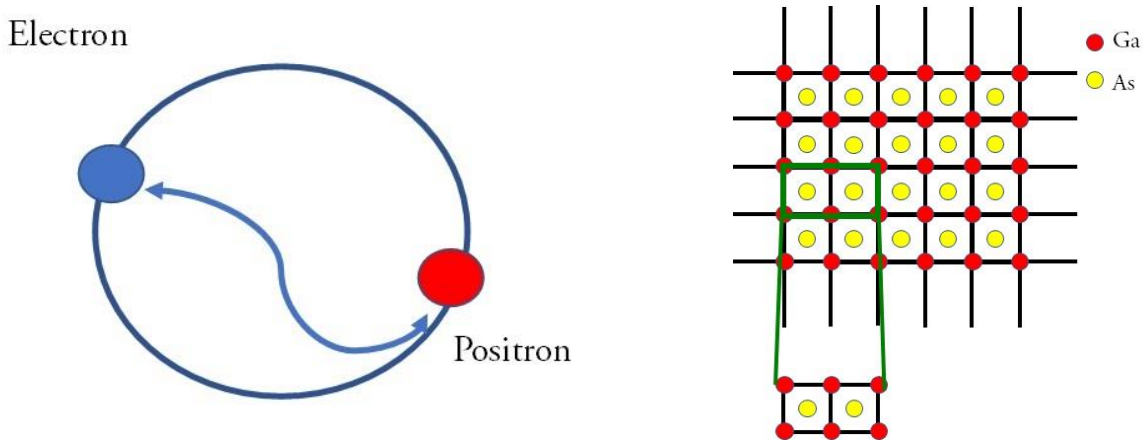

Figure 5.16. (Left) Proposed positronium atom scheme for calculation of excitonic transitions with OAM using rigid rotor model. (Right) Selecting a small section of the bulk semiconductor lattice to perform free carrier interaction calculations. This makes the calculations less computationally expensive, but omit many-body interactions in the system.

On the other hand, free carriers are generally calculated using density functional theory (DFT). The perturbation that is included in DFT does not account for non-uniformity of twisted light. Free carriers are formed along the area of the beam intensity and their oscillations are weaker towards the center of the excitation area. This radically complicates the calculations where the dipole-moment approximation cannot be applied anymore, and a large amount of charges is moving in a circular fashion within the lattice. One can assume that twisted light is applied to one or two unit cells within the lattice to simplify the amount of particles involved in the calculation (Fig. 5.16). However, like in the case with excitons described above, this does not account for many-body interactions. If too many unit cells are involved in the calculations, the time taken to model increases exponentially. A compromise needs to be found to make the reasonable approximations of the size of the lattice involved while still maintaining practical calculation time.

References

(1) D.A. McQuarrie, J.D. Simon. Physical chemistry: a molecular approach. University Science Books, 1997

(2) C. Cohen-Tannoudji, J. Dupont-Roc, G. Grynberg. Photons and atoms: introduction to quantum electrodynamics. Wiley-VCH, 1997

(3) C. Cohen-Tannoudji, B. Diu, F. Laloe. Quantum mechanics, Vols. 1 and 2, Wiley-VCH, 2019

(4) S. Mukamel. Principles of nonlinear optical spectroscopy. Oxford University Press, 1995

(5) R. Menzel. Photonics: linear and nonlinear interactions of light and matter. Springer-Verlag, Berlin, 2001

(6) J.H. Poynting. The wave-motion of a revolving shaft, and suggestions as to the angular momentum in a beam of circularly polarized light. Proc. R. Soc. Lond. A, 82:560-567, 1909

(7) L. Mandel, E. Wolf. Optical coherence and quantum optics. Cambridge University Press, 1995

(8) E. Hecht. Optics. Addison-Wesley, Fourth edition, 2001

(9) M. Padgett, L. Allen. Light with a twist in its tail. Contemporary Physics, 41(5):275-285, 2000

(10) N. Bozinovic, Y. Yue, et al. Terabit-scale orbital angular momentum mode division multiplexing in fibers. Science, 340:1545-1548, 2013

(11) J. Wang, J.Y. Yang, et al. Terabit free-space data transmission employing orbital angular momentum multiplexing. Nature Photonic, 6(7):488, 2012

(12) A.E. Willner, H. Huang, et al. Optical communications using orbital angular momentum beams. Advances in Optics and Photonics, 7(1):66-106, 2015

(13) Y. Chen, W.G. Shen, et al. Underwater transmission of high-dimensional twisted photons over 55 meters. PhotoniX, 1(5), 2020

(14) A. Ashkin. Acceleration and trapping of particles by radiation pressure. PRL, 24(4):156-159, 1970

(15) A. Ashkin, J.M. Dziedzic, et al. Observation of a single-beam gradient force optical trap for dielectric particles. Optics Letters, 11(5):288-290, 1986

(16) M. Friese, J. Enger, et al. Optical angular momentum transfer to trapped absorbing particles. Physical Review A, 54(2):1593, 1996

(17) G.A. Swartzlander, E.L. Ford. Astronomical demonstration of an optical vortex coronograph. Optics Express, 16(14):10200-10207, 2008

(18) G.A. Swartzlander. The optical vortex coronograph. Journal of Optics A, 11(9):094022, 2009

(19) S.W. Hell, J. Wichmann. Breaking the diffraction resolution limit by stimulated emission: stimulated emission depletion fluorescence microscopy. Optics Letters, 19(11):780-782, 1994

(20) V. Westphal, S.O. Rizolli, et al. Video-rate far-field optical nanoscopy dissects synaptic vesicle movement. Science, 320(5873):246-249, 2008

(21) G. Goubau, F. Schwering. On the guided propagation of electromagnetic wave beams. IRE Transactions on Antennas and Propagation, 9(3):248-256, 1961

(22) F. Pampaloni, J. Enderlin. Gaussian, Hermite-Gaussian and Laguerre-Gaussian beams: a primer. arXiv, 2004

(23) S.M. Barnett, L. Allen. Orbital Angular momentum and nonparaxial light beams. Optics Communications, 110(6):670-678, 1994

(24) F.A. Bovino. Quantum-like representation of a spiral phase plate. arXiv, 2011

(25) G. Turbull, D. Robertson, et al. The generation of free-space Laguerre-Gaussian modes at millimeter-wave frequencies by use of a spiral phase plate. Optics Communications, 127(6):183-188, 1996

(26) M. Beijersbergen, R. Coerwinkel, et al. Helical-wavefront laser beams produced with a spiral phase plate. Optics Communications, 112(6):231-237, 1994

(27) L. Marrucci, C. Manzo, et al. Optical spin-to-orbital angular momentum conversion in inhomogeneous anisotropic media. PRL, 96(16):163905, 2006

(28) L. Marrucci. The q-plate and its future. Journal of Nanophotonics, 7:078598, 2013

(29) J.P. Torres, L. Torner. Twisted photons: Applications of light with orbital angular momentum. John Wiley & Sons, 2011

(30) C. Guo. Optimal annular computer-generated holograms for the generations of optical vortices. J. Opt. Soc. Am. A, 22(2):385-390, 2005

(31) W. Cheng. Optical vortex beams. University of Dayton, 2013

(32) M.J. Padgett, L. Allen. The Poynting vector in Laguerre-Gaussian laser modes. Optics Communications, 121:36-40, 1995

(33) Y.P. Varshni. Temperature dependence of the energy gap in semiconductors. Physica, 34(1):149-154, 1967

(34) H. Tahara, Y. Kanemetsu. Observation of localized states in bulk GaAs using ultrafast photocurrent beat spectroscopy. Applied Physics Express, 9(3):032403, 2016

(35) W. Li, W. Peng, et al. Femtosecond reflection of bulk GaAs and GaAs/AlGaAs multiple quantum wells. Ultrafast Processes in Spectroscopy, Springer, Boston, Massachusetts, 1996

(36) S. Olthof, W. Tress, et al. Photoelectron spectroscopy study of systematically varied doping concentrations in an organic semiconductor layer using a molecular p-dopant. Journal of Applied Physics, 106:103711, 2009

(37) R. Loudon. The quantum theory of light. Claredon Press, Oxford, 1973

(38) M. Babiker, R. Loudon. Derivation of the Power-Zienau-Wooley Hamiltonian in quantum electrodynamics by gauge transformation. Proc. R. Soc. Lond. A, 385:439-460, 1983

(39) J. Zurita-Sanchez, L. Novotny. Multipolar interband absorption in a semiconductor quantum dot. I. Electric quadrupole enhancement. J. Opt. Soc. Am. B, 19(6):1355-1362, 2002

(40) J. Zurita-Sanchez, L. Novotny. Multipolar interband absorption in a semiconductor quantum dot. II. Magnetic dipole enhancement. J. Opt. Soc. Am. B, 19(11):2722-2726, 2002

(41) G. Quinteiro, P. Tamborenea. Twisted-light-induced optical transitions in semiconductors: free-carrier quantum kinetics. Phys. Rev. B, 82:125207, 2010

(42) G. Quinteiro, P. Tamborenea. Theory of the optical absorption of light carrying orbital angular momentum by semiconductors. EPL. 85:47001, 2009

(43) G. Quinteiro, D. Reiter, T. Kuhn. Formulation of the twisted light-matter interactions at the phase singularity: the twisted light gauge. arXiv, 2014

(44) G. Quinteiro. Below-bandgap excitation of bulk semiconductors by twisted light. EPL, 91:27002, 2010

(45) M. Babiker, C.R. Bennett, et al. Orbital angular momentum exchange in the interaction of twisted light with molecules. PRL, 89(14):143601, 2002

(46) G.C. la Rocca. Wannier-Mott excitons in semiconductors. Thin Films and Nanostructures, 31:97-128, 2003

(47) Y. Ueno, Y. Toda, et al. Coherent transfer of orbital angular momentum to excitons by optical four-wave mixing. Optics Express, 17(22):20567-20574, 2009

(48) E. Mosconi, P. Umari, F. De Angelis. Electronic and optical properties of MAPbX3 perovskites (X = I, Br, Cl): a unified DFT and GW theoretical analysis. Physical Chemistry Chemical Physics, 39, 2016

(49) Y. Cho, T.C. Berkelbach. Optical properties of layered hybrid organic-inorganic halide perovskites: a tight-binding GW-BSE study. J. Phys. Chem. Lett., 10(20):6189-6196, 2019

(50) R. Tempelaar, T.C. Berklebach. Many-body simulation of two-dimensional electronic spectroscopy of excitons and trions in monolayer transition metal dichalcogenides. Nature Communications, 10:3419, 2019

(51) Wikimedia Commons. File: Spiral-phase-plate.svg - Wikimedia Commons, the free media repository.https://commons.wikimedia.org/wikipedia/commons/1/1f/Spiral-phase-plate.png, 2011

(52) Wikimedia Commons. File: Mode-converter.png - Wikimedia Commons, the free media repository. https://commons.wikimedia.org/wiki/File:Mode-converter.png, 201

CHAPTER 6

FUTURE DIRECTIONS

6.1 Reactions to stress in cyanobacteria

In this thesis I have discussed the energy quenching mechanisms in various organisms, including cyanobacteria, green sulfur bacteria and green algae. Specifically, in Chapter 3 I described the proposed energy quenching mechanism for cyanobacteria that lack the orange carotenoid protein. We found that energy quenching primarily occurs in the phycobilisome rods via exciton-exciton annihilation. This finding leaves a lot of questions unanswered as an opportunity for future work on these organisms, as well as other light-harvesting organisms that employ photoprotection against stress.

Cyanobacteria contain phycobilisomes that harvest sunlight and pass it down the funnel to the reaction center for further photosynthetic steps. Additionally, this sunlight can be passed in the form of the chromophore excitation to form reactive oxygen species that cause lethal damage to the organism. Alternatively, the excitations can be quenched through non-protochemical quenching mechanisms and dissipate into the bath as heat. In Synechocystis sp. PCC 6803, the orange carotenoid protein (OCP) is mainly responsible for eliminating the excess energy by isomerizing between its orange and red forms with the help of the fluorescence recovery protein (1). Also, it is known that cyanobacteria are prone to mutagenesis, allowing to alter the structure of the light-harvesting antenna to test various hypotheses about the processes happening in the organism. One of the proposals for future work is to use mutagenesis to eliminate the OCP quenching site from the PCC 6803 strain. The mutated cells could be further subjected to fluence-

dependent non-linear spectroscopic experiments to differentiate the energy transfer and excess energy quenching mechanisms in the absence of the OCP. The results from mutated PCC 6803 can be compared to PCC 7942 (bacteria that initially do not contain OCP, described in Chapter 3 in detail) to identify the differences in the quenching mechanisms. In the Engel group, we are capable of performing ultrafast transient absorption and two-dimensional electronic spectroscopy experiments in both isolated phycobilisomes and in vivo cells. These experiments, however, present a set of challenges such as high scatter levels, PBS/cell death upon prolonged exposure to light, low signal levels at low excitation powers that require strong averaging. Some of these challenges can be met by flowing the sample through the sample cell using a peristaltic pump. In 2D experiments, GRAPES – a unique method developed in the Engel group (2) – can be used to minimize the duration of the measurements. Post-processing techniques of boosting signal-to-noise ratio and minimizing scatter can be also used, as described in Chapter 1 of this work.

As discussed in previous chapters, phycobilisomes consist of higher-energy rods and the lower-energy core. Through mutagenesis, it has been shown that bacteria with shorter rods or smaller core can be grown as well (3). Presumably, these mutations in PCC 7942 should be the sources of extra stress during light-harvesting, as there is a smaller amount of chromophores available to facilitate the energy quenching and transfer. I hypothesize that shorter rods would decrease the time of energy transfer to the core. Additionally, with lower chromophore availability for the exciton-exciton annihilation, the damage to the organism would be more significant in comparison to the unmutated organism at the same excitation energy. Non-linear spectroscopic methods would be ideal experiments to test this hypothesis.

Interestingly, red algae contain phycobilisomes that also do not have OCP near their structure to use for photoprotection (4). These algae rely on phycobilisomes to perform the excess energy quenching. To date, it is unknown if there are other photoprotective mechanisms present in red algae to substitute for OCP. Thus, upon growth of the algae in the lab, and studying them with non-linear spectroscopic methods can reveal the extent of phycobilisome contribution to the stress environments.

All of the ideas described earlier relied on the stress that is caused by excess sunlight supplied to the organism. However, there are additional types of stress, such as nutrient deficiency, that limit the photosynthetic processes and damage the bacteria. Specifically in cyanobacteria, it is known that low iron supply limits the growth of the organism (5, 6). Expression of photosystem I (PS I) in thylakoid membrane – the antenna encountered after the reaction center and photosystem II (PS II) – heavily relies on the iron concentration. When iron is in low supply, iron stress induced protein A (IsiA) is expressed to encompass the PSI and increase its light-harvesting efficiency. The energy transfer between PSII and PSI-IsiA complexes can be also studied using non-linear spectroscopies to unravel the effect of the IsiA on the light-harvesting properties of cyanobacteria.

6.2 Interaction of orbital angular momentum of light with matter

In Chapter 5 I have described the preliminary experiments we have conducted to understand the transfer of orbital angular momentum from light to bulk GaAs at cryogenic temperatures. Upon successful reproducibility of the transient spectra, we will continue exploring the unique interaction of OAM of light with various samples.

To measure the interaction of OAM of light with the sample, the system needs to be able to form large delocalized excited states. This involves generating Wannier-Mott excitons that tend to have large exciton radii. Alternatively, the mobility of the charges should be high enough for the electrons to travel in a circular fashion along the size of the focused twisted beam at the sample. Semiconducting systems seem to be the perfect samples for these measurements due to formation of large excitons and electrons traveling relatively "freely" in the pool of charges. In our initial experiments we have explored the interaction of OAM with bulk gallium arsenide. Here, the charges are mobile not only across the surface of the semiconductor, but also through the depth of light penetration (~15μm for 800 nm). We can extend this study to two-dimensional semiconducting systems – quantum wells, where the charges will only be able to travel along the surface layers of the material. This also expands the breadth of samples we can study to perovskite systems, two-dimensional materials like MoS_2 and aggregates with long-range charge interactions. While reducing semiconductor dimensionality (7) is certainly an interesting direction of work for comparison of OAM interactions, we do not anticipate observing differences in spectral features as a function of OAM in nanorods and quantum dots. This is due to the fact that the excitons are not as delocalized in these systems, as in 2D and 3D materials, so charges cannot interact with the curvature of the twisted beam's electromagnetic field. A number of challenges arises in the path towards measuring the interaction of OAM with systems of lower than 3 dimensionalities. Since the exciton delocalization length drops with dimensionality, the excitation beam needs to be focused to the size of the delocalization length, which beats the diffraction limit in the nanorod or quantum dot case. Additionally, as in the case with bulk GaAs, cooling to cryogenic temperatures is needed to avoid phonon modes overshadowing the signal emitted from the excited states with

OAM transferred. The measurements can be further expanded to organic semiconducting systems. Interestingly, it has been shown that interaction of twisted light with the chiral samples does not produce any differential response, unlike interaction of circularly-polarized light with chiral molecules (8). Understanding the samples' responses to orbital angular momentum of light can identify the material's properties as detectors for classical and quantum communications systems.

Quantifying spin-orbit coupling in complex chemical systems has been a challenging issue in theoretical and experimental chemistry. One way to solve this problem is coupling spin and orbital angular momenta in one excitation pulse. This results in the transfer of total angular momentum of light to the system (Eq. 1):

$$TAM = OAM + SAM \quad (1)$$

One can look at the differences in the spectral features generated by transferring various combinations of SAM and OAM to the sample (making up identical TAM). It is important to remember that SAM can only take values of –1, 0 and +1, while OAM can potentially have infinite amount of values (however, technical limitations of SLMs do not allow to introduce extremely large amounts of OAM to light). For instance, for TAM = +5, one can generate three combinations of SAM and OAM:

SAM = +1, OAM = +4

SAM = 0; OAM = +5

SAM = –1; OAM = 6

A pump-probe experiment is then performed with the light carrying both SAM and OAM. While this would only require an addition of a quarter waveplate and a polarizer to the setup, the main challenge associated with this measurement is the precise alignment of circularly-polarized light prior to applying SLM phase mask to the beam. In Chapter 5 I show that the difference in the excitonic feature is very small (~1nm between OAM = 0 and OAM = 5). The differences in the signals that include SAM may be less detectable which would require improvements in the detection scheme with improvements in spectral resolution.

Finally, entanglement of the angular momenta states has been a topic of interest since OAM was first generated in 1990s (9, 10). One way to quantify the entanglement of the states is to apply a phase mask to the spatial light modulator that contains multiple values of OAM to transfer multiple OAM into the beam. Here we consider an experiment with a single beam, like in a linear absorption method. The excitation/pump beam interacts with the sample emitting a signal that should correspond to the transfer of the mixed state of OAM. That beam with the signal is then sent to additional two spatial light modulators that contain the phase masks that geometrically separate the signals corresponding to different OAM values and collimate each of the separated beams respectively (11). These separated signals are captured in a spectrometer and a two-dimensional camera, and recorded. They are further compared to the signals from individually measured corresponding OAM values. For example, OAM values of 3 and 5 are mixed in the pump beam. Upon interactions with SLMs 3 and 4, the signal is separated into OAM' = 3 and OAM' = 5 components, where OAM' is the signal from entangled angular momenta beam. We then consider the following:

OAM = 5 vs OAM’ = 5

OAM = 3 vs OAM’ = 3

If the difference is observed, we can claim that the excited state from OAM’ = 3 interaction in the combined beam is entangled to the excited state from OAM’ = 5. The challenge may arise from the hardly detectable difference in the spectra upon comparison. This would require improvement of the detection scheme with better spectral resolution.

References

(1) D. Harris, O. Tal, et al. Orange carotenoid protein burrows into the phycobilisome to provide photoprotection. PNAS, 113:E1655-E1662, 2016

(2) E. Harel, A.F. Fidler, G.S. Engel. Single-shit gradient-assisted photon echo electronic spectroscopy. JPCA, 115(16):3787-3796, 2011

(3) I.H.M. van Stokkum, M. Gwizdala, et al. A functional compartmental model of the Synechocystis PCC 6803 phycobilisome. Photosynthesis Research, 135:87-102, 2018

(4) R. Kana, E. Kotabova, et al. Phycobilisome mobility and its role in the regulation of light harvesting in red algae. Plant Physiology, 165:1618-1631, 2014

(5) E.J. Boekema, D.A. Semchonok. Organization of photosynthetic membrane proteins into supercomplexes. Light Harvesting in Photosynthesis, Ch 10. CRC Press, Boca Raton, FL, 2018

(6) J. Sun, J.H. Golbeck. The presence of the IsiA-PSI supercomplex leads to enhances PSI electron throughput in iron0starved cells of Synechococcus sp. PCC 7002. JPCB, 119(43):13549-13559, 2015

(7) T. Kuhn, D.E. Reiter, G.F. Quinteiro. Optical control of exciton and spin states in a quantum dot by excitation with twisted light. Journal of Physics: Conference Series, 647:012012, 2015

(8) F. Araoka, T. Verbiest, et al. Interactions of twisted light with chiral molecules: an experimental investigation. Physical Review A, 71:055401, 2005

(9) A. Muthukrishnan, C.R. Stroud Jr. Entanglement of internal and external angular momenta of a single atom. J. Opt. B: Quantum Semiclass. Opt., 4:S73-S77, 2002

(10) R. Fickler, R. Lapkiewicz, et al. Quantum entanglement of high angular momenta. Science, 338(6107):640-643, 2012

(11) G.C.G. Berkhout, M.P.J. Lavery, et al. Efficient sorting of orbital angular momentum states of light. PRL, 105:153601, 2010

CHAPTER 7

CONCLUSIONS

This thesis encompasses the idea of measuring ultrafast dynamics in photosynthetic and semiconducting systems with the goal of learning about the curious phenomena such as quantum coherences, energy transfer. The overarching theme of my work is using very short – ultrafast – pulses to reveal the dynamic electronic properties of my systems of interest. This knowledge can be then applied to outstanding issues such as efficiency of classical and quantum communications, development of artificial systems to harvest solar energy. Femtosecond nonlinear spectroscopy is an excellent technology to address the questions of nature's design principles and evolution.

In Chapter 1 I introduce the main goal of this thesis, and present the concept of light-matter interactions in semiclassical approximation. Later, I discuss the ultrafast methods that are used to probe these light-matter interactions. Specifically, I write about femtosecond transient absorption spectroscopy, and point-by-point two-dimensional electronic spectroscopy. I finish the chapter with the nuances in data processing and analysis from these two experimental methods.

In Chapter 2 I describe in detail the overall process of photosynthesis, with multiple stages taking places at various timescales. Then, I focus on the initial stage of photosynthetic process – harvesting of solar energy and its transfer to the reaction center for the release of an electron. This stage occurs on ~1ns timescale making ultrafast pump-probe and 2DES setups perfect fits for the desired measurements. Further I elaborate on the principles of energy transfer in photosynthetic complexes, providing the differences between FRET, Redfield and coherent transfers. I finish the section with presenting various known photoprotective mechanisms in different organisms to show

how the species have evolved to deal with stress – whether it is due to excess solar energy, or lack of nutrients, etc.

I begin Chapter 3 with the description of cyanobacteria and their light-harvesting antenna complex called phycobilisome. Then I focus on a specific bacterium – Synechococcus elongatus PCC 7942 – and its mechanisms of energy quenching in the absence of the orange carotenoid protein. We performed fluence-dependent transient absorption measurements on isolated phycobilisomes from PCC 7942 and found that exciton-exciton annihilation appears to be the dominant photoprotective mechanism in this antenna complex. We also experimentally confirmed the exciton hopping times that have previously been predicted theoretically for this system.

Chapter 4 discusses methodology to obtain precise Hamiltonian in Fenna-Matthews-Olson complex with the help of hierarchical equations of motion (HEOM). The novel data post-processing protocol is tested in combination with HEOM to confirm the energies of the eight excitons formed in the light-harvesting complex with the further use in systems with less known Hamiltonians.

In Chapter 5 I describe in detail in implications of applying orbital angular momentum to the pulse, and then its interaction with matter. I discuss the applications of twisted light in astrophysics and imaging. I further provide physical description of twisted light, including representation of the electric and magnetic fields of the beam. The ways of introducing orbital angular momentum to the beam are mentioned further. I continue with the description of the transient absorption setup to measure the interaction of twisted light and the sample, followed by the reasons for choosing bulk gallium arsenide as the system of interest.

Later I provide a detailed theoretical description of the interactions of twisted light with matter followed by the preliminary experimental data that we have observed. Here I look into spectral shifts in the two main spectral features in the sample at cryogenic temperatures as a function of OAM. I further investigate the implications of applying positive and negative values of OAM to the sample, and describe the calculation of induced magnetization, as well as show experimental results obtained for +OAM and -OAM difference.

I conclude this thesis with the possible extensions of my work. First, I discuss the ideas of performing non-linear spectroscopic experiments on organisms where OCP is mutated out or not present at all to compare to results obtained in our work. Additionally, I discuss in detail the future direction in work about twisted light, where, I believe, there is a lot of potential to generate impactful datasets and explain the phenomena of angular momentum transfer to chemical systems.